

Eighteen-Month Report on LDRD 20080085 DR: Construction and Use of Superluminal Emission Technology Demonstrators with Applications in Radar, Astrophysics, and Secure Communications.

LANL Team:

**John Singleton¹ (PI), David Bizzozero^{2*}, Dale Dalmas³, Larry Earley³,
Joe Fasel², Todd Graves⁴, Ian Higginson^{3*}, Bill Junor⁵, Frank L.
Krawczyk³, Quinn R Marksteiner³, John Middleditch⁶, John Quenzer^{3*},
Bill Romero³, Pinaki Sengupta¹, Andrea Schmidt², Petr Volegov⁷, Zhi-Fu
Wang³**

¹MPA-NHMFL, Los Alamos National Laboratory, MS E536, Los Alamos NM 87545

²AET-2, Los Alamos National Laboratory, MS E548, Los Alamos NM 87454

³ISR-6, Los Alamos National Laboratory, MS H851, Los Alamos, NM 87545

⁴CCS-6, Los Alamos National Laboratory, MS F600, Los Alamos NM 87545

⁵ISR-2, Los Alamos National Laboratory, MS D436, Los Alamos NM 87545

⁶CCS-3, Los Alamos National Laboratory, MS B265, Los Alamos NM 87545

⁷P-21, Los Alamos National Laboratory, MS D454, Los Alamos NM 87545

(*Summer students temporarily attached to the project.)

Collaborators:

Houshang Ardavan⁸, Arzhang Ardavan⁹, Mario Perez¹⁰

⁸Institute of Astronomy, University of Cambridge, Madingley Road,
Cambridge CB3 0HA, U.K.

⁹Clarendon Laboratory, Department of Physics, University of Oxford, Parks Road,
Oxford OX1 3PU, U.K.

¹⁰Astrophysics Division, 3Y28, NASA-Headquarters, 300 E. Street SW,
Washington DC 20546, U.S.A.

Contents

1	Introduction	5
1.1	History	5
1.2	Some general points about superluminal sources: multivalued retarded times and temporal focusing	6
1.3	The path onwards	7
1.3.1	The technology demonstrators.	7
1.3.2	Mathematical and numerical work.	8
1.3.3	Astrophysical work in the program.	9
1.3.4	Commercialization.	9
2	Building and using the technology demonstrators	9
2.1	Background: electrostatic control of polarization currents	9
2.2	Modular design	9
2.3	Overview of 8-and 72-element circular machines and the linear accelerator . .	10
2.4	Animating the polarization current	11
2.5	Wedge design for 72 element and 8 element antennas and test:	12
2.5.1	Scope of the design.	12
2.5.2	Final geometry.	13
2.5.3	Features for reproducible manufacturing of elements.	16
2.5.4	Performance of periodic wedges.	17
2.5.5	Measurement data for individual manufactured wedges.	18
2.6	Design of electronics and Labview control software: tests using the 8-element system	18
2.6.1	Vector multiplier and digital control.	18
2.6.2	Circuit assembly for testing.	21
2.6.3	Labview control software.	22
2.7	Design of 72-element electronics and system integration for Technology Demonstrator 1	23
2.7.1	Overall design and integration.	23
2.7.2	72 Element Electronics.	25
2.8	Anechoic chamber and test measurement systems	30
2.9	Test results of 8-element machine: Bluetooth dipoles and dielectric wedges .	32
2.9.1	Test of speed control using an array of Bluetooth dipoles.	32
2.9.2	Tests using the 8-element dielectric antenna.	36
2.10	Design of Technology Demonstrator 2: a superluminal linear accelerator . . .	37
2.10.1	Design of dielectric antenna elements for the linear accelerator. . . .	37
2.10.2	Control electronics for the linear accelerator.	37
2.11	Future experimental work	39
2.11.1	Use of Technology Demonstrator 1: the 72- element circular machine. .	39
2.11.2	Experiments using Technology Demonstrator 2: the linear accelerator. .	39

2.11.3	Technology demonstrator 3: high-power dielectric antenna elements.	40
3	Mathematical and Numerical Physics:	41
3.1	Introduction	41
3.2	Numerical visualizations of the Liénard-Wiechert fields of superluminal sources.	41
3.2.1	Superluminal charges in rectilinear motion.	41
3.2.2	Superluminal charges in uniform rotation.	43
3.3	Mathematical Physics	49
3.3.1	The fundamental role of the retarded potential in the electrodynamics of superluminal sources.	49
3.3.2	Rigid rotation of the polarization currents due to a rotating magnetic field.	50
3.3.3	Spectral properties of the nonspherically decaying radiation generated by a rotating superluminal source.	51
3.4	Retarded-time solutions	51
3.4.1	Statement of the problem.	51
3.4.2	The immediate future.	53
3.5	An extended rotating source	53
3.5.1	Superluminal volume sources.	53
3.5.2	Mathematical approach to volume extension.	53
3.5.3	Future development.	54
4	Astrophysics	54
4.1	Introduction	54
4.2	Pulsar frequency spectrum	55
4.2.1	Application of superluminal emission to the Crab Pulsar.	55
4.2.2	Extension to other pulsars.	56
4.3	Pulsar flux versus distance relationships	57
4.3.1	Introduction.	57
4.3.2	Overview of data used in the analysis.	59
4.3.3	Observed cumulative distribution functions.	59
4.3.4	Maximum likelihood evaluation of pulsar luminosity function.	61
4.3.5	Bayesian statistical analysis.	64
4.3.6	Future work.	64
4.4	The Lick Observatory Gamma-Ray-Burst Afterglow Experiment	64
4.4.1	Introduction.	64
4.4.2	The initial setup made in late July of 2008.	65
4.4.3	Observations.	66
4.4.4	Where we are now and where we might go.	66
4.4.5	The 30-inch Hands-on-Universe Telescope.	67

5 Outreach to sponsors	67
5.1 Introduction	67
5.2 Oxbridge Pulsar Sources Ltd.	68
5.3 Commercialization	68
5.4 Other issues	68
5.5 DOE Intelligence	69
5.6 DARPA	69
5.7 Raytheon and L-3	69
5.8 USAF radar solicitation	70
5.9 NASA	71
5.9.1 Astrophysics Data Analysis.	72
5.9.2 Astronomy and Physics Research and Analysis.	72
5.9.3 Astrophysics Theory.	72
5.10 NASA Deep Space Network	72
5.11 CIA and others	73
5.12 Other outreach	73
5.12.1 Conference summaries	73
5.12.2 Talks, seminars and colloquia	73
6 References and publications	74

Eighteen-Month Report on LDRD 20080085 DR: Construction and Use of Superluminal Emission Technology Demonstrators with Applications in Radar, Astrophysics, and Secure Communications.

1. Introduction

1.1. History

Between 2004 and 2007, LANL-sponsored experimental [1, 2] and theoretical [3, 4, 5] work directed by the PI of the current program established that polarization currents can be animated to travel faster than the speed of light *in vacuo* and that these superluminal distribution patterns emit tightly focused packets of electromagnetic radiation that are fundamentally different from the the emissions of previously known sources. The work, which was developed from proposals by Ginzburg and colleagues in the early 1970s [6, 7] involved numerical and mathematical studies of radiation sources that exceed the speed of light [3, 4, 5], carried out in collaboration with H. Ardavan of the University of Cambridge. In addition, verification experiments were performed using a proof-of-principle apparatus built at Oxford University (in collaboration with A. Ardavan) using funds acquired by the PI in the UK (Fig. 1 [1, 2]).

Although resources were limited, the studies in the period 2004-2007 demonstrated that man-made superluminal sources have great potential for applications relevant to radar [8], medical and directed-energy technologies [2], as well as long-range communications [1]. In addition, the numerical work showed that phenomena seen in astronomical observations of pulsars might be attributable to emission by a rotating superluminal source [3]. In parallel with the US/UK work, a team at Sarov used the ISKRA-5 laser to demonstrate emission by superluminal polarization currents, verifying the fundamental physics involved [9, 10].

These developments [11], and the potential for scientific and technological advances in a promising but little-explored field formed the basis of the present program, which covers three areas:

- (i) the construction of next-generation practical superluminal sources to serve as technology demonstrators for radar, directed energy, and communications applications, as experimental verification for calculations and as ground-based astrophysics experiments (pulsar and gamma-ray burst simulators);
- (ii) analytical and numerical calculations of both man-made and natural superluminal sources; and
- (iii) the search for natural superluminal sources using astronomical observations.

Before expanding on the proposal, we shall briefly review some of the physics necessary to understand superluminal emitters.

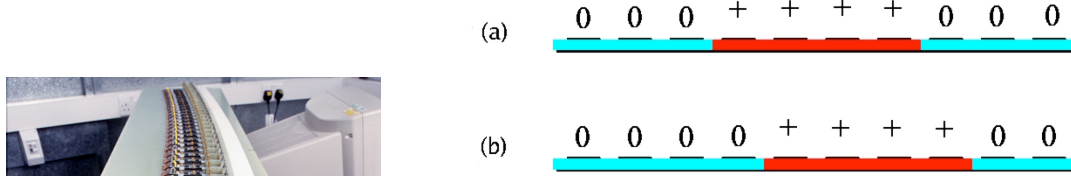


Figure 1. Left: the proof-of-concept superluminal source built at Oxford University [1, 2]. The white strip is a 10-degree arc of a 10.025 m radius circle of alumina; this dielectric contains the polarization currents. The copper ground plate is visible beneath the alumina; the amplifiers that drive the upper electrodes (covered by a G10 plate) are to the left. Right: principle of animating a polarization current. At time t (a), voltages are applied to some of the electrodes atop the dielectric, producing polarization. At time $t + \Delta t$ (b), one electrode has been switched off and another switched on, moving the polarization along the dielectric.

1.2. Some general points about superluminal sources: multivalued retarded times and temporal focusing

Though a radiation source that exceeds the speed of light may sound like a violation of Special Relativity, the universal speed limit does not apply to a polarization current, since the carrier of the current is a *pattern of electric polarization*, rather than charged particles [4, 11, 12]. Such a pattern may be made to move faster than light by the coordinated subluminal motion of charged particles [11]. No laws of physics are broken and Maxwell's equations, which are necessarily relativistic, can be used to predict the emitted radiation [4, 12].

A remarkable aspect of a radiation source that exceeds its own wave speed is that the relation between retarded (source) and reception times need not be one-to-one: multiple retarded times may contribute to a single instant of reception [4, 11, 12]. Whilst a full mathematical treatment is beyond the scope of this general introduction, some examples of multivalued retarded times from superluminal sources may be visualised simply using Huygens wavelets [11]. Fig. 2a shows a source with a constant superluminal velocity. (The diagram will be familiar to anyone who knows of the Čerenkov effect; in this case, however, the source is travelling faster than the speed of light *in vacuo*, leading to so-called *vacuum Čerenkov radiation* [11].) The envelope of the emitted Huygens wavelets is a cone; an observer outside the envelope cannot see the source, whereas one inside it can see two distinct

images from the source's history (*i.e.*, two retarded times— note the intersecting wavlet circles). It is worth noting that the first demonstration that the apparatus in Fig. 1 functions as a true superluminal source involved the detection of vacuum Čerenkov radiation emitted at an angle that depended only on the speed of the source [1, 2].

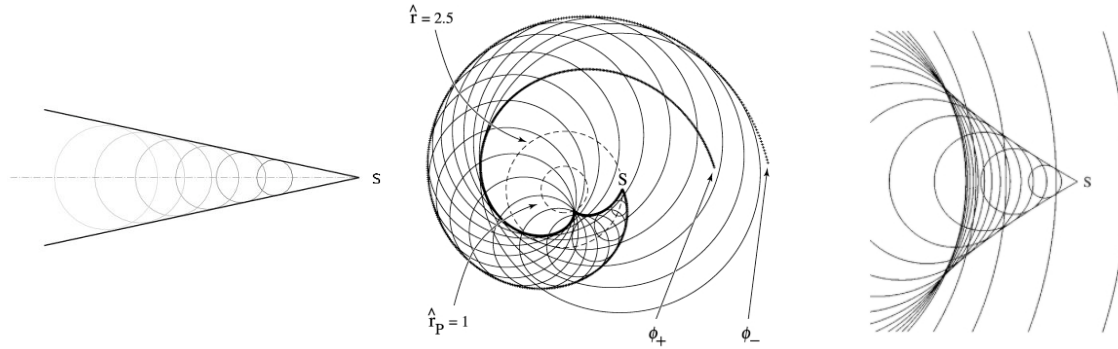


Figure 2. Huygens wavelets (light curves) and their envelopes (dark curves) for superluminal sources: (a) constant velocity, (b) centripetally accelerated, and (c) linearly accelerated. In (b), the cusp is where the two sheets fold in to meet on the inner dashed circle; in (c) the cusp occurs on either side of the source's track, where all of the Huygen's wavelets intersect.

The situation becomes even more unusual when the superluminal source also accelerates. Fig. 2b shows a superluminal source moving in a circle; here, the acceleration is centripetal [4, 12]. The Huygens wavelets now form a Čerenkov envelope consisting of an asymmetric two-sheet structure. It is relatively simple to show that an observer within the envelope will see an odd number (3, 5, 7, ...) of images of the source (*i.e.*, an odd number of retarded times), the exact number depending on the source speed [3]. The most remarkable effect, however, occurs where the two sheets meet tangentially on a cusp curve (Fig. 2b); an observer at this point will receive instantaneously contributions from an *extended period of source time* [2, 4, 12]. This unique effect, demonstrated experimentally by the machine shown in Fig. 1 [1, 2], represents *focusing of radiation in the time domain* to produce a concentration of electromagnetic energy. The initial work indicates that this *temporal focusing* has possible applications in radar [8] and long-range, low-power, secure communications.

A related effect occurs when a source undergoes linear acceleration (Fig. 2c); here, there is an extreme concentration of emitted radiation caused by temporal focusing in a ring around the source's path [13]. Our studies suggest directed energy applications for such a source.

1.3. The path onwards

1.3.1. The technology demonstrators. Whilst the original apparatus was useful as a proof-of-concept, it was large, unwieldy and based on analogue technology [1]. One of the main purposes of the current proposal is therefore to create three technology demonstrators for superluminal emission; these machines, plus an additional 8-element dielectric antenna that serves as a test-bed, are summarized in Table 1.

The technology demonstrators employ modern digital signal synthesis and are much smaller than the proof-of-concept machine [1], demonstrating the scalability of the technology to organizations interested in commercialization. In addition, some will serve as ground-based astrophysics experiments, simulating pulsars (Technology Demonstrator 1) and gamma-ray bursts (Technology Demonstrator 2). The compactness of the new machines also allows them to be run in the well-characterized environment of the radio-frequency anechoic chamber constructed by ISR-6 at TA-53 for many experiments, whereas the original apparatus was used outside, resulting in the complication of ground reflections [2].

Machine Status	Form	Elements	Purpose
TD 1 Being assembled	Full circle 125 mm radius	72	Astrophysics experiments Long-range communications Phase-front studies (radar)
8-element Complete, in use	40° arc 125 mm radius	8	Test-bed for TD1 components Cusp formation High frequency work
TD 2 Designed, part built.	Linear accelerator	24	Directed energy. Fundamental physics: gamma-ray bursts
TD 3 Preliminary design	High power elements (linear)	~ 5	Directed energy

Table 1. The machines; TD is short for Technology Demonstrator.

Section 2 describes the detailed design work for the new superluminal sources, plus initial test results.

1.3.2. Mathematical and numerical work. Though Maxwell's Equations are necessarily relativistic, their solution for a source traveling faster than the speed of light is nontrivial. As we have already seen, unlike the case of a subluminal source, multiple retarded times must be considered [2, 4, 12]. In addition, there are divergences in the fields to be handled [4, 12]. The modeling of the experimental superluminal sources and the astronomical observations [3, 14] therefore demands a considerable amount of mathematical groundwork; sources that move faster than their own wavespeed have been little considered thus far, and the field is at a very early stage of development [11]. Therefore, this program develops the mathematical framework required for treating superluminal sources and studies the numerical techniques necessary to solve some of the intractable equations encountered. This aspect of the program is discussed in Section 3.

1.3.3. Astrophysical work in the program. As noted above, we have suggested that the emission from pulsars and other astrophysical objects may involve superluminal sources [3]. A core aim of the project is to develop this idea using analysis and/or modeling of existing observational data. As discussed in Section 4, by these means we have recently shown that the superluminal model is able to account *both* for the emission spectrum and the intensity/distance relationship of pulsars. There is also an observational component to the program, and Section 4 describes the use of a fast detector on a mid-sized telescope to search for evidence of superluminal emission in gamma-ray-burst afterglows.

1.3.4. Commercialization. Section 5 describes plans for commercialization of superluminal technology.

2. Building and using the technology demonstrators

2.1. Background: electrostatic control of polarization currents

Whilst the competing Russian group demonstrated the feasibility of superluminal emission using polarization shock waves in a plasma generated by the ISKRA-5 laser [9, 10], the method promoted by the LANL group is based on electrostatic control and animation of the polarization current, a technique that is far more amenable for useful and controllable devices [2]. Fig. 1 (Right) shows the basic principle: A series of electrodes is placed above a dielectric (such as alumina) mounted on a ground plate. The application of voltages to the electrodes creates a polarized region underneath; this can then be moved by switching the voltages on the electrodes on and off [1, 2]. Given the sizes of practical devices ($\sim 0.1 - 1$ m), superluminal speeds can be readily achieved using switching speeds in the MHz-GHz range (timings in the 10s–100s of picoseconds) [2, 11]. Far more subtle manipulation of the polarization current is of course possible by controlling the magnitudes and timings of the voltages applied to the electrodes [2].

2.2. Modular design

The individual amplifiers driving the electrodes of the proof-of-concept superluminal source are clearly visible in Fig. 1, illustrating that identical, modular units can be used to control the polarization currents. We are building on this modular approach for the proposed technology demonstrators (Table 1) using common electronic modules for all machines. As will be noted below, the dielectric antenna elements are also quite modular, leading to streamlining of design work. In the following sections we will give a more detailed explanation of the rationale behind the machines being built at LANL.

2.3. Overview of 8-and 72-element circular machines and the linear accelerator

As in the case of the proof-of-concept apparatus, the mechanism for building superluminal sources appears directly in the Ampere-Maxwell equations [2]:

$$\nabla \times \mathbf{H} = \mathbf{J}_{\text{free}} + \frac{\partial \mathbf{D}}{\partial t} = \mathbf{J}_{\text{free}} + \epsilon_0 \frac{\partial \mathbf{E}}{\partial t} + \frac{\partial \mathbf{P}}{\partial t} \quad (1)$$

The two terms in Eq. 1 that are sources of electromagnetic radiation are \mathbf{J}_{free} and $\partial \mathbf{P} / \partial t$. The free-current density \mathbf{J}_{free} consists of charged particles such as electrons; it is the basis of conventional sources such as aerials and synchrotrons [15]. All known charged particles possess rest mass and so cannot move faster than the speed of light. However, there is no corresponding restriction on the polarization current, $\partial \mathbf{P} / \partial t$ [7, 11]. Thus, a superluminal “antenna” can be built by manipulating polarization currents so that they move faster than the speed of light.

The superluminal antennas at LANL are built by using an array of external electrodes to induce a polarization pattern in a dielectric, and then varying the oscillations on the different electrodes so that the polarization current moves faster than the speed of light in vacuum [1, 2]. This is illustrated in Fig. 1(a) and (b); a moving polarized region can be created by varying the voltage on an array of electrodes. As mentioned in the Introduction, many of the interesting properties of superluminal emission occur when the source is accelerating in addition to moving faster than the speed of light. The first two superluminal sources built at LANL provide a rotating superluminal polarization pattern (Table 1). Here, the geometry of the dielectric constrains the polarization distribution to a path which is a circle or the arc of a circle, resulting in centripetal acceleration.

Technology Demonstrator 1 has a 72 element full-circle dielectric antenna, spanning 360°; a schematic is shown in Fig. 4, and work on the associated electronics is discussed in section 2.7. As this report is being written, the 72-element machine is under construction, with around 20 dielectric antenna elements made and a substantial proportion of the electronics assembled. However, an 8-element prototype, which spans a 40° arc of a 0.125 m radius circle, has already been under operation for some time (Table 1). This represents $\frac{1}{9}$ of the 72-element source, and the antenna design and electronics are common to both machines, allowing components and software to be debugged whilst the 72-element source is being built. Experimental results from the 8-element source are discussed in Section 2.9, and a picture of the assembled antenna is shown in Fig. 34.

Whilst Technology Demonstrator 1 is somewhat analogous to a synchrotron, Technology Demonstrator 2 will be a linear accelerator of polarization current (Table 1). The design work for Technology Demonstrator 2 is complete; the acceleration (in the same direction as the motion) is produced by the electronics, one third of which has already been built and tested. This machine is discussed in Section 2.10.

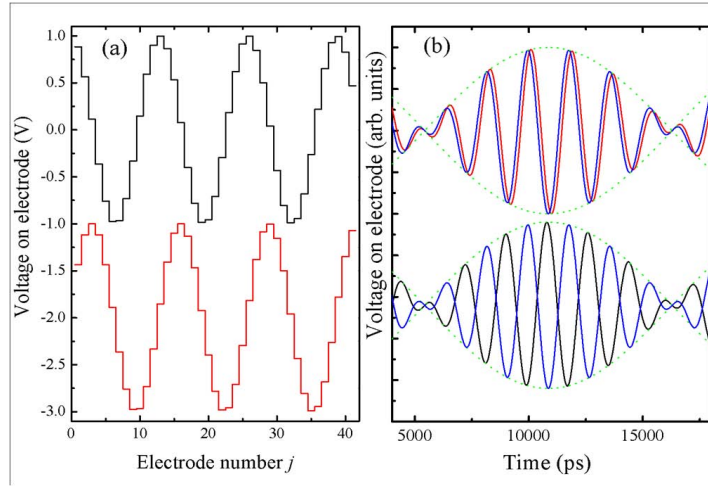


Figure 3. (a) Voltage on each electrode at two different times showing movement of a discretized sinusoidal wave of polarization. (b) The upper plot shows the time dependence of the voltage on two adjacent electrodes, and the lower plot shows the time dependence of the voltages on two electrodes that are 6 steps apart (After Ref. [2]).

2.4. Animating the polarization current

A single mode of a polarization distribution that is both rotating and oscillating in time is described by [4, 12]

$$\mathbf{P}(r, \varphi, z, t) = \mathbf{s}_{r,\varphi,z}(r, z) \cos[m(\varphi - \omega t)] \cos \Omega t \quad (2)$$

Here \mathbf{s} describes the direction of polarization, the first cosine term causes circular motion and the second cosine provides modulation of the whole polarization. Any arbitrary repetitive rotating and oscillating source can be described as a sum over all integers m in Eqn. 2 [4, 12].

Practical machines are not continuous circles, but built up from elements subtending a few degrees, each energized by a separate amplifier (see Figs. 1 and 4, and Table 1). In the 8 and 72 element machines, each element or “wedge” subtends an angle $\Delta\varphi = 2\pi/72$ radians $= 5^\circ$. Hence, a discretized version of Eq. 2 is used to give the voltage applied to the electrode of the j th element [1, 2]

$$V_j = V_0 \cos[\eta(j\Delta t - t)] \cos \Omega t. \quad (3)$$

Here η is an angular frequency providing the motion of the polarization current, and Ω is, as before, a master modulation angular frequency that is present to provide additional beam steering [2].

Fig. 3 illustrates how this approach (*i.e.* a set of discrete antennas with slightly different phases) can simulate a smoothly rotating source. As long as the phase variation is not too rapid, theoretical work has shown that the radiation pattern from such a discretized source is almost identical to that of a continuous source [4, 12].

In order for eqn. 3 to simulate eqn. 2, $\eta = m\omega$ and $\Delta t = \Delta\varphi/\omega$. Here there is a subtle difference between a full circle machine such as Technology Demonstrator 1 and an antenna that is only the arc of a circle [4, 12]. For full circle antennas, the rotating pattern should

be continuous (*i.e.* contain no discontinuities) both spatially and in the time domain; this restricts m to integer values. Antennas that form an arc of a circle, such as that in the 8 element machine, have no such restriction, and m can take any value [2].

The speed of the source (*i.e.* the instantaneous velocity of the rotating polarization pattern) is $V_{\text{rot}} = a\omega$, where a is the radius of the antenna; this can also be expressed as [2]

$$V_{\text{rot}} = a \frac{\Delta\phi}{\Delta t} \quad (4)$$

The electronics used to generate these signals, discussed in Section 2.6, set the *phase* of the signal, and not the time delay. The relation between the time delay and the phase is given by

$$\Delta t = \frac{\Delta\phi}{360 * f}, \quad (5)$$

where $\Delta\phi$ is the phase difference between adjacent elements, in degrees, and $f = \frac{\eta}{2\pi}$ GHz is the carrier frequency.

2.5. Wedge design for 72 element and 8 element antennas and test:

2.5.1. Scope of the design. The scope of the superluminal antenna design work is to find a configuration (Figure 4) that will generate polarization currents in a dipole pattern with radial orientation on the periphery of a circular antenna.

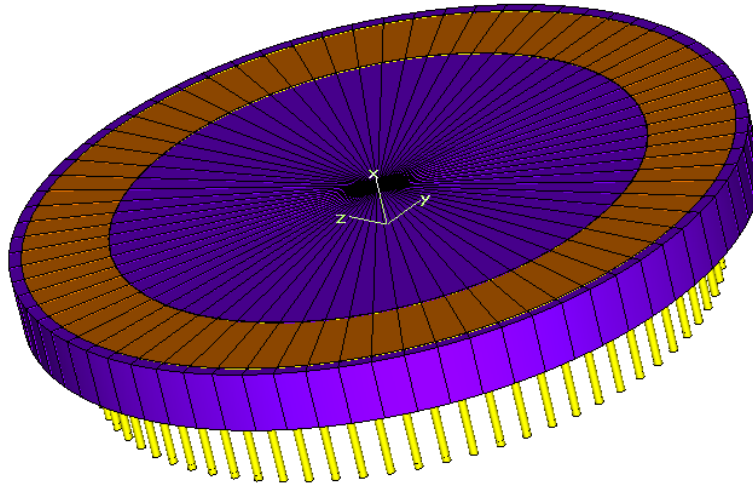


Figure 4. Full model of the superluminal antenna: This antenna consists of 72 wedge-shaped elements, each spanning a 5-degree range of the circle. The structure is driven by 72 individual coaxial channels (yellow) from the bottom. The polarization current inhabits the alumina ring (brown) on top of the antenna.

The antenna has 72 individual drives that allow voltages corresponding to Eq. 3 to be imposed on each element. The carrier frequency $f = \eta/2\pi$ for the radiation pattern was chosen to be close to 2.4 GHz; this facilitates tests on outdoor ranges, as will be described below. Modulation frequencies $\Omega/2\pi$ of up to 200 MHz are imposed; these are used to steer the beams from the machine [2]. Thus the transmission has to be broadband with a total range of 20%, to avoid reflections back into the driving electronics.

There are several challenges to overcome.

- (i) The drive signals are generated and transported to the antenna in coaxial lines. Thus, each of the 72 wedges must provide a transformation from a circular TEM mode to a dipole radiation pattern. While this type of drive is common in accelerator structures or other resonant circuits, where TEM modes feed into eigenmodes of a totally different pattern, a more complex, field-shaping geometry is required for what is in effect an open antenna.
- (ii) Sufficiently strong polarization currents require dielectric material at the exit from the antenna to free space, which represents a large impedance mismatch from a few 10s of Ω s inside the dielectric to 377Ω in free space. The design needs to find a compromise between selecting a material of a sufficiently large permittivity (to obtain a strong polarization due to the dipole field [2]) and a reduction of the reflection at the mismatch. Mismatch conditions also need to be considered at the transition from the 50Ω coaxial cables to the propagation region.
- (iii) To generate the dipole pattern, distinct anode and ground electrodes need to be provided in the region where the dipole mode pattern is propagating. This requires a break in the conduction path between opposite sides of the propagation region. This requirement conflicts with the need to shield the fields from radiating out of the antenna anywhere else but the top of this region. The break for the RF wall currents, while exhibiting very low leakage of RF-fields is a major design driver.
- (iv) There is a need to impose very accurate timing, amplitude and frequency variations onto the radiation pattern around the circumference of the dielectric circle. This requires a design of the individual wedges that allows high reproducibility of the performance.

2.5.2. Final geometry. To approximate a continuously-traveling radiation pattern around the circumference of the full antenna, the circle is broken up into 72 narrow wedges each subtending 5° (Table 1 and Fig. 4). Each of these elements is driven separately from a coaxial line connected to the driving electronics.

Figure 5 shows the body of a wedge-shaped element made from G10, a machinable, fiberglass-epoxy composite. The cut-out is the propagation region. The coaxial mode couples to this region from the bottom, then it is transformed into a dipole pattern and transported to the top, where it radiates into free space. The cutout is located so that the radius at the center of the polarization region has a length of one wavelength at 2.4 GHz (125 mm).

The critical element for the field shaping transformation from the TEM mode to the dipole mode is a connection of the coaxial inner conductor to one side of the rectangular propagation region (electrode) and the connection of the outer conductor to the other side of this region (ground). This establishes the polarization, setting up the dipole field. The connection to the ground is straightforward due to the good accessibility of the outer conductor. The connection of the inner conductor requires careful shaping to establish a smooth change in impedance, maximizing transmission of the wave into the radiation field.

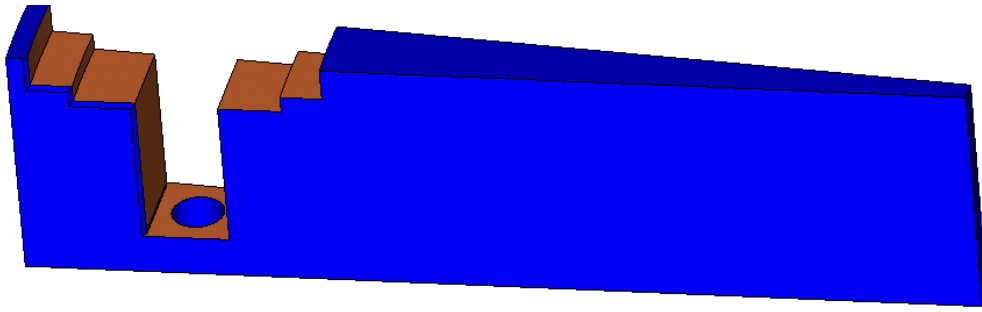


Figure 5. Wedge-shaped individual antenna element: the body is made up of G10 (blue). The cut-out is the propagation region for the dipole mode. The sides of the cut-out are plated (copper color) for shielding purposes.

Fig. 6 shows the shaped center conductor providing a current path from the coaxial inner conductor to one of the side electrodes.

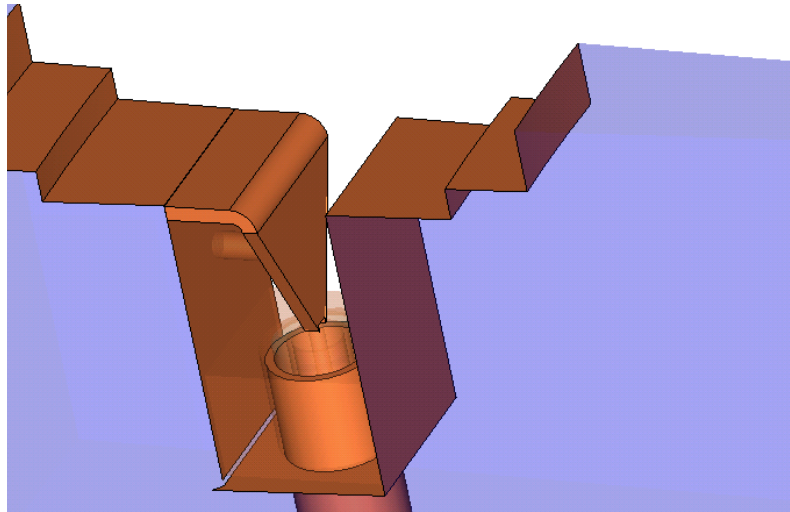


Figure 6. Field shaping element; the coaxial inner conductor is connected to the left side of the plating by an element that shapes the electric field and provides a slow impedance change from bottom to top. The outermost conductor of the coaxial lines contacts the ground at the penetration from the bottom to the propagation region.

The need for maximum shielding of the dipole mode toward the bottom and the sides (in the radial direction) requires an elaborate separation between electrode and ground plating. The electric separation of those two can only allow for a very low amplitude of RF leaking out into the environment, or else the signal from the superluminal emission would be contaminated. The solution was found in a discussion with James Potter from JPAW Accelerator Works [16], who suggested to use a coaxial choke with low field at the location of the break. To implement this we used two concentric coaxial cables. The inner coaxial cable carries the signal into the structure, and the outer cable is shorted at the bottom and has a break in the outer conductor. The distance between short and break is approximately one

quarter of a wavelength.

The two cables are flush at the top, where the full wave exits into the structure. In the outer cable a quarter wave builds up with a null close to the break (see Fig. 7). Only a small portion of the wave radiates out of the break. The propagation region is completely plated to prevent radiation from leaving anywhere else than at the top of the wedge. This plating is only broken in one thin line azimuthally across the wedge. In this configuration, using a break at the coax to minimize leakage and a second break where electrodes needed to be separated, a low leakage has been achieved.

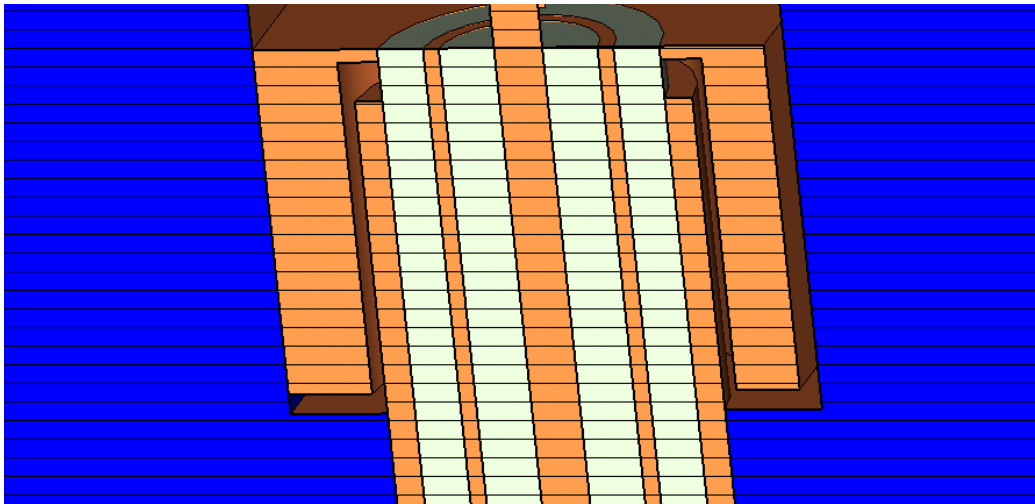


Figure 7. Shielded break in RF-conduction; this cross-section (solids are indicated by hashing) shows the concentric coaxial lines and a shielding block. A gap between the block and the coaxial lines provides the primary break in electrical contact. The block shields the second break between the electrode and ground plating (lower left of cut-out). The low leakage through the breaks can be attributed to the choice of break locations and the effect of the outer (larger) coaxial line, in which a quarter wave builds up with a minimum at the primary break location.

To obtain a propagating polarization current radiating into free space a dielectric medium is used as the top layer of the antenna wedges. It provides field enhancement and is the source of the polarizing charges [2]. For a large amplitude of the radiating dipole field we can either use a dielectric with a high permittivity, or a large volume for the dielectric. A large permittivity aggravates the mismatch between the dielectric top layer and the free space impedance and so we opted for a moderate material (Alumina 99%). To further address the impedance mismatch, we selected a thin slab of dielectric (4 mm) and increased its radial extent to obtain a larger volume. Penetration through the thin slab is better than that for a short but thicker slab. A further improvement was gained by increasing the radial extent of the propagation region up below the slab. Fig. 8 shows the radial cross-section of the top of the antenna.

In order to provide a complete record of the design, Fig. 9 shows other features that help in lowering the RF leakage (a copper block that accepts the concentric coaxial lines), and improving the impedance transition along the propagation path (a shorting pin between the

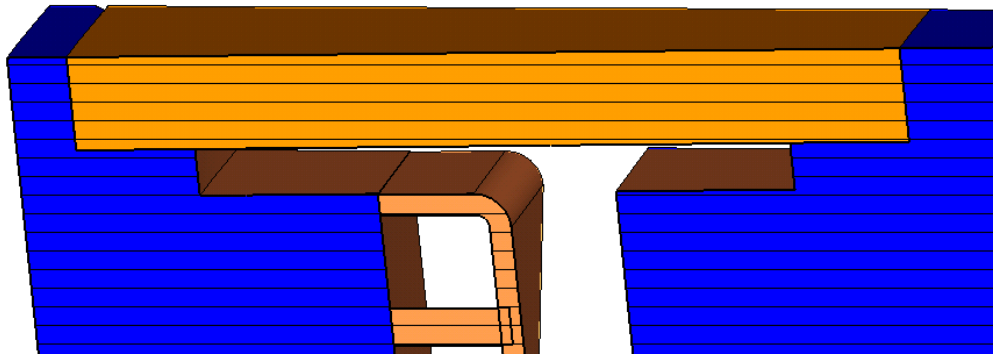


Figure 8. Alumina-filled polarization region: the top of each antenna element is filled with alumina. The dipole field in this region sets up the modulated polarization currents. To minimize impedance mismatch, the slab has been made fairly thin and wide (radially). The increase in radial dimension without a large step in impedance change has been done in two steps, one filled with air and one filled with alumina.

field shaping device and one of the electrodes). These also help with the concern addressed in the following subsection.

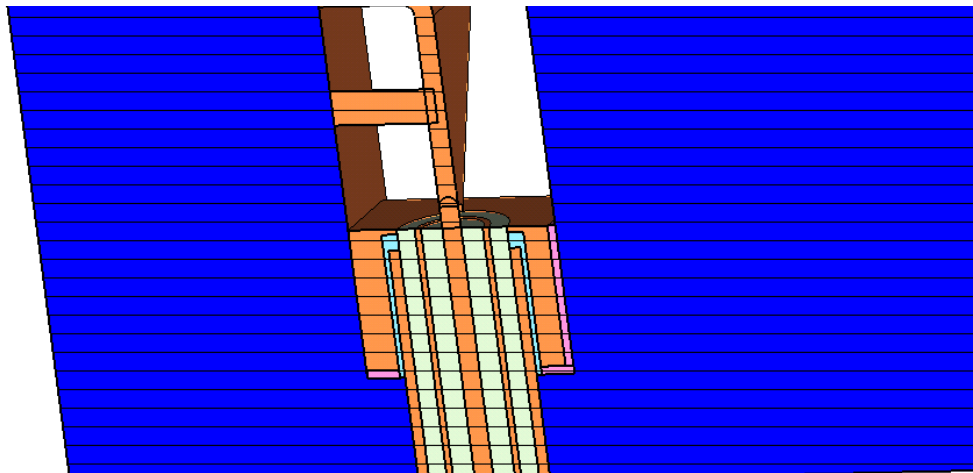


Figure 9. Additional impedance match features: the copper block below the field-shaping element and the pin between the field-shaping element and the electrode are additional features to help the mitigation of impedance mismatches.

2.5.3. Features for reproducible manufacturing of elements. The small features of the wedges make it challenging to make 72 elements that perform reproducibly. For example, the first iteration of the design had smaller coaxial lines and a free-hanging shielding block, but the delicate nature of the components and other handling difficulties resulted in a spread in performance that was too wide. The design presented here has significant improvements that should allow the manufacturing of a homogeneous set of wedges (Fig. 10).

The steps taken are as follows. (i) The shielding block lies on a number of Teflon shims that hold the block in place during soldering. (ii) The coaxial lines have been increased to the maximum possible diameter that can be fitted into a 5-degree wedge. (iii) The larger coaxial lines resulted in a thicker field shaping element that is less fragile. (iv) The shielding block assumed the important role of defining the proper positioning of the coaxial lines with respect to the alumina slab and providing a more stable attachment of the field-shaping element to the inner coaxial conductor.

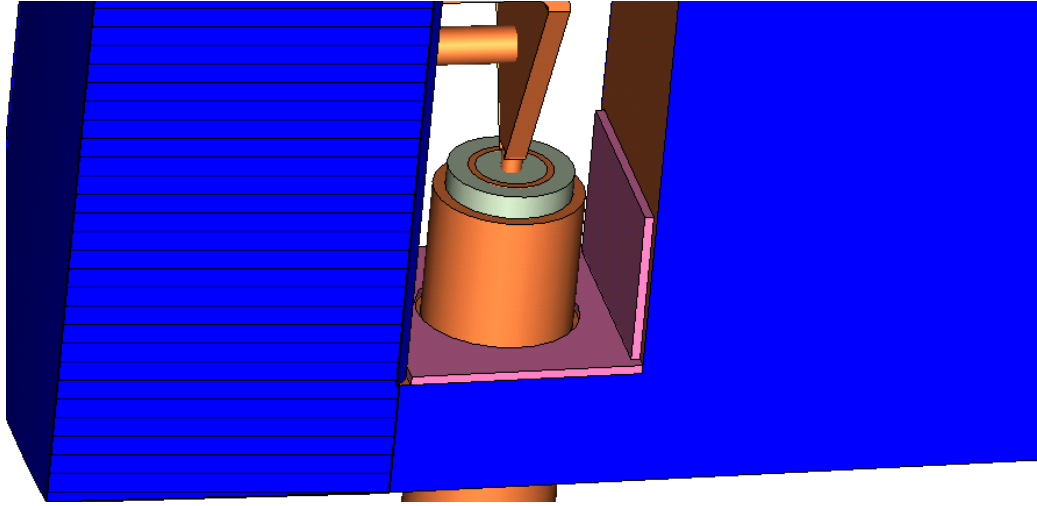


Figure 10. Stability features: the block is held in position by 2 Teflon shims (pink) below and on the left side of the block (block hidden). The mechanical stability and handling during manufacturing has been increased by selecting the largest coaxial lines fitting into the G10-wedges. This choice also improved the stability of the field-shaping element, that needs to be of the same thickness as the innermost coaxial conductor.

2.5.4. Performance of periodic wedges. The simulations of the design have been done with individual wedges whose azimuthal boundaries have been selected to represent a periodic repetition of wedges. The design characteristics were the good transmission of the drive power into the radiation field as characterized by the S_{11} of the driving signal. Fig. 12 shows the range where the return loss is better than -10 dB. The range includes the required band from 2.16 to 2.64 GHz. A snapshot of the electric field amplitude indicates the field shaping from coaxial mode to a radiating dipole pattern (Figure 13).

The simulations have been done with the well benchmarked em-simulator *Microwave Studio* from CST [17]. The software allows a CAD style description of geometries, various ideal or lossy material parameters can be imposed. Boundary conditions include open space, symmetry conditions and periodic boundaries.

The wedges of the latest design were built in-house. Owing to the more delicate fabrication parts, the wedges of an earlier design were built by a company with wide experience of small microwave components for customers such as JPL and NASA (Thomas Keating Ltd., UK) [18]. The lessons learned from the early design and fabrication were crucial

REVISIONS

REV	DESCRIPTION	BY	DATE
X2	ADDED NOTES	BR	5/1/08
X3	ADDED DETAIL F VIEW	BR	1/28/09

NOTES:

- THE NOMINAL ELECTROPLATING THICKNESS IS 0.001 INCHES OF OFF COPPER. THE MINIMUM ACCEPTABLE THICKNESS IS 2 SKIN DEPTHS OR .00034 INCHES.
- SURFACE FINISH TO BE $\sqrt{63}$ OR BETTER.
- THRU HOLE WILL BE MASKED BEFORE ELECTROPLATING.
- ADDITIONAL SUBSTRATES BELOW THE COPPER TO IMPROVE BONDING TO THE G-10 IS ACCEPTABLE.

DETAIL A

DO NOT PLATE CHAMFERED EDGES - MASKING REQUIRED.

MASKING REQUIRED ON BOTTOM OF SIDE WALL. .013 GAP BETWEEN COPPER SURFACES THIS SIDE ONLY

.001 COPPER COATING ON G-10 AS SHOWN SIDE WALL TO SIDE WALL

DETAIL B

.001 COPPER COATING MUST COVER THE ENTIRE TOP SURFACE OF STEPS FROM THE BOTTOM TO THE TOP SIDE WALL TO SIDE WALL - ON OPPOSITE SIDE FOLLOW MASKING INSTRUCTIONS

DETAIL C

.013 GAP

DETAIL D

DETAIL E

DETAIL F
SCALE 2 : 1

Los Alamos NATIONAL LABORATORY

WEDGE COPPER LINER ASSEMBLY

1 XXX		XXXX		XXXX		1	
Qty	Part No. & D. No.	Description	Material	Material	Item No.	Material	Item No.
ISR-6		Classification Of Part: unclassified		Drawing Title Block: unclassified			
Los Alamos NATIONAL LABORATORY							
Name		Date		Tolerance (Unless Otherwise Noted)			
Originated Bill Romero		5/1/08		$x = +1.2/A$ $0.2x = +1.2/A$ $0.25x = +1.00B/\sqrt{\text{inch}}$ $0.64x =$			
Drawn Bill Romero		5/1/08					
Checked		Date		State		Drawing Number	
Approved		15-1		1		LAR-01002X3 B	

THE INFORMATION AND DESIGNS CONTAINED IN THIS DRAWING ARE CONFIDENTIAL AND THE PROPRIETARY OF LOS ALAMOS NATIONAL LABORATORY

Figure 11. Full assembly fabrication drawing

The main information that can be deduced from the measurement of the first 16 wedges in free space is that most of them perform reproducibly (Fig. 14) and are expected to meet the specifications. Measurements in a more appropriate environment are reported in Section 2.9.2.

2.6.1. Vector multiplier and digital control. The phase and amplitude of the voltage sent to each element (wedge) is controlled by using a pair of ADL5390 RF vector multipliers (VM) in the 8-element design; in the 72-element machine these are replaced with the similar (but

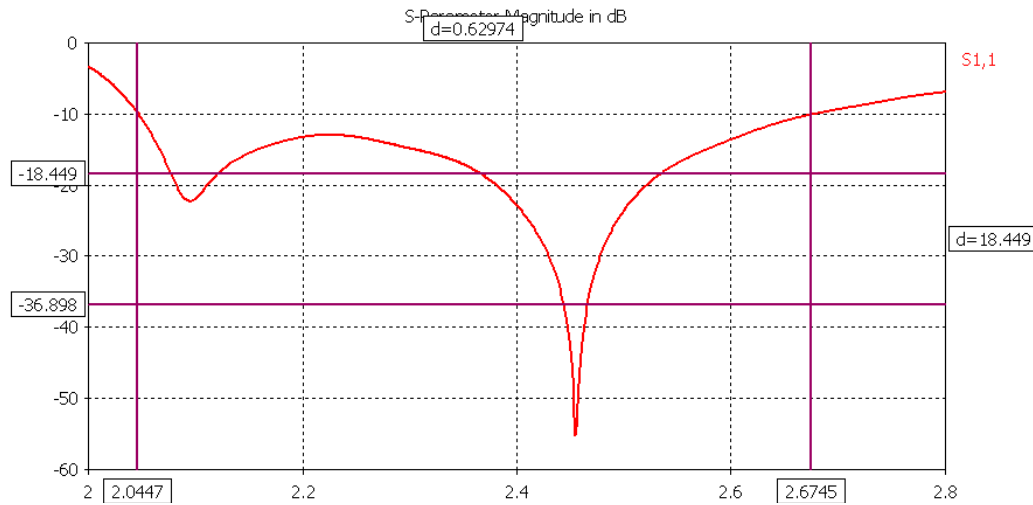


Figure 12. S -parameter analysis for an individual wedge in a periodic environment: a good measure for the suitability of the wedges is the S_{11} parameter that describes reflections from the antenna back into the coaxial drive. Assuming a reflection of -10dB or better as definition for the bandwidth, the wedges have a bandwidth of 630 MHz between 2.04 GHz and 2.67 GHz, which includes the required range of operation from 2.2 GHz to 2.6 GHz or 2.4 ± 0.2 GHz.

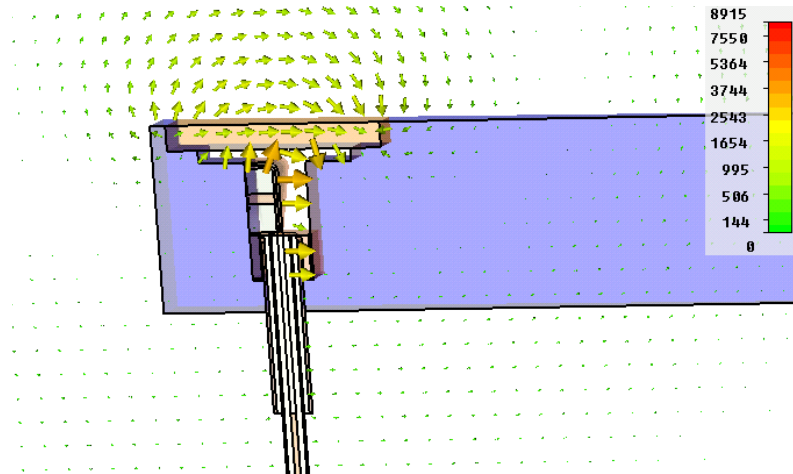


Figure 13. Snapshot of the dipole electric field radiation pattern: the electric field in the central cut-plane shows the field amplitude and direction mostly in the propagation region. The pattern in the coaxial region is not visible due to overall scaling issues. The dipole radiation pattern with only small field contributions (logarithmic scale) elsewhere shows the proper field transformation.

newer) AD8349. A basic schematic of a single VM is shown in Fig. 15. The theory of how these VMs operate is described in detail in Ref. [19], but will be summarized here.

The VM accepts a pair of RF inputs of a single angular frequency ω_1 that have been passed through a 90° splitter. This pair of inputs, which can be described as $\sin(\omega_1 t)$ and $\cos(\omega_1 t)$, are input into RFIN_I and RFIN_Q. The output of the VM is then controlled with the IBBP/IBBM and QBBP/QBBM modulated inputs. Each of these is a differential input that

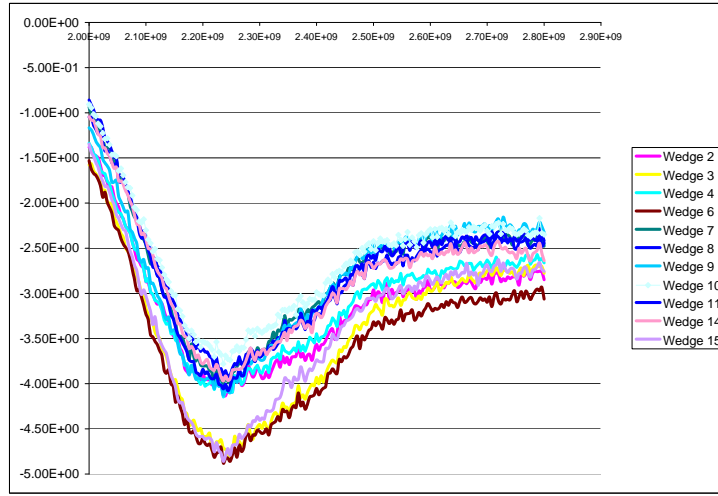


Figure 14. S_{11} -measurement of individual wedges in free space: these are the measurements for the 11 best of 15 wedges built. This indicates good reproducibility of the manufacturing of the wedges. (Note S_{11} is plotted versus the frequency.)

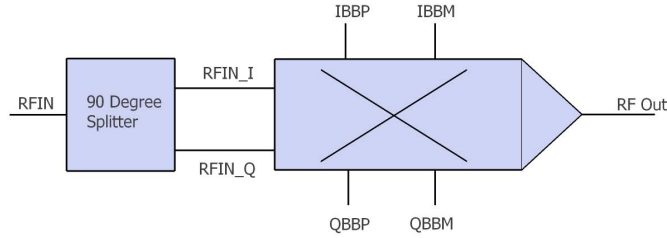


Figure 15. A schematic of the circuit used to generate a single sideband of the RF source on an antenna.

must be centered around a common mode voltage of $V_c \approx 0.5$ V, where $I(t) = \text{IBBP} - \text{IBBM}$ and $Q(t) = \text{QBBP} - \text{QBBM}$. The inputs $I(t)$ and $Q(t)$ can either be DC inputs or RF inputs with a frequency of up to 240 MHz.

The (theoretical) output of the VM is given by:

$$V_{out}(t) = I(t) \sin(\omega_1 t) + Q(t) \cos(\omega_1 t) \quad (6)$$

If $I(t)$ and $Q(t)$ are made to be DC inputs, then the resulting signal, $I_1 \sin(\omega_1 t) + Q_1 \cos(\omega_1 t)$, will have an amplitude given by $A_1 = \sqrt{I_1^2 + Q_1^2}$, and a phase given by $P_1 = \tan^{-1}(I_1/Q_1)$. The phase can be adjusted to a full 360° by including both positive and negative values of I_1 and Q_1 .

For each output channel of the RF source, two different vector multipliers are used to control the magnitude and phase of two input signals with angular frequencies ω_1 and ω_2 , and these signals are added together with a splitter. If the amplitudes A_1 and A_2 of the RF outputs

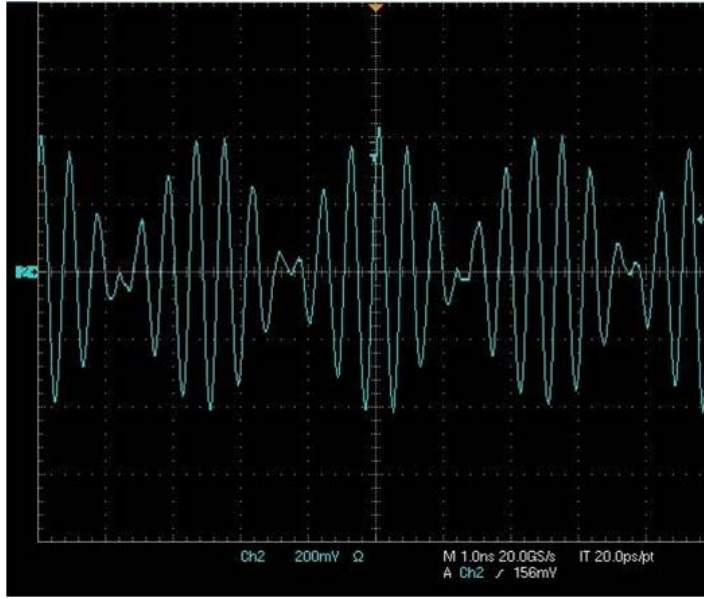


Figure 16. Oscilloscope signal of amplitude-modulated waveform with a 2.4 GHz carrier frequency and 200 MHz modulation frequency.

of the two vector multipliers are equal, than the resulting signal can be described as

$$V_{out} = A [\cos(\omega_1 t + P_1) + \cos(\omega_2 t + P_2)] = 2A \cos \left[\frac{1}{2}(\omega_1 + \omega_2)t + \frac{1}{2}(P_1 + P_2) \right] \cos \left[\frac{1}{2}(\omega_1 - \omega_2)t + \frac{1}{2}(P_1 - P_2) \right]. \quad (7)$$

Thus, the output waveform is the desired modulated signal, as described by Eqn. 3, with a carrier frequency of $\eta = (\omega_1 + \omega_2)/2$, a carrier phase of $P_c = (P_1 + P_2)/2$, a modulated frequency of $\Omega = (\omega_1 - \omega_2)/2$, and a modulation phase of $P_m = (P_1 - P_2)/2$. In order to create an oscillating superluminal source [2], we hold the modulation phase on each antenna constant, while varying the carrier phase from antenna to antenna according to Eqn. 5.

Fig. 16 shows an output waveform from one of the control modules of the 8 element test machine. The signal is clearly of the correct form (compare with Eqn. 7). Fig. 17 shows the equivalent measured frequency spectrum; as desired, the 2.2 GHz and the 2.6 GHz amplitudes are almost equal, and contributions at other frequencies are suppressed by more than -30 dB.

The modulation and carrier phases P_m and P_c are controlled by setting the phases of each individual sideband, P_1 and P_2 , which are in turn controlled by the four inputs I_1 , Q_1 , I_2 , and Q_2 . The external control of the I and Q inputs is accomplished by using Linear Technologies LTC1990 digital to analog converters (DACs). Each individual DAC has eight outputs, which can control the four DC I and Q inputs for a single output waveform (each I and Q input require two voltages to maintain an 0.5 volt offset). These DACs are controlled by serial communication from an 8051 processor, and can be daisy-chained so that (for example) the 72 elements required for Technology Demonstrator 1 can be controlled from a single processor.

2.6.2. Circuit assembly for testing. For flexibility, the initial implementation of the control circuitry was done using discrete components (e.g. quad splitters) and vector multiplier

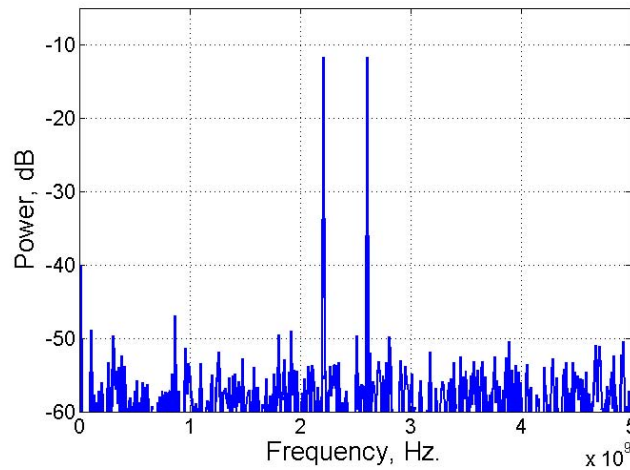


Figure 17. The frequency spectrum of the signal from our 8 element circuit.

evaluation boards connected using SMA connectors and flexible coax cables. The 8-channel control system for the 8-element machine is constructed in this way. Whilst the evaluation boards are very convenient, the manufacturer’s desire that they be “all things to all people” leads to some redundant features and less-than-optimal performance. As will be described below, the subsequent machines employ optimized printed-circuit boards.

2.6.3. Labview control software. A scalable‡ LabVIEW amplitude and phase control routine was developed to accurately control the circuits. From the start, inadequacies in the vector multiplier evaluation boards that were used for the 8 element design proved to make the ideal equations (Eqn. 6) for setting gain and phase ineffective in some regions. Further investigation of the evaluation boards themselves showed that the input traces had not been properly impedance matched during construction, causing a phase shift along the trace. However, by assuming a non-ideal phase angle, a set of approximate equations for gain and phase were developed to set the desired amplitude and phase output. The LabVIEW program first uses these equations to set the amplitude and phases, and then iteratively compensates for additional errors until the desired phase and amplitude has been reached. In this way, software compensates for less-than-ideal components.

This approach does of course require monitoring of the signal sent to each element. The signals on each element can therefore be measured using a Tektronix TDS 7404 digital oscilloscope. A coupler attached to each element takes $\frac{1}{10}$ of the RF power into a binary network of relays that is digitally controlled to compare any of the element signals with a reference signal using two channels of the oscilloscope. The TDS 7404 can sample two channels at 10 GS/s (*i.e.*, 10^{10} samples per second), which is more than adequate for the maximum frequency of 2.6 GHz used. The LabVIEW program measures the phase of each sideband by taking the FFT of a large sampling time of data resulting in a resolution of a

‡ In this context “scalable” means that the same LabVIEW routines can be used in the control programs for the 72-element Technology Demonstrator 1 and the 24 element Technology Demonstrator 2.

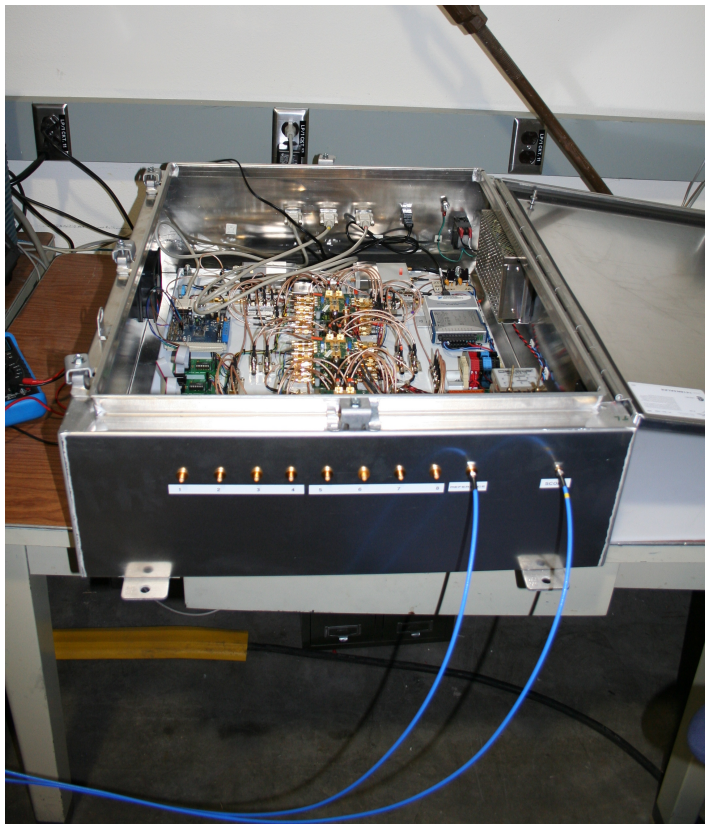


Figure 18. Photograph of the electronics used to generate the phase controlled, modulated signal for the 8-element machine.

fraction of a degree. This was shown to be better than the resolution that could be achieved by looking at the signal directly in the time domain.

In the Technology Demonstrators, the connection between the antenna elements, vector multiplier boards and phase measuring system is made using identical circuit boards and a minimum of cabling. However, the 8-element machine is constructed from discrete components cabled together. Hence, the 8 signals have slightly different path lengths between the antenna element and the oscilloscope, leading to phase errors as large as 20° and amplitude errors of 0.7 dB. The difference in phase and amplitude between the oscilloscope and the antenna are measured, and these values are directly compensated for in the LabVIEW code. This error compensation method reduces the error in phase to $\leq 2^\circ$, and the amplitude errors to ≤ 0.3 dB. It could also be used to compensate for non-identical circuit boards in the Technology Demonstrators.

Fig. 18 shows a photograph of the electronics used to generate the phase controlled, modulated signal for the 8 element machine.

2.7. Design of 72-element electronics and system integration for Technology Demonstrator 1

2.7.1. Overall design and integration. The overall design for Technology Demonstrator 1 has several key points which are based on lessons learned from the original RF Source built

and tested at Oxford (Fig. 1 [1, 2]). The source must be portable and compatible with indoor and outdoor operation. The source should be controlled from a single personal computer that has a simple user interface. The RF electronics and antenna should be closely coupled. The antenna should have a mount that is rugged, portable but also highly accurately pointable and controllable. The system must operate with low power consumption for operation outdoors (*e.g.* supplied by an inverter powered by a truck battery). The final machine should basically be a plug and play instrument for astrophysicists and radar jocks in the field.

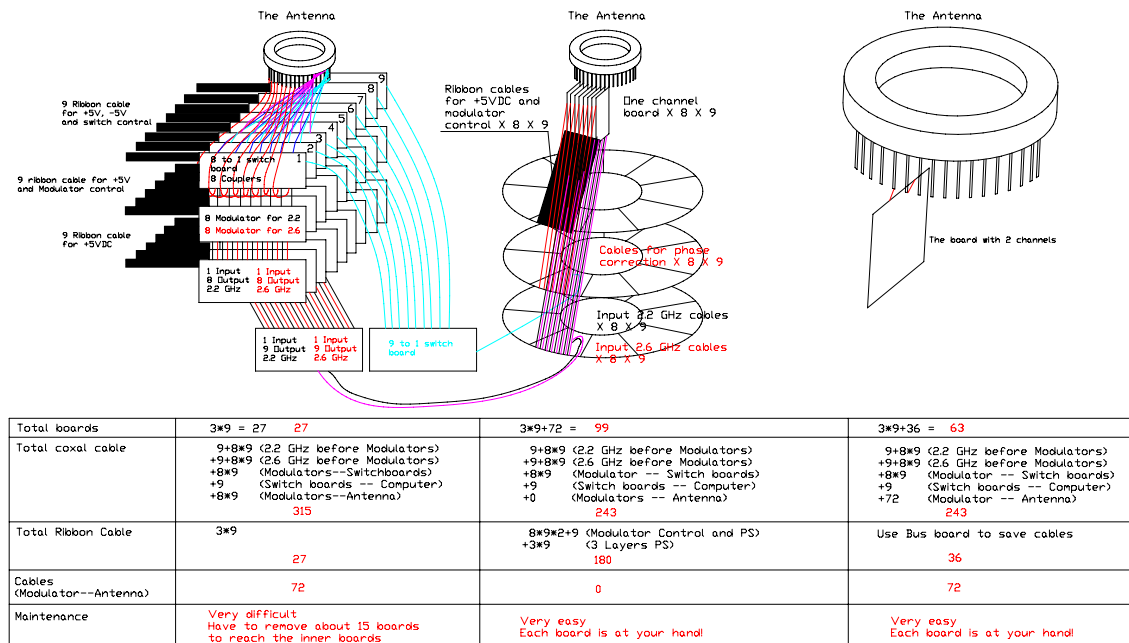


Figure 19. Machine configurations and options for integration.

The dimensions of the circular antenna dictated the machine design. The weight of the machine limited the choice of pointing and mounting system. The RF system was complicated by coaxial cabling and the requirement of phase matching of channels. The drawings in Fig. 19 show a design trade-off study made in the design process.

The design on the left shows a minimum of printed circuit boards (PCBs) located in an RF box and many coaxial cables for connections. This design separates the RF electronics from the antenna. RF shielding is better but maintenance in the field is more difficult and the large number of flexible cables is a headache for precise phase control (see the previous section). The center design is the “wedding cake” concept where the PCBs are integrated in layers feeding the RF outputs to the antenna; the phase control and measurement are partly via rigid coax and tracks on PCBs, reducing potential errors. The design on the right is a variation of the wedding cake to reduce the total number of PCBs. A balance was chosen between mechanical design, maintenance, cabling and weight, plus attractiveness to future sponsors (*e.g.* does it look like something that could hang off the wing of an airforce jet?). Fig. 20 shows a schematic of the machine.

The design of the RF electronics has the oscillators in the rear, the distribution boards

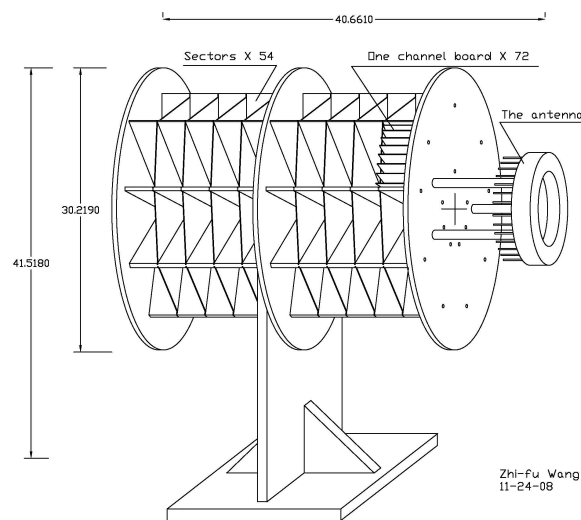


Figure 20. Schematic of Technology Demonstrator 1, showing support stand for RF electronics and antenna.

in the middle and the amplitude and phase control PCBs as close to the antenna as possible. There is a center mechanical support that holds all of the boards in place. There are PCBs used as bus boards to provide the interconnections. The mounting feature is used to connect to an alt-azimuth antenna positioner that is computer controllable. The mount is shown in Fig. 21.

2.7.2. 72 Element Electronics. The electronics system design for Technology Demonstrator 1 involves almost 100 compact custom printed circuit boards (PCBs) located in a mechanical structure as close to the antenna as possible to reduce phase errors. The design for a 72 channel RF system is divided into 9 sections with 8 channels in each section. There are 9 Bus Boards that connect the individual PCBs together to form the system. The goal is to have 72 RF channels with identical performance in amplitude, phase and spectral content that drive the 72 elements of the antenna. Each individual RF channel will be phase controlled from the LabView program described above.

The RF system design was based on using all commercial off the shelf (COTS) components. As mentioned in the previous section, the first 8 channels were constructed using packaged components with SMA connectors and coaxial cables; at the heart of this system are the Analog Devices vector multiplier evaluation PCBs. In this way a proof-of-concept 8 channel system was built and tested. The final 72 channel system uses custom PCBs that were designed in house at LANL and fabricated by Advanced Circuits Corp [20]. All the RF components used in the custom PCBs were surface mount versions of the packaged components used in the 8 channel prototype. Figure 22 shows a photograph of a model of the 72 channels, PCBs, interconnections and antenna. The custom PCBs were designed using the commercial software PCB Artist. Each board uses careful layout to maintain equal signal paths to allow easier phase control of the 72 channels. Each PCB is four layers and has strict

PRECISION PAN-TILT UNIT

High-speed positioning of heavy payloads

Model PTU-D300

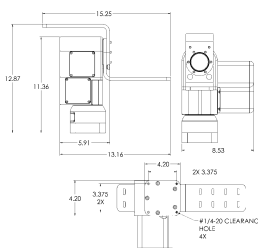
Rugged, Compact, Feature-rich

The PTU-D300 is a family of modular computer-controlled pan-tilt units designed for fast, accurate positioning of heavy payloads. It provides high torque rated for payloads up to 70 lbs while maintaining speed, precision, and a very small form-factor. It offers multiple mounting options and a single connection point. It is designed for demanding applications that require high duty-cycles and long-life in harsh all-weather environments. Key features include:

- Rigid design provides steady images in windy environments
- Solid and vibration-tolerant for vehicle-mounted applications
- Large payload capacity (35 lbs. top-mount; 70 lbs. side-mount)
- Wide-range of pan speeds (< 0.0064°/sec. to 100°/sec.)
- Extremely precise positioning (0.0064° with microstep) allows translating object positions to global coordinates accurately
- 360° continuous-pan including pass-through for many payload types (Video, IR, Microwave, Laser)
- Single connector for all video, control, power
- Flexible payload mounting (top or side)
- Precise control of position, speed & acceleration
- Simple control from host computer via RS-232/485
- Fully sealed for outdoor/marine applications (IP67)

Applications:

- Long-range surveillance
- Antenna positioning systems
- Satellite communications systems
- Laser ranging systems
- Automated video detection & tracking systems
- Industrial automation
- Port security
- Vehicle & shipboard surveillance systems



1485 Rollins Road, Burlingame, California 94010
(650) 342-9399 • FAX: (650) 342-9199
Sales@DPerception.com
www.DPerception.com

12/2006

PRECISION PAN-TILT UNIT

High-speed positioning of heavy payloads

Model PTU-D300

Technical Specifications

General Features

- Rigid design
- Solid and vibration-tolerant
- 360° continuous-pan with pass-through for any payload
- Single connector for all video, control, power
- Flexible payload mounting (top or side)
- Precise control of position, speed & acceleration
- CE Mark certified; Mil-spec optional
- Single DC power input

Pan-Tilt Performance

Standard	Side Mount	Top Mount
Max payload ^a	70 lbs. (31.7 kg.)	35 lbs. (15.8 kg.)
Max. speed ^b	50°/second	50°/second

a. Over-the-top payload assumes COG 6" from tilt-axis; over-the-side payload assumes balanced COG.
b. Max. speed may depend on exact payload configuration and dynamics

High-Speed Pan	Side Mount	Top Mount
Max payload	50 lbs. (22.7 kg.)	25 lbs. (11.3 kg.)
Max. pan speed	100°/second	100°/second
Max. tilt speed	50°/second	50°/second

Tilt Range (approx): -30° to +90° from upright (120° range)
Pan Range (approx): 360° continuous

Pan Speed Min: .0064°/sec
Tilt Speed Min: .0064°/sec
Pan Position Resolution: 0.0064° (with microstepping)
Tilt Position Resolution: 0.0064° (with microstepping)
Duty Cycle: Up to 100% duty cycle, or 3-5 million cycles
Acceleration/Deceleration: Trapezoidal. On-the-fly speed and position changes

Power Requirements

Input Voltage: unregulated 9-30VDC (fastest performance & torque @ 30VDC)

Power Consumption (measured at 30VDC):
49.2W avg. peak 2.25A (high power mode)
34.2W avg. peak 1.60A (regular power mode)
18.2W avg. peak 0.78A (low power mode/default)
1.6W (holding power off mode)

Connections & Communications

Base Connector: PRIMARY AMP (MIL-C-26482). Includes:
PTU-Power (3c) - 9-30VDC + shield
PTU-Control (7c) - RS-232/RS-485
Payload Signals (9-15c)

SECONDARY reserved

Payload Signal Pass Through:

Power (2c): 50VDC max @ 3A max
Video (4c):
Other (3-8c) 50VDC max @ 1A max
Microwave: (DC-18GHz) (OPTIONAL)
Custom: various (OPTIONAL)

Computer Control: RS-232 standard (not on all wiring options);
Built-in multidrop RS-485 networking

Control Protocols: DP (ASCII, Binary)

Mechanical

Weight: 26 lb. (11.34 kg) (Standard bracket: 1.25 lb.)

Dimensions:

Pan-tilt only: 11.61" H x 5.53" W x 8.53" D
w/top mount bracket: 13.12" H
w/side mount bracket: 13.16" W

Payload Mounting: side-mount, top-mount, dual-side+top mount

PTU Mounting: Pedestal mount

Material: Machined aluminum

Packaging & Environmental

Standards: Designed to IP67

Operating Temperature: -30°C to 50°C

Non-operating Temperature: -30°C to 70°C

Humidity: 100% relative humidity, non-condensing

Ice (operating): sustain operation with 0.25" ice buildup

Dust/Sand (operating): sustain exposure to blowing dust/sand

Wind/Rain/Fog: IP67

Salt Spray: sustain operation in salt spray environments

Color/Finish: Black anodized

EMI: FCC Part 15, part B Class A

Options

- Microwave payload pass-through (rotary joint)
- Side mount or top-mount brackets, dual-side-top bracket
- Geo-Pointing Module
- Ethernet/IP Interface
- Stabilization Module
- Expanded Payload pass-through wiring

Specifications subject to change without notice.



1485 Rollins Road, Burlingame, California 94010
(650) 342-9399 • FAX: (650) 342-9199
Sales@DPerception.com
www.DPerception.com

12/2006

Figure 21. Antenna frame alt-azimuth positioner and specifications.

50 Ω traces for all signals. The PCBs use SMB connectors that allow easier interconnection of coaxial cables between PCBs. Several versions of the PCBs were built and tested as



Figure 22. Model of the antenna and RF electronics.

prototypes to determine impedance, cross talk and grounding.

As discussed above, the operation of the RF system consists of generating RF voltages for 72 channels that consist of phase controlled 2.2 GHz and 2.6 GHz signals, with all other spurious harmonics suppressed. The specifications for each channel are given in the Table 2.

Output power(max)	+10dBm
Power variation channel to channel	<1dB
Phase jitter	<2 degrees rms (5 ps rms)
Phase control	0-360 degrees
Spurious harmonics and signals	<-30dBc

Table 2. Specifications for each channel.

Precise control of the superluminal speed of the source equates to precise control of signal phase. The RF system uses a reference channel against which to set the phases of all 72 channels. There is a splitter in each of the 72 channels used to derive a signal to monitor both amplitude and phase via a digitally-controlled binary switch stack; as in the 8-element system, final signal digitization is provided by a high-speed oscilloscope. Further details of this section of the system are given below.

The system uses two tunable RF master oscillators built by L3 Nova Engineering; for most measurements one will be used at 2.2 GHz and the other at 2.6 GHz. These oscillator signals are divided into 72 channels and then amplified to provide the input RF signals to the 144 vector modulator chips (AD8349). The specifications for the Nova Engineering

oscillators are given in Table 3 and the critical parameters for the AD8349 are in Table 4.

Frequency tunable	2.0 to 3.0 GHz
SSB phase noise	-60dBc/Hz@1kHz removed
Spurious signals	-60dBc
Harmonics	-35dBc

Table 3. Specifications for the Nova oscillators.

1 degree rms quadrature error @ 1.9 GHz
0.2 dB I/Q amplitude balance @ 1.9 GHz
Broad frequency range: 0.8 GHz to 2.7 GHz
Sideband suppression: 46 dBc @ 0.8 GHz
Sideband suppression: 36 dBc @ 1.9 GHz
Modulation bandwidth: dc to 70 MHz
0 dBm output compression level @ 0.8 GHz
Noise floor: 147 dBm/Hz
Single 2.7 V to 5.5 V supply
Quiescent operating current: 45 mA

Table 4. Specifications for the AD8349.

The AD8349 allows precise amplitude and phase control of the output RF signal. The 2.2 GHz and the 2.6 GHz inputs are combined together and adjusted to provide a matched output. The AD8349 is rated to 2.7 GHz and extensive testing done at LANL showed it worked well up to this frequency. We use DC signals for phase control in the design. The AD8349 allows IF control signals but for our design DC controls were found to be simpler and more precise. We use the Linear Technology LTC1660 10-bit 8-channel D/A converter to control amplitude and phase inputs to the AD8349. Figure 23 shows the PCB Artist layout of the main PCB with the AD8349 and LTC1660. Figure 24 shows the block diagram for 8-channels. The 72 channels consist of 9 identical blocks of 8-channels.

As mentioned briefly above, the system has 72 monitor points located just before the signals are sent to the array of antenna elements. The 72 monitor channels are sent through a switch matrix that allows any one channel to be measured and compared to a reference channel. The LabView program allows any one channel monitor point to be selected and compared to the reference. This monitoring of the 72 channels will be performed while the system is operating. In this way, the phase of each channel can be adjusted in real time to keep the system running correctly in the face of, *e.g.*, thermal drifting of components. This monitoring system also allows trouble shooting of any channel in case of failures.

The system design allows easy maintenance and repair. Spare boards will be ready in case of failures. The monitoring system will allow the failed PCB to be determined. Spare PCBs can be exchanged quickly and the system put back into operation.

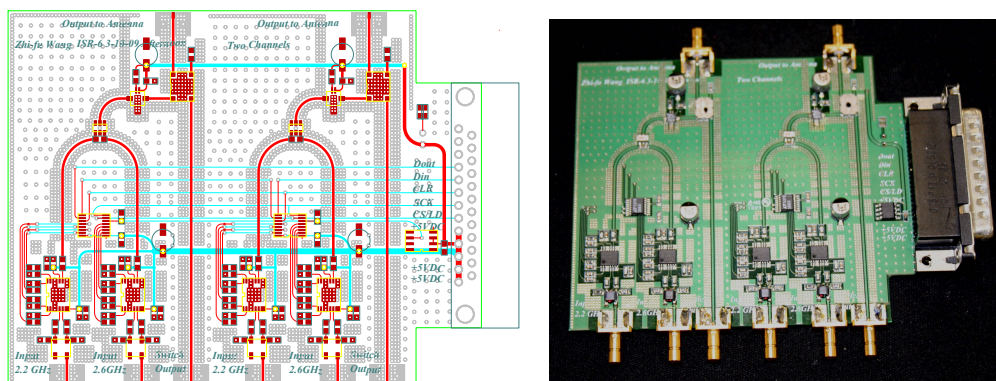


Figure 23. PCB Artist layout of 2-channel RF modulator (left), photo of the board (right).

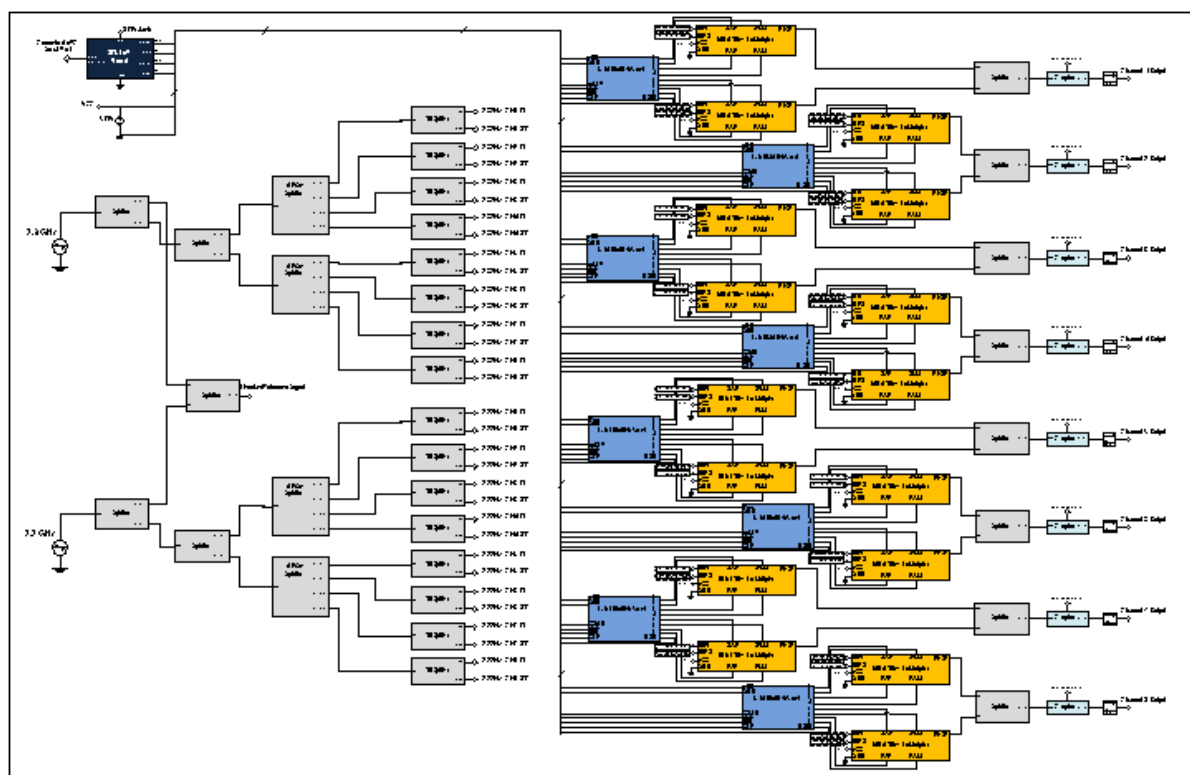


Figure 24. Block Diagram for the 8-channel board

The PCBs are tested using a LabView control and measuring system. The main measuring instruments are a Tektronix 4GHz 20GS/s digital scope and a HP8594E Spectrum Analyzer. The test setup is shown in Figure 25. The PCBs are also tested for RF loss and reflections using an HP8720 network analyzer.

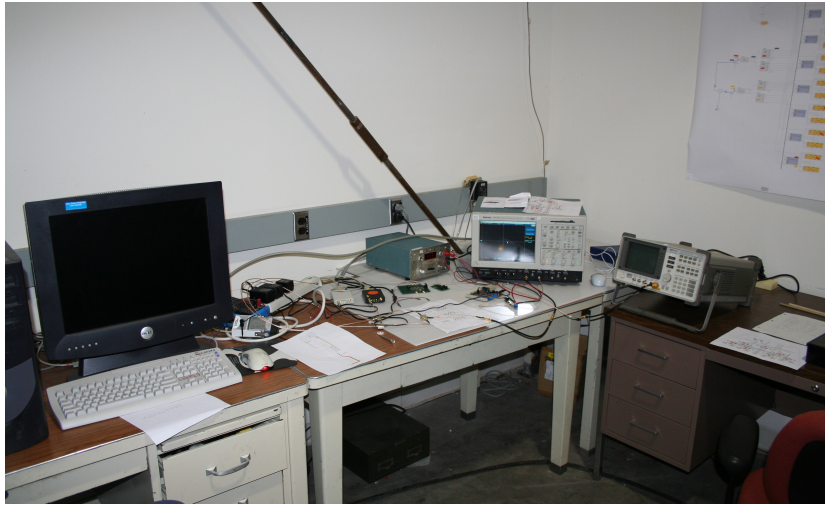


Figure 25. Test setup for PCBs

2.8. Anechoic chamber and test measurement systems

The eventual goal of the superluminal program is to make measurements of the various sources outside at distances ~ 1 km (see Section 2.11), where the cusp becomes much easier to detect [2]. However, it is prudent to perform the first tests at the location where the hardware is being designed and fabricated. To accomplish this, an anechoic chamber was built and equipped in Building 14 of TA 53 at LANL.

The anechoic chamber is a wooden $3.8 \times 3.8 \times 3.8$ m³ room, designed to approximate RF transmission in free space. Directly inside the wooden structure is aluminum sheet, which acts as a Faraday cage, shielding the experiment from outside RF interference. Inside the chamber, the aluminum sheet is completely covered with an absorbing material. The material used for this is ECCOSORB VHP-NRL, from Emerson & Cuming Microwave Products [21]. The absorbers used have a pyramidal shape with a 30 cm long cone, and use dielectric loss to absorb the RF [21]. This material has measured reflectivity that is less than -30 dB at 2 GHz [21]. Fig. 26 shows a picture of the inside of the anechoic chamber, where the absorber can be seen. Because no radiation can get in from the outside, and the absorber (ideally) absorbs all radiation from the transmitting antenna that does not hit the receiving antenna, any measurement made in the anechoic chamber is theoretically identical to a measurement made in infinite free space.

The stand used to hold the superluminal sources is shown on the left side of Fig. 26. This stand is a commercially purchased, Computer Controlled Pan-Tilt Unit, Model PTU-D300 from DirectedPerception (Fig. 21). In this model, the pan angle can be varied by 360°, while the tilt angle can be varied by 180°. The Model PTU-D300 also contains encoders which can read the current location of the device back to a computer.

Manipulating this stand is the primary method used to map out radiation patterns in the superluminal experiments. Varying the pan angle of the stand effectively controls the θ coordinate of the observer, in spherical coordinates. A negative pan angle means that the

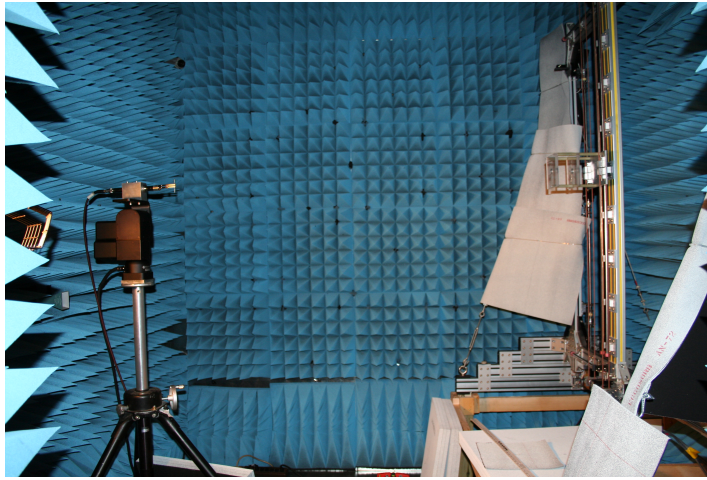


Figure 26. Photograph of the anechoic chamber, including the rotating stand and the x-y positioner. When data are being taken, the metal frames of the two stands are also covered in absorber.

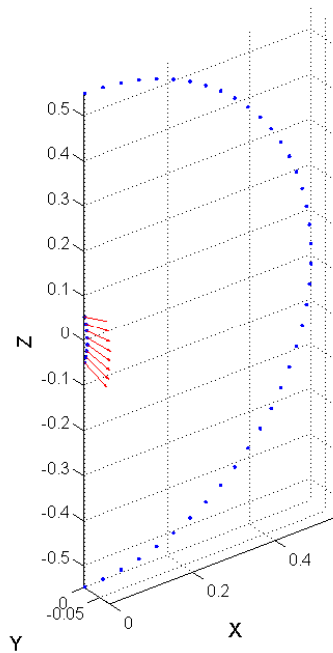


Figure 27. A schematic showing how varying the pan angle on the antenna stand effectively changes the observation angle. The pan = 0° point corresponds to the observation point at $z = 0$. The red arrows are pointing in the dipole direction for the Bluetooth dipole experiments, and the primary direction of dielectric polarization for the polarization antenna experiments.

ϕ angle of the observer, in spherical coordinates, is shifted by 180° . Fig. 27 is a schematic showing how varying the pan angle on the antenna stand effectively changes the θ coordinate of the observer. The ϕ angle of the observer can also be adjusted by altering the tilt angle on the antenna stand.

On the right side of Fig. 26 we see the stand used to hold and position the receiving antenna. This stand can be manipulated as an $x - y$ positioner, with 72 cm of motion in any direction from the center. The $x - y$ positioner can move in steps as small as 0.007 cm, and contains encoders which read the current position of the stand back to a computer.

The receiving antenna used for these experiments is a Schwarzbeck tunable $\frac{1}{2}$ -wave antenna. The distance between the receiving antenna and the superluminal source is 1.37 m when the receiving antenna is at the center. Since a typical wavelength in the experiments is $c/(2.4 \text{ GHz}) = 0.125 \text{ m}$, the experiment is adequately in the far field region, with $R/\lambda \approx 11$. Adjusting the $x - y$ positioner antenna can increase the distance between the receiving antenna and the superluminal source.

The $x - y$ positioner was also used to confirm that reflections from walls were minimal inside the anechoic chamber. For this test, a single Schwarzbeck dipole was placed on the rotating stand, in place of the superluminal source. The rotating stand was kept at a constant position, and both the transmitting and receiving antennas were pointed in the vertical (\hat{z}) direction. Then the $x - y$ positioning stand was used to map out the radiation pattern from the transmitting dipole, to make sure that reflections from the walls were not leading to an interference pattern inside the chamber. Variations in power due to the interference patterns observed inside the chamber were found to be less than 0.5 dB.

The amplitude of radiation is measured through an HP 8594E spectrum analyzer. The radiation from the superluminal source is peaked at two frequencies, $(\eta \pm \Omega)/(2\pi)$. Generally, an experimental scan is done twice so that the spectrum analyzer can measure the radiation from the two separate peaks using a reasonably narrow frequency window.

A LabVIEW code was written to manipulate the stands, take data, and keep track of all relevant experimental parameters (source speed, carrier and modulation frequencies *etc.*). The code is fully automated to vary a wide range of experimental parameters, including the rotation velocity of the source, the pan and tilt angle of the rotating stand, and the x and y position of the $x - y$ positioner stand. After adjusting the position of any antenna, the LabVIEW code always pauses (typically for 200 ms) to make sure there are no errors introduced from vibrations in the stands.

Most experiments thus far have employed the 8-element prototype machine. The measurements involve varying the speed of the superluminal source, and for each speed performing a fine scan of the pan angle of the rotating stand, from -90° to $+90^\circ$ in 0.5° steps. After every individual scan, the LabVIEW code saves the data as a LabVIEW data file, an Excel spreadsheet, and a Matlab file. This is very convenient for the plotting and analysis of large amounts of data. For example, Figs. 29, 30, 31 and 32 involve 23300 points of data, but it only took a few seconds to create each of these with a Matlab code that was written at LANL specifically for the purpose.

2.9. Test results of 8-element machine: Bluetooth dipoles and dielectric wedges

2.9.1. Test of speed control using an array of Bluetooth dipoles.

As an initial test of the precise superluminal speed control of the 8-element prototype electronics, the 8 dielectric



Figure 28. A photograph of the 8 Bluetooth dipoles used for initial tests inside the anechoic chamber. The dipoles are mounted in the same configuration as the dielectric elements.

elements were replaced with 8 Bluetooth dipoles. The production of a cusp demands a continuous, *volume* superluminal source [2, 4, 12]. Hence, unlike the dielectric antenna elements, the discrete dipoles will not emit a radiation cusp. Nevertheless, the emitted radiation from the dipoles approximates a vacuum Čerenkov cone [11]; the angle at which this emerges is an excellent means of measuring the effective speed of the source.

Experiments were performed inside the anechoic chamber. Fig. 28 shows the 8 Bluetooth dipoles mounted on the rotating stand in the anechoic chamber. The Bluetooth dipoles are commercial products that are designed to radiate at frequencies between 2.4 GHz and 2.48 GHz; however, measurements of their S_{11} parameters showed that they continued to radiate a significant portion of the input power out to 2.6 GHz. Because of this, the carrier frequency for these experiments was set to $\eta/2\pi = 2.5$ GHz, and the modulation frequency was set to $\Omega/2\pi = 100$ MHz.

The modulated signal used in these experiments emits radiation primarily at the two sidebands described in Eqn. 7. These two sidebands will have their emission peaked at the modified Čerenkov angles [1, 2, 11]

$$\sin \theta_{\pm} = \left(\frac{\eta}{\eta \pm \Omega} \right) \frac{c}{v}, \quad (8)$$

When the two sideband frequencies are 2.4 and 2.6 GHz, the two Čerenkov peaks are at

$$\sin \theta_{+} = \frac{2.5}{2.6} \frac{c}{v} \quad \text{and} \quad \sin \theta_{-} = \frac{2.5}{2.4} \frac{c}{v}. \quad (9)$$

As an initial test, the antenna speed was varied from $-6c$ to $+6c$, in steps of $0.4c$. Here a negative velocity implies that the phase differences between antenna elements are reversed; the Čerenkov cone will then emerge at a negative angle [2]. Both positive and negative velocities were used to eliminate possible asymmetries in the angular measurements.

Figs. 29 and 30 show waterfall plots of the measured power versus pan angle of the rotating stand, for all of the positive rotation speeds of the superluminal source. The data

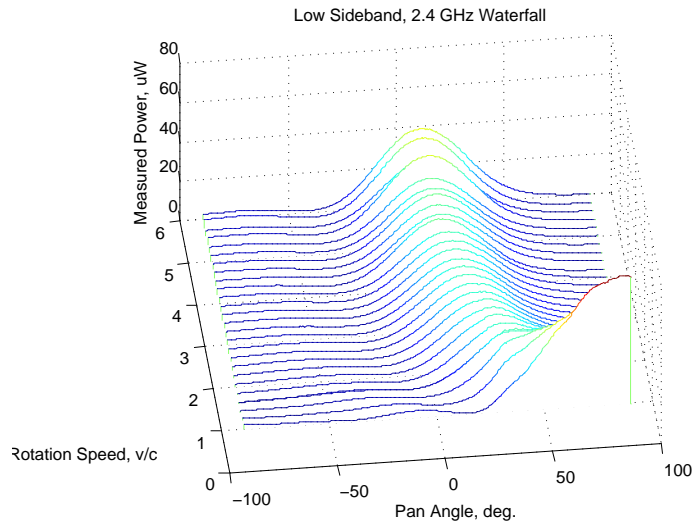


Figure 29. A waterfall plot showing measured power from scans of the pan angle of the rotating stand, at a succession of different speeds of the superluminal source. The data shown here are from the lower sideband (2.4 GHz).

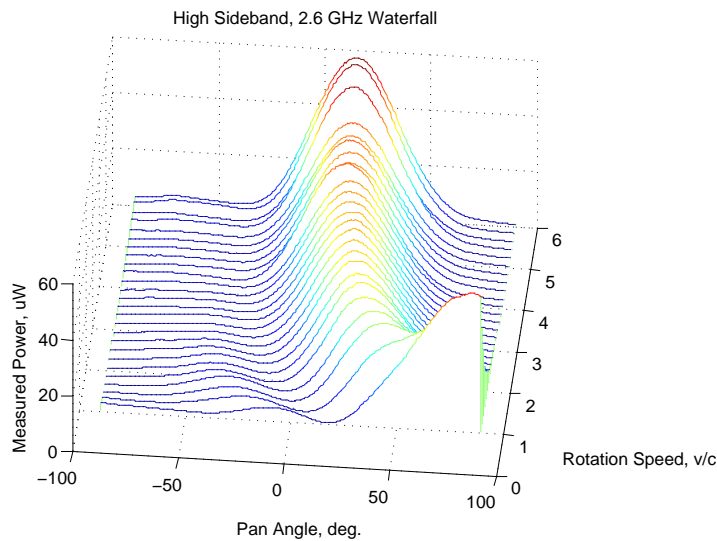


Figure 30. A waterfall plot showing measured power from scans of the pan angle of the rotating stand, at a succession of different speeds of the superluminal source. The data shown here are from the higher sideband (2.6 GHz).

in these figures are smooth, both when the pan angle and the rotation velocity is varied. This suggests that interference from external sources is not playing an important role in the measurements. Some interference-like behavior is seen in both the high and low sidebands at very high velocities. The highest powers, particularly in the lower sideband, are seen at low rotation velocities. At velocities close to c , the peak angle of radiation jumps, as expected, to $\approx 90^\circ$, for both the higher and lower-frequency sidebands [2].

To understand how well the 8-element machine works, it is important to compare the angle of peak power found in the measurements of Figs. 29 and 30 with the theoretical peak

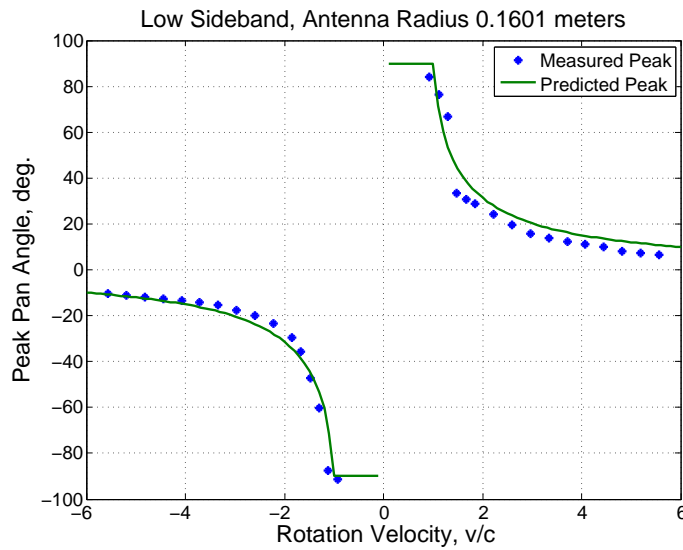


Figure 31. The measured peak pan angles of the radiation from the Bluetooth dipoles versus the rotation speed of the superluminal pattern. These data are for the lower sideband, at 2.4 GHz.

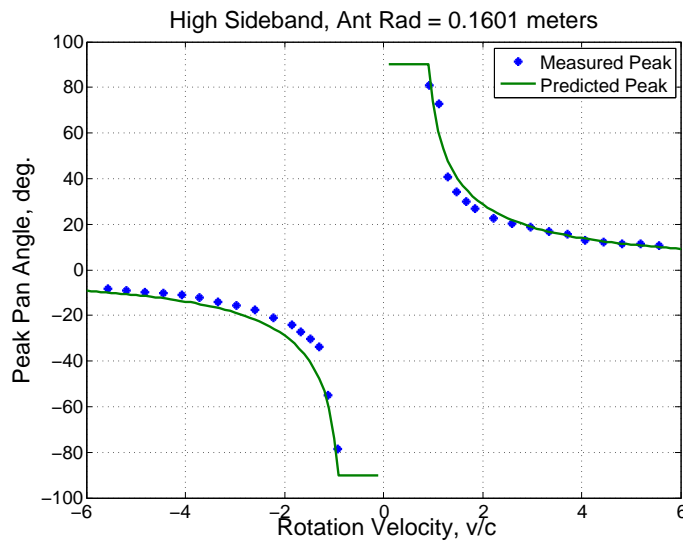


Figure 32. The measured peak pan angles of the radiation from the Bluetooth dipoles vs. the rotation speed of the superluminal pattern. These data are for the higher sideband, at 2.6 GHz.

angle of Eqn. 9.

Figs. 31 and 32 show a comparison of the measured peak angles with the predicted peak angles for the Cerenkov cone according to Eqn. 9. In general the match between theory and experiment is very good, showing that the phase setting electronics, the LabVIEW control software, and the anechoic chamber are all in working order. The small amount of discrepancy between theory and experiment is attributable to random errors in the spacing between the Bluetooth dipoles [2], and to some interference from reflections still present inside the anechoic chamber.



Figure 33. A photograph of the experimental setup when the receiving antenna is outside the anechoic chamber. Additional absorber, not shown in the photograph, was present on the bottom 1/3 of the door to the anechoic chamber. The door frame (covered in absorber) and the extra absorber in the lower part of the door help to eliminate ground and wall interference paths.

2.9.2. Tests using the 8-element dielectric antenna. The first 8 element dielectric antenna has been assembled from wedges identical to those to be used in Technology Demonstrator 1. It is currently being tested in the laboratory. Fig. 34 shows the dielectric antenna mounted on the rotating stand. For the initial tests of the 8 element wedges, the receiving antenna was moved outside of the anechoic chamber. This was done because it was suspected that the small discrepancy between measurement and theory in Figs. 31 and 32 may be due to near-field effects. When the receiving antenna is moved outside the chamber, the distance between it and the superluminal source is 8.6 m. Then $R/\lambda = 69$, and the measurements are completely in the far field.

The initial tests are promising, showing that the dielectric antenna wedges work as intended. A scan, showing the measured power at 2.4 GHz versus pan angle, using the dielectric antennas and the Bluetooth antennas is shown in Fig. 35; the source speed was the same in both cases. The measurements shown in Fig. 35 indicate that the 8 wedges, when put together, give off slightly more power than the 8 Bluetooth dipoles. As discussed in section 2.5, tests of isolated individual antenna elements do not give a good impression of the true performance; the wedges were designed to be used in an array. Therefore, the fact that the radiated power from the dielectric wedges is slightly greater than the radiated power from the Bluetooth dipoles, which have S_{11} parameters that are less than -10 dB at the measured frequencies, indicates that the prediction of the simulations is correct and that the wedges have good S_{11} parameters when used together.

Fig. 35 also shows that the dependence of measured power on pan angle is similar for the Bluetooth dipoles and the dielectric antenna. If the dielectric antenna had poor S_{11} parameters, then a large part of the incoming signal would be reflected back into the phase control electronics. This would distort the output signals in unpredictable ways, and likely

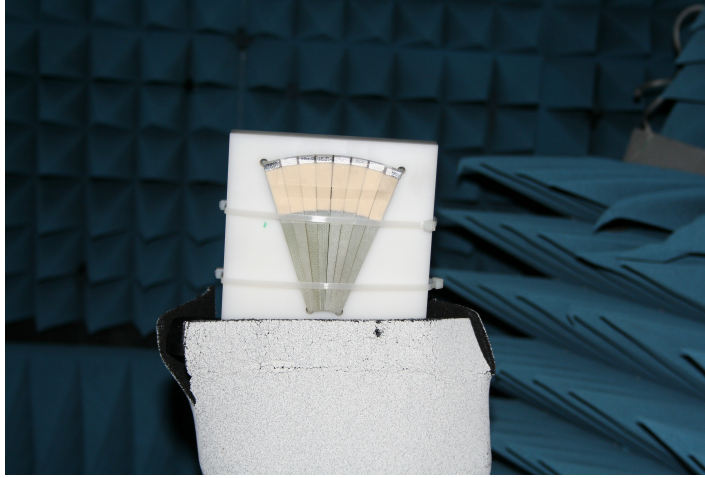


Figure 34. A photograph of the 8-element dielectric antenna inside the anechoic chamber.

would cause the phase control system to stop functioning properly. Because the observed power dependence is similar with both radiating sources, and the measured peak is reasonably close to theory, the phase control electronics must be working properly, providing further evidence that the dielectric wedges are radiating as predicted. Thus far, the dielectric antenna has shown good performance for source speeds between c and $6c$.

A small secondary peak is observable in the negative pan angle region of Fig. 35, when the Bluetooth antenna are used, but is not observable when the dielectric antenna are used. This is in agreement with predictions; EM simulations of 8 discrete dipoles give this secondary peak, while simulations of 8 dielectric wedges show that the peak is suppressed. This is a very good indication that the dielectric elements function as volume radiation sources, as desired.

2.10. Design of Technology Demonstrator 2: a superluminal linear accelerator

2.10.1. Design of dielectric antenna elements for the linear accelerator. Technology Demonstrator 2 is planned as a linear array of dielectric antenna elements. Design studies showed that a linear antenna element can be achieved by simply replacing the 5-degree wedge of the circular machines by a strip of a width equal to the widest section of the propagation region. Fig. 36 shows the geometry that consists of the same subelements as the previous design, except for a strip and compatible alumina slab. The S_{11} -characteristics (Fig. 37) shows very similar characteristics to the earlier wedge design (*c.f.* Fig. 14).

2.10.2. Control electronics for the linear accelerator. The electronics for the linear machine will be built by adapting the 8 element box, shown in Fig. 18, to include 24 elements. The 16 additional elements will be built from the printed circuits described in Section 2.7. For a rectilinearly accelerating source that is also oscillating in time, the voltage on each rectangular electrode will be described by

$$V_j = V_0 \cos[\eta(j\Delta t_j - t)] \cos \Omega t, \quad (10)$$

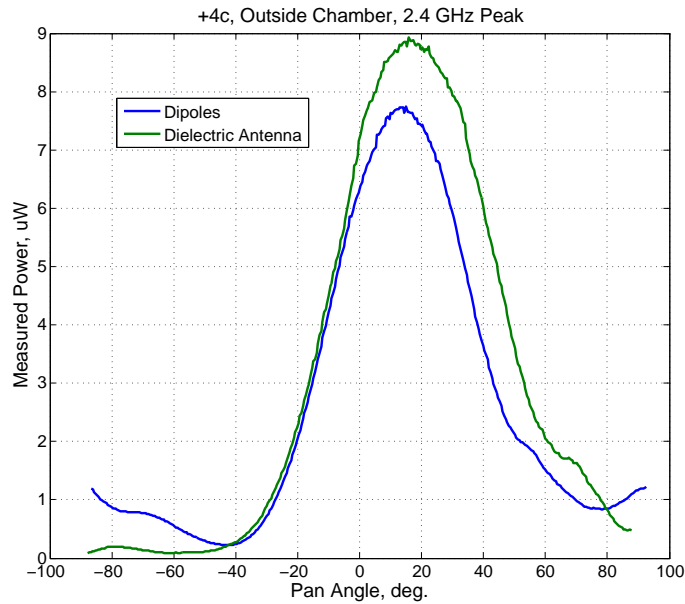


Figure 35. A scan of measured power at 2.4 GHz versus pan angle, using the dielectric antennas and the Bluetooth antennas. For these scans, the receiving antenna was outside the chamber.

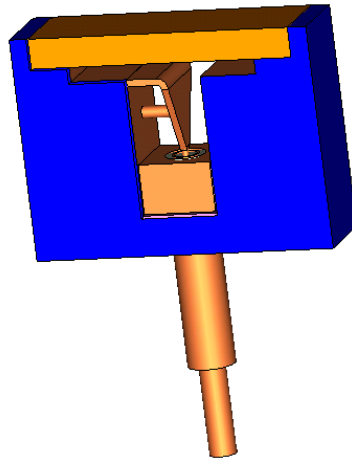


Figure 36. Geometry of the strip antenna element: the antenna elements for the linear array can be obtained by simply replacing the wedge and alumina slab of the circular machines by strip-shaped elements. All other features can be identically used from the earlier design.

where the Δt_j are calculated to give the required acceleration, which need not be uniform.

The relation between the time delays Δt_j and the phases between adjacent elements is the same as in the rotating case. For velocities that range from slightly under c to $6c$, the phase differences between adjacent elements must vary from $\approx 40^\circ$ to 5° . Tests using the 8-element machine have already proven that the electronics can set all of these phases accurately. For the linear accelerator, the LabVIEW code will have to be modified to be able to set different phases between each antenna.

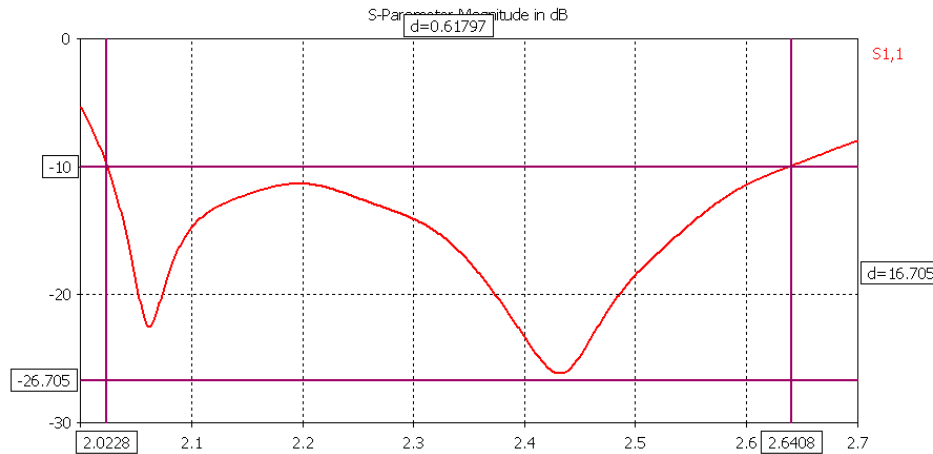


Figure 37. S-parameter results for the linear antenna simulation; the bandwidth required to transmit carrier and modulation frequency is maintained in this simple redesign for the strip element based on the previous wedge design for the circular machines.

2.11. Future experimental work

2.11.1. Use of Technology Demonstrator 1: the 72- element circular machine. Technology Demonstrator 1 is currently under assembly. As this report is being written, about 20 of the circuit boards are assembled, and over one quarter of the dielectric antenna elements (wedges) are finished. Assembly and initial characterization of this machine is planned over Summer 2009, using the anechoic chamber to verify source speed control and polarization of the emitted radiation. In addition, a phase-front analysis apparatus employing two Schwarzbeck dipole aeriels will be commissioned and used to characterize the emitted radiation [8]. The latter measurements are important in verifying the relationship between reception time and the multiple retarded times. They also will underpin the patented application of superluminal sources as the basis of countermeasure-resistant radar [8].

On completion of these short range tests, the machine will be moved outside so that the evolution of the emitted radiation with increasing distance can be studied; the intention of this study is to detect and characterize the cusp radiation, relevant both to long-range, low-power communication applications [2] and to astrophysics (this phase of the program could be said to represent a ground-based astrophysics measurement) [14]. A suitable site at the lower end of Mortendad Canyon has been identified for these trials; grass is known to act as a very good absorber for ~ 2.5 GHz radiation, suppressing the ground-reflected interference path [2] and simplifying the analysis of the data.

2.11.2. Experiments using Technology Demonstrator 2: the linear accelerator. After assembly and characterization in the anechoic chamber (late 2009), the key measurement for the linear accelerator is the measurement of the ring-like region of intense temporal focusing (Fig. 2(c)), the position of which is a precise function of the acceleration and speed of the source. This is an electromagnetic analogue of the “sonic boom” produced by a jet plane as it

High Power Wedges

RF Block Diagram

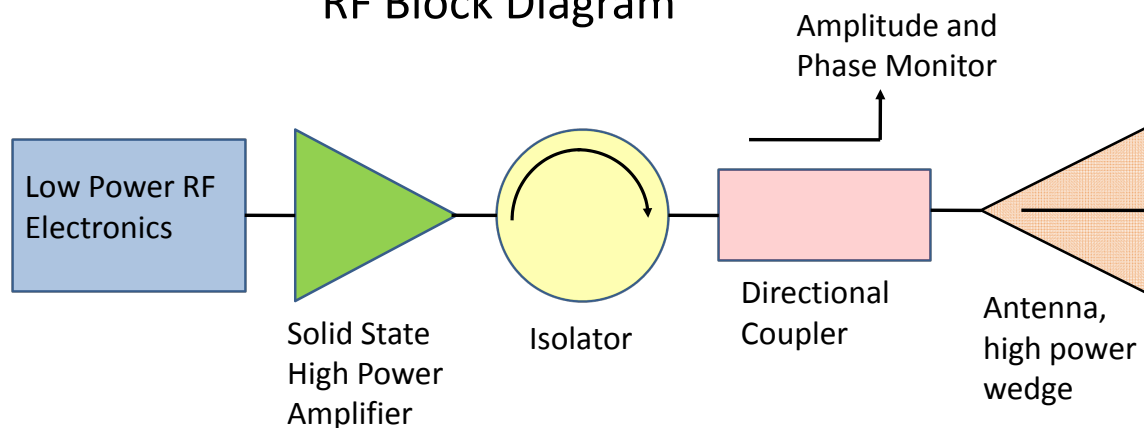


Figure 38. Block diagram of high power wedge RF system.

accelerates through the speed of sound [13, 22, 23, 24].

To demonstrate the “electromagnetic boom”, a rail system is currently being set up next to the anechoic chamber so that a detector (a Schwarzbeck calibrated dipole) can be moved reproducibly to distances of up to 10 m away from the source. The experiments would involve setting the acceleration and speed of the source, and then performing an angular mapping at various closely-spaced distances to precisely locate the position of the “boom”. In addition to being an interesting piece of fundamental science, this demonstration would serve as a proof of concept for directed-energy applications of superluminal sources. The experiments are also relevant to a potential model for gamma-ray bursts which we are developing [25].

2.11.3. Technology demonstrator 3: high-power dielectric antenna elements. The goal for high power testing in year three will be a simple extension of the low power RF electronics version of year two. We will use the same RF PCBs as low level drivers and purchase COTS RF high power amplifiers and insert them between the low level RF electronics and the antenna. We will also need to purchase isolators and directional couplers that will be located after the amplifiers and before the antenna for amplitude and phase monitoring and amplifier protection from reflections. Each channel will be identical.

Each RF channel will drive a single dielectric element (wedge) of the antenna. The high power wedges will be similar to the low power wedges of year two. There will be some mechanical changes to handle the coaxial cable input. We will use a high gain solid state amplifier with a power level up to 1 kW per channel. This will be a similar design to the Navy’s AEGIS Radar. The AEGIS is the premier Navy phased array radar for antimissile defense. The Navy uses a low level RF signal distribution system that feeds a 5 kW amplifier in each channel and then feeds the phased array antenna. The RF amplifier must be operated in the linear range to prevent phase distortion that would steer the radiated electromagnetic beam off target. Fig. 38 shows a diagram of the high power RF system.

3. Mathematical and Numerical Physics:

3.1. Introduction

Although Maxwell's Equations are necessarily relativistic, their solution for a source traveling faster than the speed of light is nontrivial. For example, unlike the case of a subluminal source, multiple retarded times must be considered [4, 5]. In addition, there are divergences in the fields to be handled [4, 5]. The modeling of the experimental superluminal sources and the astronomical observations (see Section 4) therefore demands a considerable amount of mathematical groundwork; sources that move faster than their own wavespeed have been little considered thus far, and the field is at a very early stage of development [11]. We are therefore both developing the mathematical framework necessary for treating superluminal sources on a regular basis and also building the numerical techniques required to solve some of the intractable equations encountered. Both lines of enquiry are necessary in understanding long-term applications of superluminal technology.

We will first describe the underlying physics that can be understood by treating a point-like superluminal source. This is relevant to the Technology Demonstrators and to a qualitative understanding of pulsar observations. Next, we will cover the fundamental Mathematical Physics techniques that are being developed, followed by the retarded time calculations that will underpin long-distance communications. Finally, our current focus is to derive the mathematical and numerical apparatus to tackle *extended* superluminal sources. The latter work is vital to obtain quantitative models for astrophysical phenomena and experimental machines.

3.2. Numerical visualizations of the Liénard-Wiechert fields of superluminal sources.

3.2.1. Superluminal charges in rectilinear motion. A remarkable aspect of a radiation source that exceeds its own wave speed is that the relation between retarded (source) and reception times need not be one-to-one [26]: multiple retarded times may contribute to a single instant of reception, which is to say that several wave fronts with differing emission times can pass through a single observation point simultaneously [4]. The relationship between emission and observation time for some simple superluminal sources can be visualized using the Huygens-Fresnel principle, which makes every point on a propagating wave front a source of spherical waves in its own right [15]. Fig. 39 shows a superluminal point-charge in constant rectilinear motion, as with the familiar Vavilov-Čerenkov effect [11]. Here, however, the source is traveling faster than the speed of light *in vacuo*, thus giving rise to so-called “vacuum Čerenkov radiation” [11]. The envelope of the emitted Huygens wavelets forms a cone whose aperture is given by $\cos(\theta) = c/v$ (Fig. 39 (top)), where c is the speed of light *in vacuo* and v that of the source: the higher the source speed, the narrower the cone. An observer outside the envelope cannot see the source since none of the advancing waves have reached him or her yet, whereas one inside it samples two distinct images from the source's history (Fig. 39 (bottom)). On the envelope of the wave fronts the two contributions coalesce and one sole image is received.

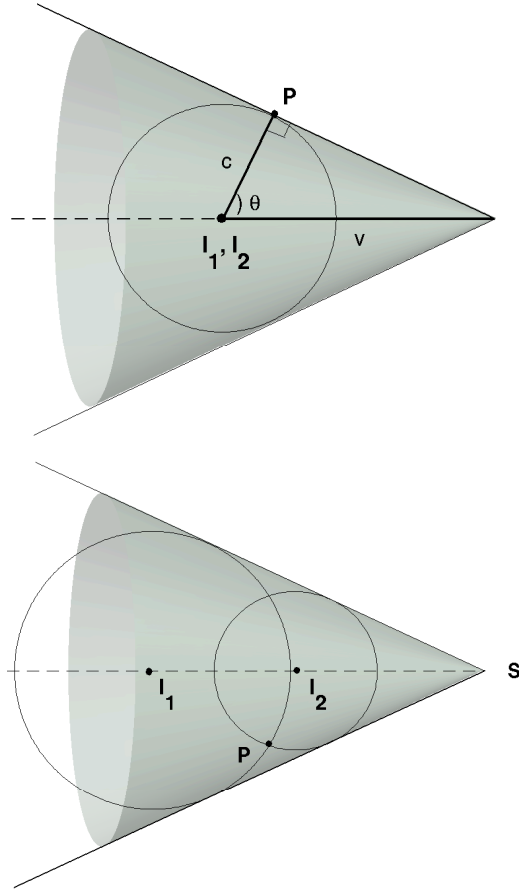


Figure 39. Huygens wavelets (light curves) and their envelope for a superluminal source moving at a constant velocity along a rectilinear trajectory. (top) On the envelope of the wave fronts, two contributions from the source's history coalesce and an observer will see one image of the source only. (bottom) An observer inside the Čerenkov envelope samples two images of the source, one to the left and one to the right. Nothing is seen outside the envelope.

If the superluminal source is also subject to linear acceleration, the wave fronts for which the superluminal “Mach number” $\beta \equiv (u + at)/c > 1$, *i.e.*, those that are emitted after the source breaks the “light barrier,” form a Čerenkov envelope consisting of two axisymmetric sheets and an elongated nose (Fig. 41). Here, u is the speed of the source at time $t = 0$ and a denotes the acceleration. As the source's acceleration increases, the inner and outer sheet of the envelope are pulled apart and the electromagnetic “Mach cone” becomes increasingly narrow. The space-time diagram in Fig. 40 shows that an observer may see images of the source from as many as three retarded times, depending on his relative position with respect to the envelope. Since the source is subject to acceleration, we observe the formation of a cusp, a region of intense concentration of emitted radiation, that is created at the singular point $(x_P, t_P) = (c^2/2a, c/a)$ and expands at the speed of light into a ring around the source's path. These shock waves of light constitute, in effect, an optical analogue of the “sonic boom” caused by an aircraft in supersonic flight [22, 23, 24].

The radiation emitted by a point charge q on an arbitrary trajectory $\mathbf{x}(t)$ as observed at

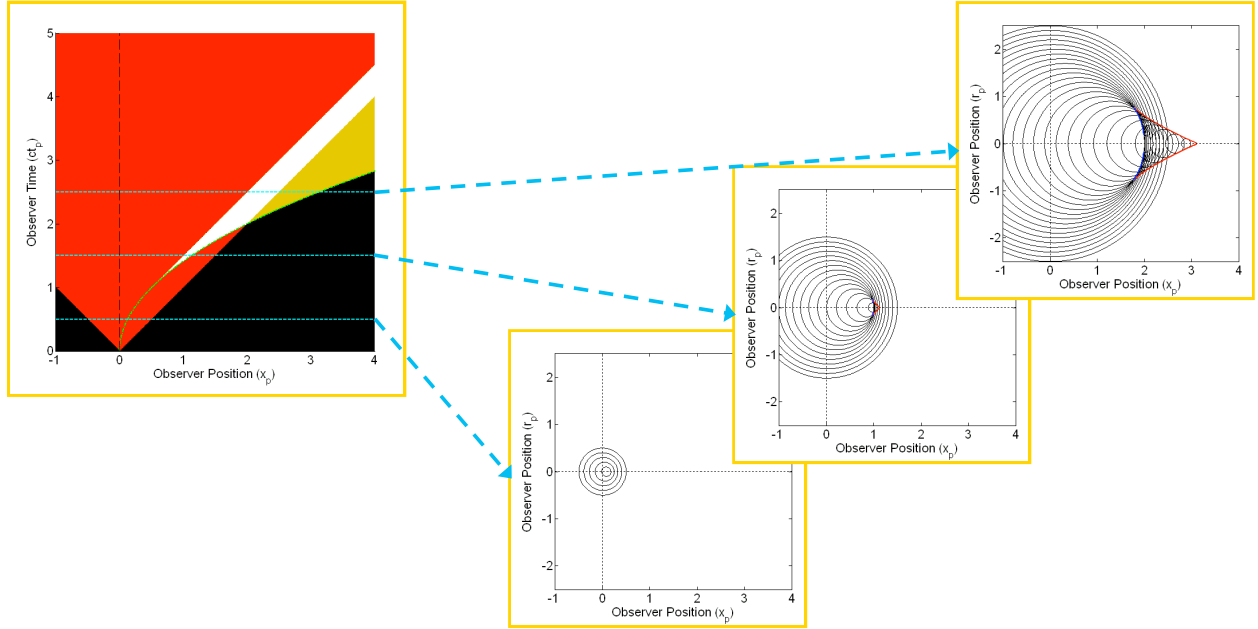


Figure 40. Space-time diagram and Huygens wavelets for a rectilinearly accelerated source. Depending on his relative position with respect to cusp and envelope, an observer will see one, two or three contributions from the source's history.

space-time coordinates (\mathbf{x}_p, t_p) is given by the familiar expression for the Liénard-Wiechert fields:

$$\mathbf{E}(\mathbf{x}_p, t_p) = q \sum_{\{t | t + \frac{R(t)}{c} = t_p\}} \frac{1}{|1 - \hat{\mathbf{n}} \cdot \boldsymbol{\beta}|^3} \left[\frac{(1 - \beta^2)\mathbf{u}}{R^2} + \frac{\hat{\mathbf{n}} \times (\mathbf{u} \times \dot{\boldsymbol{\beta}})}{cR} \right] \text{ and } \mathbf{B} = \hat{\mathbf{n}} \times \mathbf{E}. \quad (11)$$

Here, $\mathbf{R}(t) \equiv \mathbf{x}_p - \mathbf{x}$, $\hat{\mathbf{n}} \equiv \mathbf{R}/R$ designates the radiation direction, $\boldsymbol{\beta} \equiv \dot{\mathbf{x}}/c$ is the velocity vector of the source scaled by the speed of light, and $\mathbf{u} \equiv \hat{\mathbf{n}} - \boldsymbol{\beta}$. (The summation and the absolute-value brackets are typically omitted for the subluminal regime, in which retarded times are unique and $1 - \hat{\mathbf{n}} \cdot \boldsymbol{\beta}$ must be positive.) We note that the field diverges where $\hat{\mathbf{n}} \cdot \boldsymbol{\beta} = 1$; that is, where the source approaches the observer at the speed of light. Fig. 41(bottom) and Fig. 42(top) show the strength of the radiation field emitted by a source element traveling in the $z = 0$ plane along the trajectory $\mathbf{x}(t) = \tilde{x} + ut + \frac{1}{2}at^2$, where \tilde{x} is the position of the source at time $t = 0$. While the former is accelerating across the light barrier ($u = 0.5c$ and $a = c$ per second), the latter is slowing down uniformly ($u = 2.5c$ and $a = -c$ per second). Notice that, in this case, cusp creation occurs at $(x_p, t_p) = (-c^2/2a, -c/a)$, which lies outside the plane of observation. The point charge shown in Fig. 42(bottom) moves at a sinusoidally varying speed, *i.e.*, along the path $\mathbf{x}(t) = t + \alpha \sin(\eta t)$, weaving across the light barrier with amplitude α and frequency η .

3.2.2. Superluminal charges in uniform rotation. The analysis of faster-than-light sources that move along a rectilinear trajectory serves not only as an introductory case to more complex dynamical systems but has applications in its own right such as the development of novel directed energy and radar technologies. Of more relevance from an astrophysical point

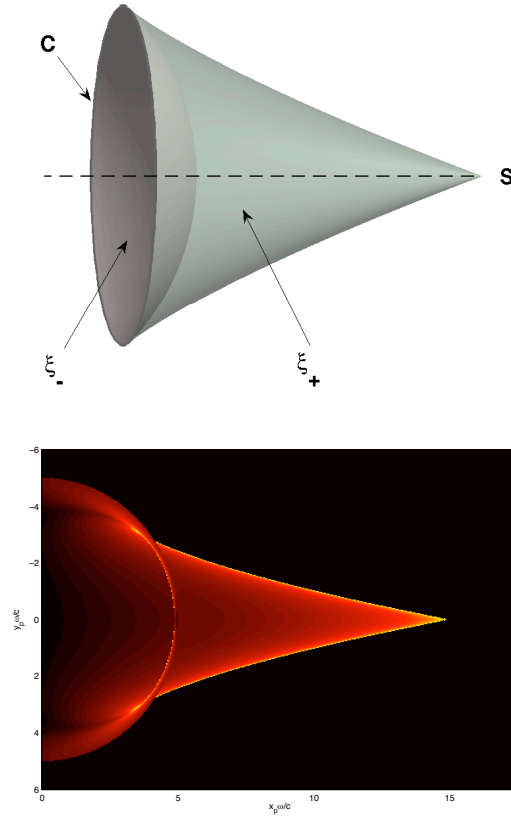


Figure 41. (top) Inner and outer envelope (ξ_- and ξ_+ , respectively) for a superluminal source moving with constant acceleration. The two sheets meet tangentially to form a cusp (C) around the source's path. (bottom) Calculated field strength for a similar source as observed in the $x_P - y_P$ plane. The two sheets of the envelope as well as the cusp are bright yellow, indicating regions of intense concentration of the emitted radiation.

of view, however, is the investigation of the electromagnetic fields that arise if a source of this type rotates about a fixed axis at a constant angular frequency [3, 14]. While our studies of radiation sources in constant superluminal rotation were originally motivated by astronomical observations of pulsars, they extend to rapidly spinning, highly magnetized stellar remnants in general and may aid in the explanation of phenomena as diverse as gamma-ray burst afterglows and the intense radiation received from quasars.

The radiation field of an extended source in uniform superluminal rotation as observed at a given point P is dominated by the emission from those of its volume elements that approach P , along the radiation direction, with the speed of light and zero acceleration at the retarded time. These elements comprise a filamentary part of the source, a threadlike structure whose radial and azimuthal widths become narrower the farther an observer is from the source, and whose length spans the distribution of the source parallel to the axis of rotation. Since the constituent elements of this filament are all situated at the same optical distance from the observer, their radiation field in the far zone is effectively identical to that of a point-like source and is here numerically approximated as such.

Consider an observer at cylindrical space-time coordinates $(r_P, \varphi_P, z_P; t_P)$ and a source element rotating in the $z = 0$ plane at radius r with angular velocity ω , *i.e.*, at retarded coordinates $(r, \omega t, 0; t)$. A retarded distance $R(t)$ from source to observer is

$$R(t) = c(t_P - t) = [z_P^2 + r_P^2 + r^2 - 2rr_P \cos(\omega t - \varphi_P)]^{1/2}, \quad (12)$$

and a retarded time t for observation time t_P is therefore a solution to [4, 12]

$$t_P = h(t) \equiv t + c^{-1}[z_P^2 + r_P^2 + r^2 - 2rr_P \cos(\omega t - \varphi_P)]^{1/2}. \quad (13)$$

Figure 43 shows the function $h(t)$ for three characteristic combinations of source speed and observer position. Solutions of $t_P = h(t)$ are intersections of horizontal lines t_P with the graph of h . Because of the oscillating term in Eqn.13, for case (a) there may be three retarded times for a single observation time. Higher source speeds increase the amplitude of the oscillations in h , resulting in higher odd numbers of retarded times. In fact, the “critical values” N_m at which the number of intersections increases can be expressed as

$$\frac{2m\pi}{N_m} + \frac{2}{N_m} \arccos\left(\frac{1}{N_m}\right) - 2 \sin(\arccos(\frac{1}{N_m})) = 0, \quad m = 0, 1, 2 \dots \quad (14)$$

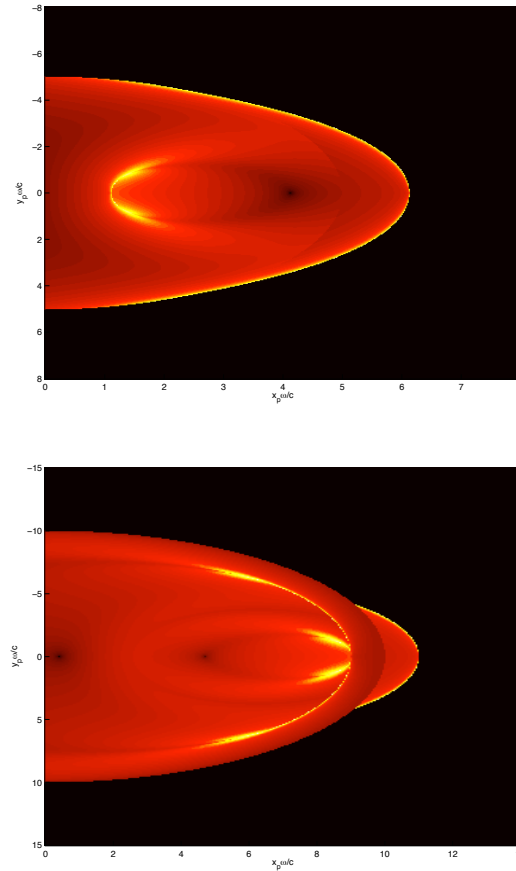


Figure 42. Strength of the radiation field emitted by charges subject to constant deceleration (top) and traveling at sinusoidally varying speed (bottom).

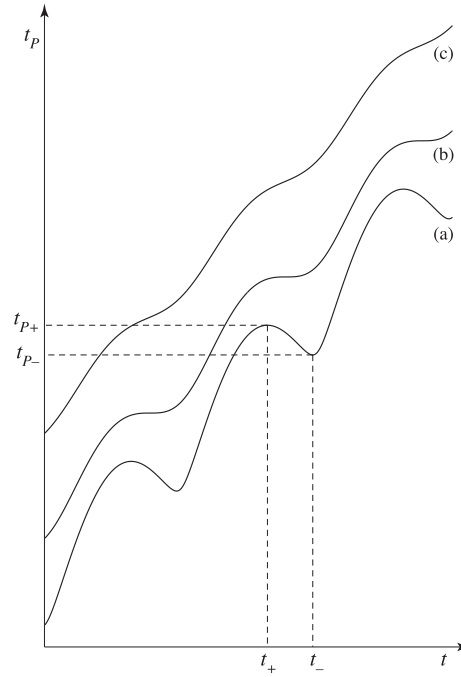


Figure 43. Relationship between observation and emission time for an observation point (a) inside, (b) on the cusp of, and (c) outside the envelope (after Ref. [4, 12]).

Here, N is the speed of the source divided by the speed of light *in vacuo* and, analogous to the Mach number, is dimensionless. Solving Eqn. 14 for N_m we find that $N_0 = 1, N_1 = 4.603 \dots, N_2 = 7.789 \dots, N_3 = 10.949 \dots$ and, in general, $\lim_{m \rightarrow \infty} N_m = m\pi$. Table 5 relates various source velocities to the number of retarded times which contribute to a single instance of observation time.

Velocity of the source (in multiples of c)	Number of retarded times
$0 \leq N \leq 1$	1
$1 < N \leq 4.603 \dots$	3
$4.603 \dots < N \leq 7.789 \dots$	5
$7.789 \dots < N \leq 10.949 \dots$	7

Table 5. Source velocities related to the number of retarded times which contribute to a single instance of observation time.

The Čerenkov-like envelope of an element of a superluminally rotating source is a tubelike structure consisting of two sheets (corresponding to t_{\pm} in Fig. 43) where the source element approaches the observer along the radiation direction at the speed of light ($\partial h / \partial t = 0$) and the field diverges (Fig. 44). The two sheets meet tangentially to form a cusp of points which the source element approaches not only with the wave speed, but with zero acceleration ($\partial^2 h / \partial t^2 = 0$, the inflection point of curve (b) of Fig. 43). The cusp curve is tangent to the light cylinder in the plane of rotation and spirals out above and below the plane, approaching

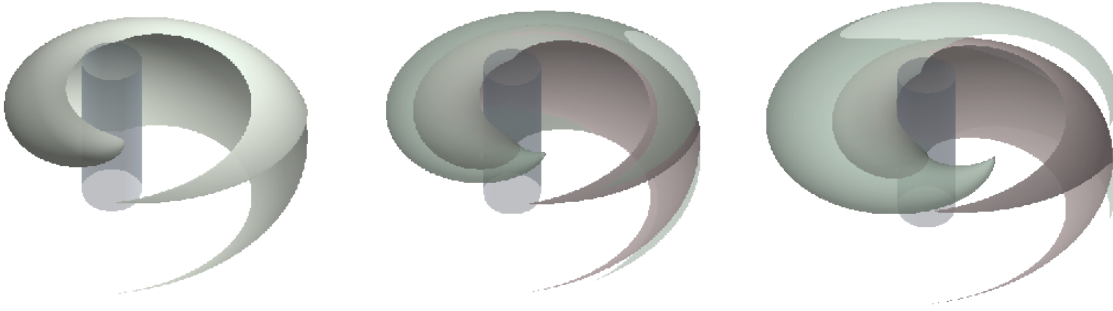


Figure 44. Development of the two-sheeted envelope for a volume element in constant superluminal rotation. (left) $\omega/c = 1$, (middle) $\omega/c = 1.75$ and (right) $\omega/c = 2.5$. Notice that the inner sheet of the envelope hardly changes while the outer sheet elongates and expands: a source that breaks the light barrier acquires a second, outer sheet.

the cone of polar angle $\arcsin(c/r\omega)$ [4, 12]. There is a remarkable effect associated with the cusp: an observer will receive essentially instantaneous contributions from an *extended period of source time*. This unique property, which we have demonstrated experimentally [2], constitutes *temporal focusing*, *i.e.*, focusing of radiation in the time domain, to produce a concentration of electromagnetic energy leading to an intensity that decays more slowly (as $1/R$) with distance R from the source than emission from a conventional radiation source (as $1/R^2$) [27]. This nonspherically decaying component of the radiation appears as a spiral-shaped packet of intense localized electromagnetic waves, a diffraction-free propagating caustic that, when detected by a far-field observer, presents itself as a powerful pulse of electromagnetic radiation [27]. The fact that cusp radiation decays more slowly than predicted by the inverse square law does not violate conservation of energy since weaker fields elsewhere in the emitted radiation compensate for the strong fields on the cusp, which is constantly reconstructed from conventional (*i.e.*, spherically decaying) waves that combine and disperse [27].

Numerical evaluations and visualizations of the radiation emitted by a localized source in superluminal rotation show the following intrinsic characteristics [3, 28]:

- (i) The radiation is sharply focused along a narrow, rigidly rotating spiral-shaped beam that embodies the cusp of the envelope of the emitted wave fronts (Fig. 45).
- (ii) For moderately superluminal sources, it consists of either one or three concurrent polarization modes (depending on the position of the observer relative to the cusp) that arise from contributions to the field from differing retarded times.
- (iii) At each edge of the pulse, two of the modes are comparable in strength, dominating over the third. Near the middle of the pulse, the three modes are of comparable strength (Fig. 46(left)).
- (iv) The position angle of one of the modes, as well as that of the total field, swings across the beam by as much as 180° , while the position angles of the other two modes remain approximately orthogonal throughout their excursion across the beam (Fig. 47 and Fig. 46(right)).

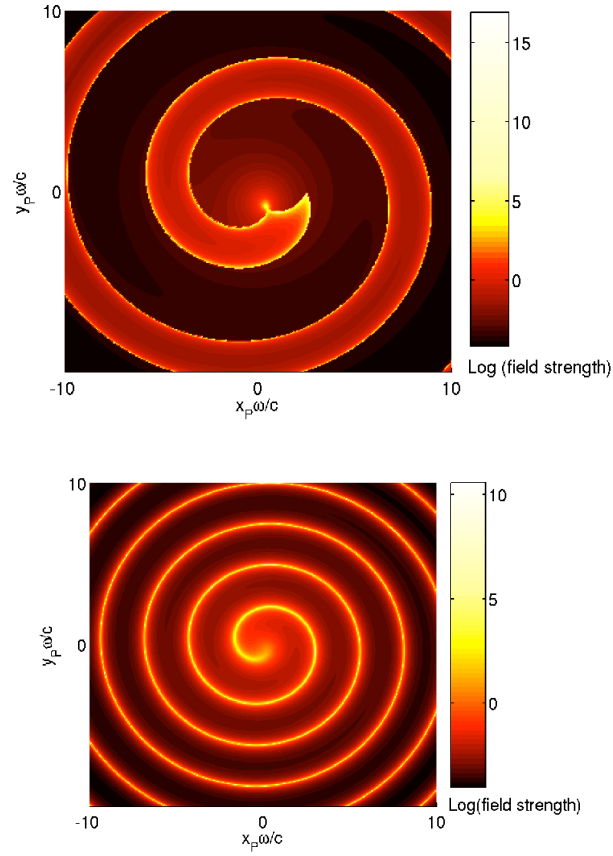


Figure 45. (top) Field strength in the plane of the source's orbit, for $\hat{r} = 2.5$. Note the high radiation intensity along the inner edges of the envelope and near the cusp. (bottom) Relative radiation intensity on the limiting cone of the cusp.

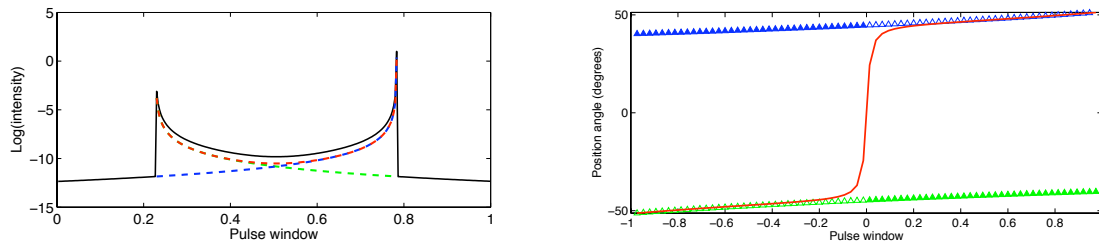


Figure 46. Intensity and polarization position angle for three retarded times (green, red, blue) and the total field (black)

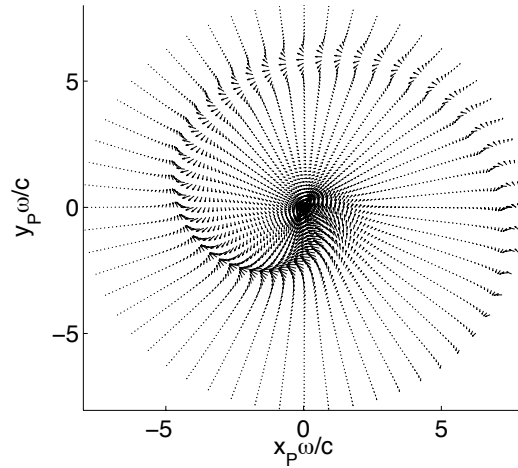


Figure 47. Polarization position angles and field strengths for a source with $\hat{r} = 2$ on the cone $\theta_p = \pi/12$ outside the envelope [3].

- (v) One of the three modes is highly circularly polarized and differs in its sense of polarization from the other two.
- (vi) Two of the modes are highly linearly polarized across the entire pulse.

As we have noted elsewhere [3, 14, 28], *all* of these characteristic phenomena are also observed in astronomical observations of pulsars, strongly suggesting that superluminal emission mechanisms are involved. We will return to this point in Section 4.

3.3. Mathematical Physics

3.3.1. The fundamental role of the retarded potential in the electrodynamics of superluminal sources. We have calculated the gradient of the radiation field generated by a polarization current with a superluminally rotating distribution pattern [26] and shown that the absolute value of this gradient increases as $R^{7/2}$ with distance R , within the sharply focused subbeams that constitute the overall radiation from such a source. In addition to supporting earlier findings that the azimuthal and polar widths of these subbeams become narrower (as R^{-3} and R^{-1} , respectively) with distance from the source, this result implies that the boundary contribution to the solution of the wave equation governing the radiation field does not always vanish in the limit where the boundary tends to infinity (as is commonly assumed in textbooks and the published literature) [26, 29, 30].

There is a fundamental difference between the classical expression for the retarded potential and the corresponding retarded solution of the wave equation that governs the electromagnetic field: while the boundary contribution to the retarded solution for the potential can always be rendered equal to zero by means of a gauge transformation that preserves the Lorenz condition, the boundary contribution to the retarded solution of the wave equation for the field may be neglected only if it diminishes with distance faster than the contribution of the source density in the far zone [26, 29, 30]. In the case of a rotating

superluminal source, however, the boundary term in the retarded solution for the field is by a factor of the order of $R^{1/2}$ larger than the source term of this solution, in the limit where the boundary tends to infinity [26]. This result is consistent with the prediction of the retarded potential that the radiation field generated by a rotating superluminal source decays as $R^{-1/2}$, instead of R^{-1} , and explains why an argument based on the solution of the wave equation governing the field in which the boundary term is neglected misses the nonspherical decay of the field. Given that the distribution of the radiation field of an accelerated superluminal source in the far zone is not known *a priori* to be prescribed as a boundary condition, our analysis establishes that the only way one can calculate the free-space radiation field of such sources is via the retarded solution for the potential [26, 29, 30].

These findings are not merely of mathematical interest, but are also relevant to pulsar observational data: the more distant a pulsar, the narrower and brighter its giant pulses should be [14, 28].

3.3.2. Rigid rotation of the polarization currents due to a rotating magnetic field. Very soon after the discovery of pulsars, it was realized that the very stable periodicity of the mean profiles of their pulses could only result from a source that rotates, and which therefore possesses a rigidly rotating radiation distribution [31]. In subsequent sections we will show that this source rotation is not only responsible for the periodicity of the pulses, but also determines the detailed frequency dependence of the emitted radiation [14]. However, before this could be accomplished, it was necessary to show that any electromagnetic disturbances must follow the rotation of the pulsar's magnetic field, irrespective of the speed that this implies.

The rigid rotation of the overall distribution pattern of the radiation from a pulsar is described by an electromagnetic field whose distribution depends on the azimuthal angle ϕ only in the combination $(\phi - \omega t)$, where ω is the angular frequency of rotation of the pulsar and t is the time. We were able to show that Maxwell's equations demand that the charge and current densities that give rise to this radiation field should have the same time dependence [14]. Therefore, the observed motion of the radiation pattern of pulsars can only arise from a source whose distribution pattern rotates rigidly, i.e. a source whose average density depends on ϕ only in the combination $(\phi - \omega t)$.

Furthermore, if a plasma distribution has a rigidly rotating pattern in the emission region, then it must have a rigidly rotating pattern everywhere; we were also able to show that a solution of Maxwell's equations with the time dependence $\partial/\partial t = -\omega\partial/\partial\phi$ applies either to the entire volume of the magnetospheric plasma distribution or to a region whose boundary is an expanding wavefront that will eventually encompass the entire magnetosphere of the pulsar [14, 28]. Unless the plasma atmosphere surrounding the pulsar is restricted to an unrealistically small volume, it is therefore an inevitable consequence of the observational data that the macroscopic distribution of electric current in the magnetosphere has a rigidly rotating distribution whose linear speed exceeds that speed of light c for radii $r > c/\omega$. This is a fundamental justification for the application of superluminal emission models to pulsar observational data [14, 28].

3.3.3. Spectral properties of the nonspherically decaying radiation generated by a rotating superluminal source. We have found that the focusing of the radiation generated by a polarization current with a superluminally rotating distribution pattern is of a higher order in the plane of rotation than in other directions [32]. Consequently, our previously published asymptotic approximation to the value of this field outside the equatorial plane breaks down as the line of sight approaches a direction normal to the rotation axis, *i.e.*, is nonuniform with respect to the polar angle. To investigate this issue, we employed an alternative asymptotic expansion to show that, though having a rate of decay with frequency (μ) that is by a factor of order $\mu^{2/3}$ slower, the equatorial radiation field has the same dependence on distance as the nonspherically decaying component of the generated field in other directions: it, too, diminishes as the inverse square root of the distance from its source [32].

As in the previous section, these results are relevant to the giant pulses received from pulsars [14, 28]: the focused, nonspherically decaying pulses that arise from a superluminal polarization current in a highly magnetized plasma have a power-law spectrum (*i.e.*, a flux density $S \propto \mu^\alpha$) whose index (α) is given by one of the values $-2/3$, -2 , $-8/3$, or -4 .

3.4. Retarded-time solutions

3.4.1. Statement of the problem. The various models of rotating superluminal sources we construct rely crucially on accurate determination of the possibly multiple retarded times contributing to an instantaneous observation time. There are numerical difficulties to overcome, especially in the physically most significant configurations: near the cusp of the bifurcation surface [4, 13].

The geometry of the problem is simple. A volume element of a rigidly rotating source distribution rotates in the X-Y plane at radius r with angular velocity ω . A retarded distance to an observer at spherical coordinates $(R_P, \varphi_P, \theta_P)$ is

$$R(t) = \left[R_P^2 + r^2 - 2rr_P \cos(\hat{\varphi} + \omega t - \varphi_P) \right]^{1/2}, \quad (15)$$

where $\hat{\varphi}$ is an initial angular position and $r_P \equiv R \sin \theta_P$. A retarded time t for observation time t_P must satisfy

$$t_P - t = R(t)/c \quad (16)$$

Introducing the length scale c/ω (where a circumflex over a length variable denotes such a scaled length) and the Lagrangian variables $\hat{\varphi} \equiv \varphi - \omega t$ and $\hat{\varphi}_P \equiv \varphi_P - \omega t_P$ (capturing the rigid rotation of the patterns of the source and the radiation field [14]), Eqn. 16 becomes

$$\phi = g(\varphi) \equiv \varphi + \left[\hat{R}_P^2 + \hat{r}^2 - 2\hat{r}\hat{r}_P \cos(\varphi - \varphi_P) \right]^{1/2}, \quad (17)$$

where $\phi \equiv \hat{\varphi} - \hat{\varphi}_P$. A numerical difficulty with Eqn. 17 is that a large (*e.g.*, astronomical) \hat{R}_P swamps the oscillations in the cosine term. We remedy this by subtracting $\hat{R}_0 \equiv (\hat{R}_P^2 + \hat{r}^2)^{1/2}$ from both sides, resulting in

$$\Delta\phi = \Delta g(\varphi) \equiv \varphi + \hat{R}(\varphi) - \hat{R}_0 = \varphi - \frac{2\hat{r}\hat{r}_P \sin \varphi}{(\hat{R}_0^2 - 2\hat{r}\hat{r}_P \sin \varphi)^{1/2} + \hat{R}_0}, \quad (18)$$

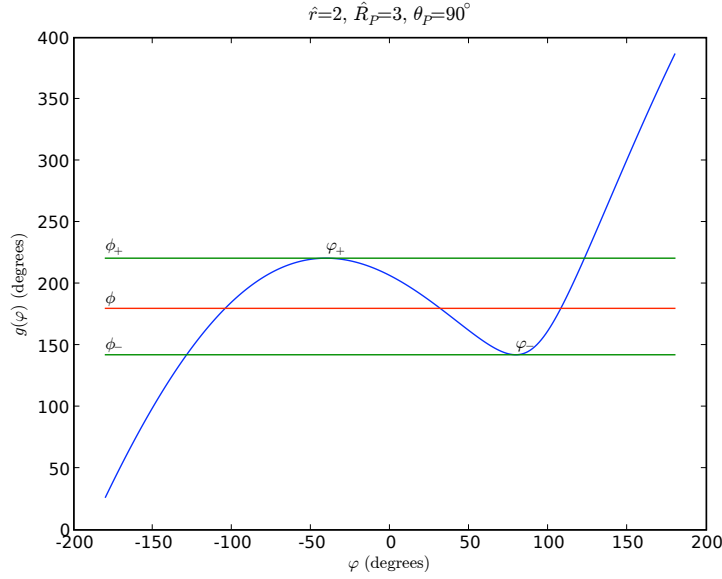


Figure 48. The function g , relating retarded and observation angular positions φ and ϕ , respectively. The local extrema are (φ_+, ϕ_+) and (φ_-, ϕ_-) . The retarded angles for an observation angle ϕ between ϕ_- and ϕ_+ are the intersections of a horizontal line with the graph of g .

where we have also chosen $\varphi_P = -3\pi/2$ for convenience. In the limit that $\hat{R}_P \rightarrow \infty$, this becomes

$$\Delta\phi = \varphi - \hat{r} \sin \theta_P \sin \varphi, \quad (19)$$

which is of the form of Kepler's equation for elliptical orbits [33],

$$M = E - e \sin E, \quad (20)$$

but the “eccentricity” is greater than one when multiple solutions for retarded times are possible. This correspondence with Kepler's equation brings to the fore the more serious numerical difficulty in solving either of the transcendental equations Eqn. 18 or 19: that e near one and M near zero results in severe subtractive cancellation [33]. In orbital mechanics, this special case of determining the eccentric anomaly near the pericenter of a near-parabolic orbit is usually merely a side issue, but for our superluminal sources, the analogous situation is a central concern: determining retarded times near the cusp of the bifurcation surface, which are the strongest contributors to the observed field. For typical pulsar observations, $\hat{r} \sin \theta_P$ is very near indeed to unity. Near the cusp, the increment above one is of the order of \hat{R}_P^{-2} , with the scaled distances \hat{R}_P to pulsars being of order 10^9 to 10^{15} . The oscillatory region of g is correspondingly tiny: in radians, $\varphi_- - \varphi_+$ is of order \hat{R}_P^{-1} , and $\phi_+ - \phi_-$, \hat{R}_P^{-3} .

Our solution to finding retarded times in this critical region is to precisely locate the turning points (φ_+, ϕ_+) and (φ_-, ϕ_-) of g using multiple-precision arithmetic and approximate Δg in this region by a cubic interpolating the turning points and matching the zero derivatives at those points. We find that this cubic is typically a good approximation to Δg over a range several orders of magnitude larger than $\varphi_- - \varphi_+$, and it can be directly inverted to yield

three real roots for $\phi_- < \phi < \phi_+$ or one elsewhere. Beyond this range, Δg is well enough behaved that, starting from linear first approximation to the root, a Newton or secant-method iteration will converge quickly. There may be other regions of the parameter space, however, where a more involved interpolation technique may be needed to produce a root or a first approximation.

3.4.2. The immediate future. We are preparing a paper describing the problem and numerical techniques we employ. As well, we will relate this problem to the Kepler problem, discussing what techniques for solving Kepler's equation could be applicable in our case [33], and *vice versa*. For example, it appears that approximating the Kepler function by a cubic Hermite spline with knots at multiples of π or $\pi/2$ might be a viable approach to solving the KE in the near-parabolic case.

3.5. An extended rotating source

3.5.1. Superluminal volume sources. Another unique property of a superluminal polarization current is that it represents a true *volume* source [2]; by contrast, almost all conventional antennas are metallic, and therefore limited to *surface* currents because of screening [15]. From the standpoint of directed energy, this offers the potential to dump the energy radiated from an extended four-dimensional volume of source space-time at a single space-time point. The issue is also related to pulsars, where it is thought that volumes of plasma $\sim 1 \text{ m}^3$ are responsible for the so-called “giant” pulses [14, 34, 35, 36].

3.5.2. Mathematical approach to volume extension. As a generalization of our previous studies of a rotating pointlike source [3] and as a prelude to treatment of a compact source with volume extension, we have been analyzing a model of a rotating compact source with extension only in the azimuthal direction. The first version of this model employed a pattern of electric polarization with magnitude varying over $\hat{\varphi}$ as a power of cosine scaled by a width parameter $\hat{\varphi}_0$:

$$P(\varphi) = \begin{cases} \cos^n\left(\frac{\pi\hat{\varphi}}{2\hat{\varphi}_0}\right) & -\hat{\varphi}_0 \leq \hat{\varphi} \leq \hat{\varphi}_0 \\ 0 & \text{elsewhere.} \end{cases} \quad (21)$$

(We at first used $n = 2$, but later realized that because two derivatives of this function appear in the analysis, those derivatives, at least, should be smooth at the boundaries. Thus, we use $n = 4$, resulting in a distribution strongly resembling a Gaussian.) Analogously to a previous treatment of a full-circle source [4], evaluating the radiation field of this localized source involves a hypersingular integral, which we must regularize using the Hadamard finite-part procedure. This results in a collection of integrations with integrable singularities at the intersections of the source region with the bifurcation surface.

We evaluate the field for an observer situated at a critical angle off the axis of rotation,

$$\theta_p = \arcsin \left[\left(\frac{1}{\hat{r}^2} + \frac{\hat{r}^2 - 1}{\hat{R}_p^2} \right)^{1/2} \right], \quad (22)$$

upon which most of the energy of the source at radius r is focussed [27]. This places the source just inside the observer's bifurcation surface, near the cusp of that surface. We find that a source much narrower than the separation of the bifurcation sheets essentially reproduces the dynamic intensity and polarization characteristics of the pointlike source [3] (Fig. 46), while a source width much larger than this separation produces a pulse profile with two or three peaks and typically two rapid 90-degree shifts in polarization position angle. Figure 49 shows a pulse profile with a width that is on the order of nanoseconds (as observed in *giant pulses* [34, 35, 36]) for a rotational period on the order of tens of milliseconds. For a source velocity of $1.5c$, this corresponds to an emitting region on the order of meters wide. We also find that the shape of the pulse profile varies dramatically with the width of the emitting region (Fig. 50).

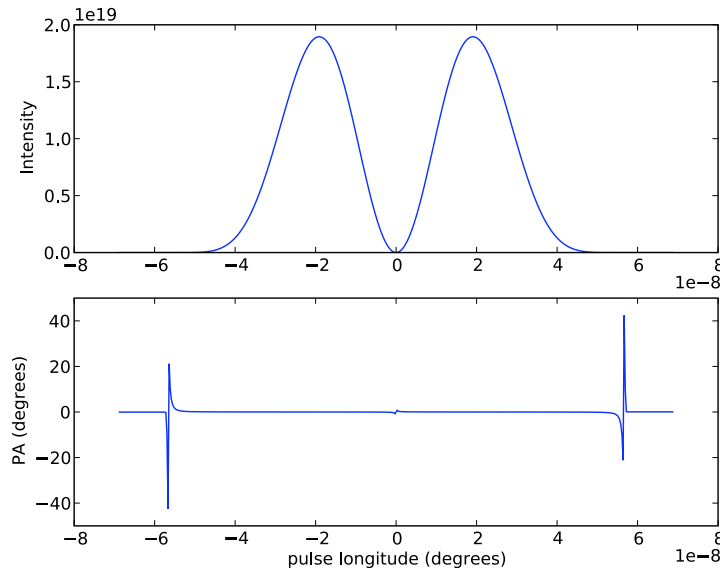


Figure 49. Pulse intensity and position angle for a source with azimuthal extent 4.2×10^{-7} radians, $\hat{R}_P = 10^{10}$, $\hat{r} = 1.5$, $\hat{r} \sin \theta_P = [1 + (\hat{r}^4 = \hat{r}^2)/\hat{R}_P^2]^{\frac{1}{2}}$.

3.5.3. Future development. We will complete our study of the azimuthally extended source by exploring the parameter space away from the cusp angle and publish our results. We will then build on this work by looking at integration in the radial and polar directions, as well. We will need to apply recent research in the numerical evaluation of highly oscillatory integrals [37].

4. Astrophysics

4.1. Introduction

An early motivation of the work in this program came from the suggestion that the emission from pulsars and other astrophysical objects involves superluminal sources [4, 3, 13]. For

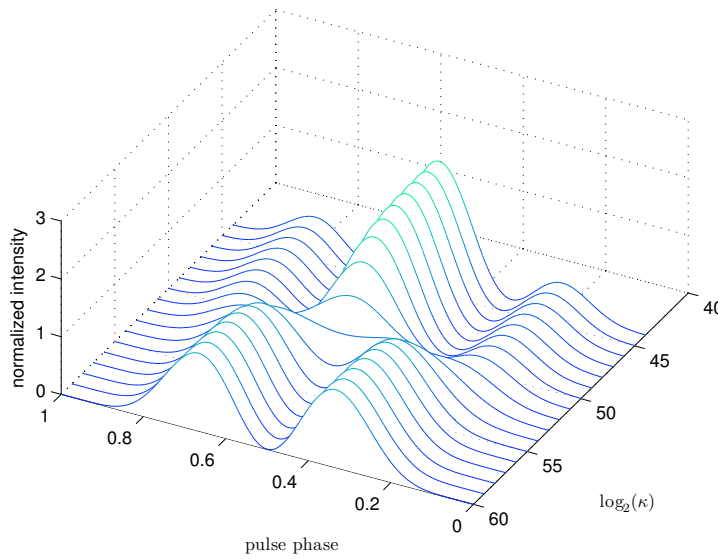


Figure 50. Variation in the shape of the pulse profile with azimuthal extent of the source. Pulse durations and intensities are scaled to facilitate comparison. The parameter κ is the ratio of the source extent to the separation of the bifurcation sheets.

example, a superluminal point-source model reproduced the general form of the Stokes parameters derived from pulsar observations [3].

During the course of the project we have developed this idea, so that a superluminal model is able to account both for the emission spectrum [14, 28, 38] and the intensity/distance relationship of pulsars [39].

4.2. Pulsar frequency spectrum

4.2.1. Application of superluminal emission to the Crab Pulsar. Recently, detailed observations of the proportionately spaced emission bands in the dynamic spectrum of the Crab pulsar were reported by Hankins and Eilek [40]. This oscillatory intensity immediately recalled earlier predictions of the emission of a rotating superluminal source [4, 12]; hence, it was apparent that the observations fitted the oscillations of the square of a Bessel function whose argument exceeds its order [14].

This function occurs naturally in the analysis of the emission from a polarization current with a superluminal distribution pattern: a current whose distribution pattern rotates (with an angular frequency ω) and oscillates (with a frequency $\Omega > \omega$ differing from an integral multiple of ω) at the same time [4, 12]. Using the results of this model, the dependence on frequency of the spacing and width of the observed emission bands can be quantitatively accounted for by an appropriate choice of a single free parameter, which is attributable to, and consistent with, the plasma frequency close to the emission region in a conventional pulsar magnetosphere [14]. In addition, the value of this parameter (obtained by fitting Hankins and Eilek's data) places the last peak in the amplitude of the oscillating Bessel function in question at a frequency that agrees with the position of the observed ultraviolet peak in the spectrum of the Crab pulsar [14]. By inferring the value of one further parameter from

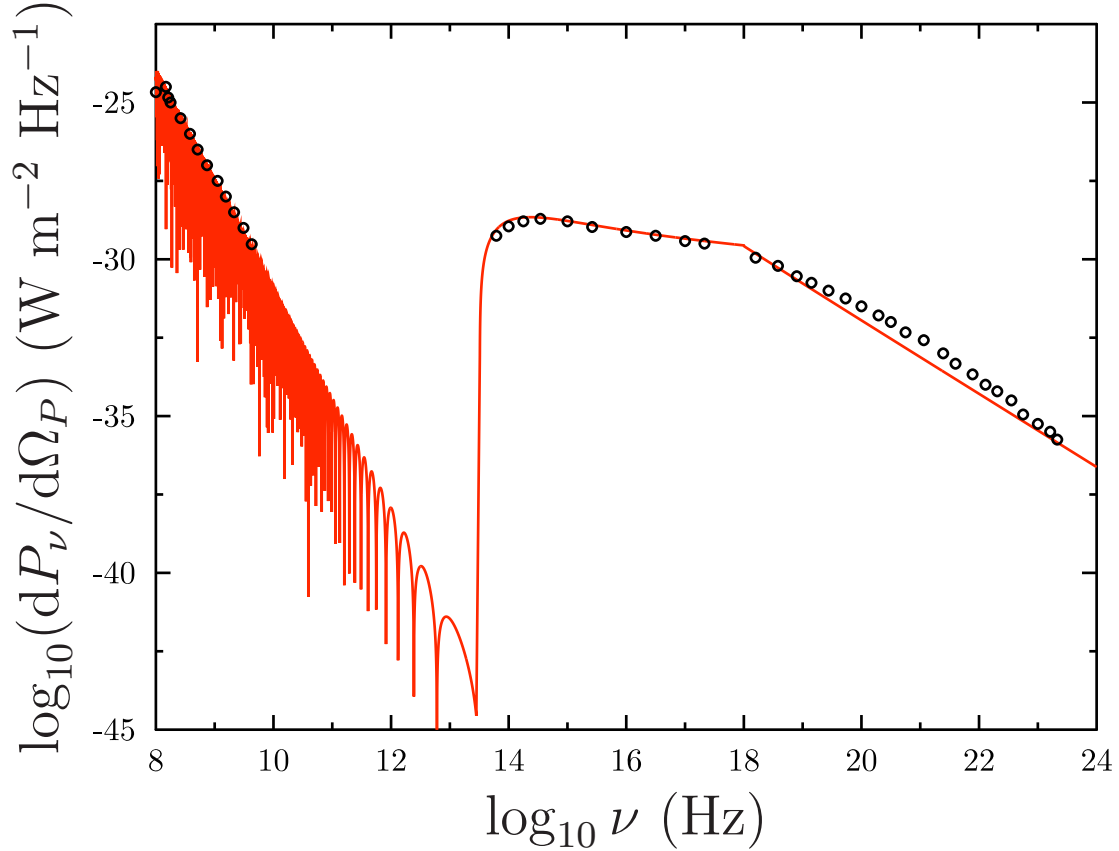


Figure 51. Measured emission spectrum of the Crab pulsar versus frequency in Hz. The points are observational data, the curve is the prediction of the superluminal model. In addition to fitting the overall shape of the emission spectrum, the same superluminal model was able to reproduce the intensity oscillations in the 1–10 GHz region reported by Hankins and Eilek [40] using the same parameters (after Ref. [14]).

observational data (a frequency consistent with electron cyclotron resonance in a conventional pulsar magnetosphere), and by mildly restricting certain local properties of the source, it is possible to account *quantitatively* for the emission spectrum of the Crab pulsar over 16 orders of magnitude of frequency (Fig. 51).

Within the same model, it was also possible to show how the suppression of the emission bands by the interference of the contributions from differing polarizations can account for the differences in the time and frequency signatures of the interpulse and the main pulse in the Crab pulsar [14].

4.2.2. Extension to other pulsars. The frequency spectrum of a rotating superluminal source is predicted to scale simply as $(\Omega/\omega)^3$, where, as before, ω is the angular velocity. To

lowest order, the features observed in the Crab pulsar should therefore also be present in the emission spectrum of other pulsars, but scaled appropriately by the rotation speed. Fast-rotating millisecond pulsars should therefore emit primarily in the MHz region (as they do) whereas slow rotators such as Geminga should emit far out into the ultraviolet/X-ray (as it indeed does).

We are currently engaged on gathering published pulsar data that span a wide enough range of frequency to test this idea. Thus far, the spectra of Vela, Geminga and B1929+10 have been studied [38]. For these three pulsars, it seems that the superluminal model provides an excellent fit of the observed data over a wide range of frequency (see Fig. 52). The same general features are seen as in the Crab spectrum, appropriately scaled by the rotation speed, as predicted. The differences (in the relative intensity of the various bands) are attributable to details of the magnetosphere of the pulsars [38]. However, the overall frequency spectrum seems to be “universal”.

Previous attempts to explain pulsar emission have employed different models for different (tiny) regions of the emission spectrum [41]. By contrast, the fact that the superluminal model, with only one or two adjustable parameters, can account for the emission spectra of several pulsars over many order of magnitude of frequency [14, 28, 38], gives strong support to our ideas.

4.3. Pulsar flux versus distance relationships

4.3.1. Introduction. Following our success in modeling the frequency spectrum of several pulsars, we are also testing a further prediction for rotating superluminal sources against observational data; that there is a component of pulsar emission whose intensity decays with distance d as $1/d$ [4, 27], rather than the conventional inverse square law (intensity $\propto 1/d^2$) that applies to conventional sources. Consequently, it is this component of a pulsar’s radiation that is bound to dominate observations made from a large distance (e.g., from Earth). By using measured fluxes at 1400 MHz (S_{1400}) and inferred distances of around 1700 pulsars from the Australia Telescope National Facility (ATNF) Pulsar Catalogue [42], we have shown that either the fluxes are much more compatible with the $1/d$ dependence than with the previously-assumed inverse square law or the distances quoted in the ATNF Catalogue [42] are subject to very significant errors.

The proposed component with intensity proportional to $1/d$ results from a general property of sources that travel faster than their emitted waves: that there is no simple relationship between reception time and retarded time [22, 23]. Multiple retarded times [4, 24, 27], or, if the source accelerates, extended periods of retarded time [27], can contribute to the waves received instantaneously, resulting in *temporal focusing*; i.e., focusing (concentration of the energy carried by the waves) in the time domain [11]. An analogous effect is well known in acoustics [22, 23, 24]. It is the temporal focusing from the parts of the source that approach the observer at the wavespeed and with zero acceleration that leads to the $1/d$ intensity dependence [27]. Note that this mechanism does not violate conservation of energy since the enhanced intensity detected in some places is compensated exactly by diluted intensities

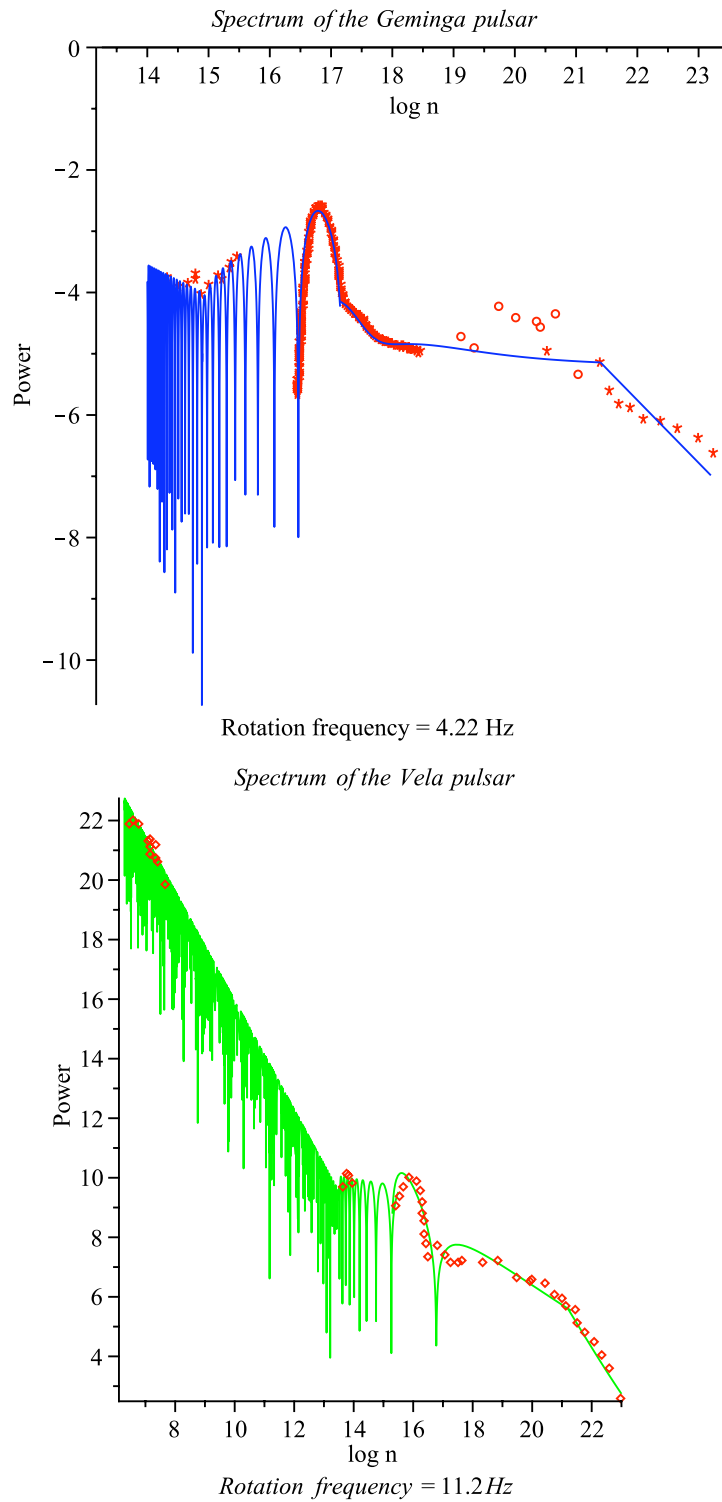


Figure 52. Emission spectra of the Geminga (top) and Vela (bottom) pulsars; points are observational data, and curves are the prediction of the superluminal model. The emission frequency is given in terms of a multiple n of the rotation frequency to aid in comparing the spectra.

elsewhere [27]. We also emphasize that the emission discussed in this (and previous) sections arises from true superluminal motion; electromagnetic disturbances (polarization currents) that travel faster than c [11]. This should not be confused with the concept of *apparent* superluminal motion, an idea has been applied mostly to radio sources and interpreted as relativistic aberrations in the line of sight [43].

4.3.2. Overview of data used in the analysis. The analyses below assume that the populations of pulsars at various distances from the Earth are similar; each population will have a representative spread of different pulsar types, sizes and energies.

We take our 1400 MHz flux and pulsar distance data from the ATNF Pulsar Catalogue [42] (<http://www.atnf.csiro.au/research/pulsar/psrcat>). To eliminate statistical biases from different instruments, we further restricted the sample to those pulsars detected using a single instrument, *i.e.*, the Parkes Multi-beam Survey [44]. In this catalogue, the overwhelmingly most common determinant of distance is dispersion measure [45, 46, 47], with other methods employed only rarely. Fortunately, pulsars have never been previously assumed to be, nor used as, standard candles, so that the number of distances contaminated by the assumption of a conventional inverse square law ($1/d^2$), at least for *their* intensities, is likely to be insignificant. We choose the most recent implementation of the dispersion model to evaluate our distances [47].

Fig. 53(a) plots almost the entire Parkes Multibeam Survey out to a distance of 20 kpc as $\log_{10}(S_{1400})$ versus $\log_{10}(d)$, where d is the distance, in Fig. 53(a), the only exclusions being pulsars in globular clusters. We omit globular-cluster pulsars because they likely represent a non-standard population compared to pulsars in our Galaxy, and because the method of observation employed in their observation is very different [41].

In Fig. 53(a), the limited sensitivity of the detection equipment used to observe the pulsars is immediately obvious: the data set contains very few observations with $S_{1400} \leq 0.06$ mJy, and the point density appears diluted up as far as ~ 0.2 mJy. As we shall see below, a very significant number of pulsars in this region are not detected; as the distance increases, an increasing fraction of the weaker pulsars therefore will be absent, biasing the *observed* population towards the pulsars with greater fluxes.

If a straight-line fit of all of these data is made, the gradient is -0.30 ± 0.05 , implying that $S_{1400} \propto d^{-0.30}$. Such a fit should, however, be treated with extreme caution for the reasons discussed in the previous paragraph; as the distance increases, the population sampled will be increasingly biased to the higher-intensity pulsars. Thus, at larger distances, any form of mean S_{1400} will be artificially high compared to the true value.

4.3.3. Observed cumulative distribution functions. One of the most commonly used ways to test limited amounts of data for the validity of any statistical distribution is to use its cumulative distribution [48]. To assess the effect of distance on S_{1400} cumulative distributions, we group the pulsar data in bins covering certain distance ranges (*e.g.* 8.5 – 10 kpc). The distance bins were chosen so that they contained a large enough population for meaningful statistical analysis (if possible, 50 – 150 pulsars). However, we were also aware that a

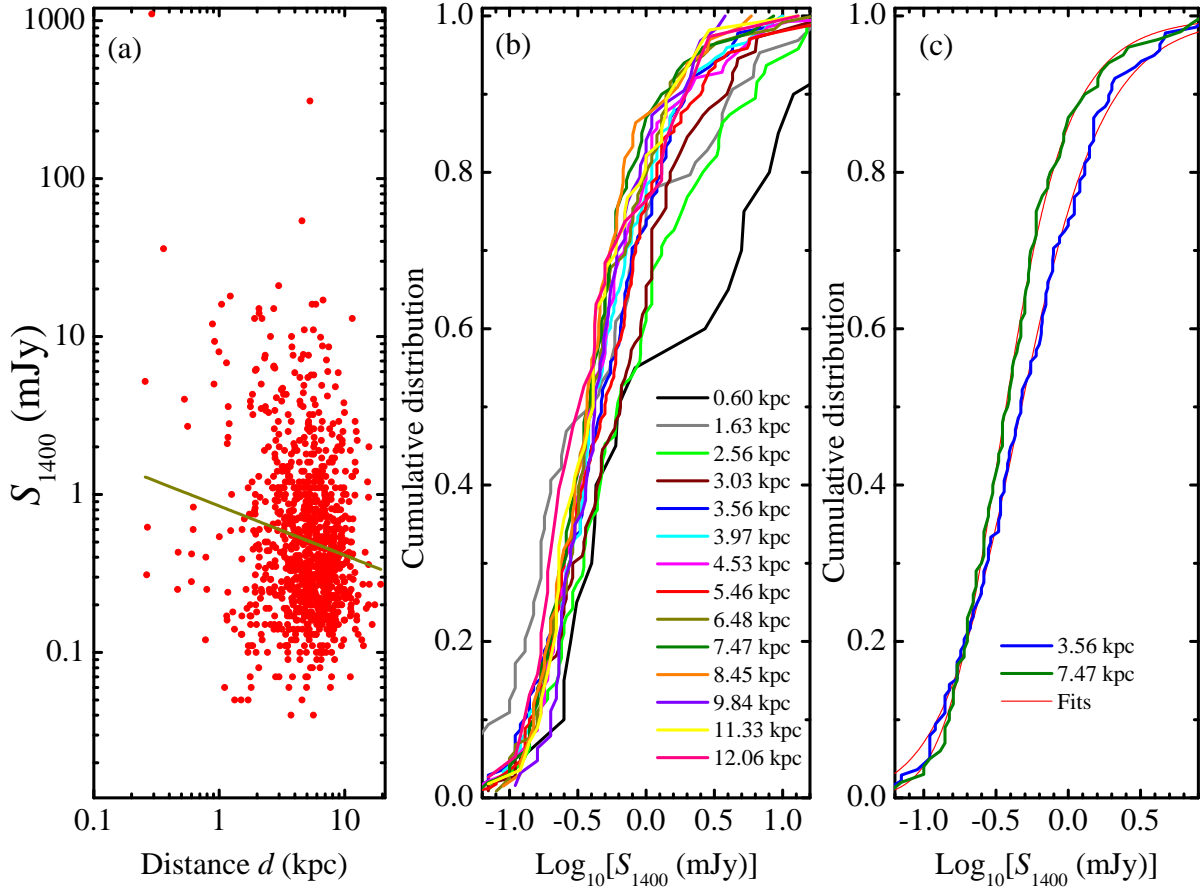


Figure 53. (a) The Parkes Multibeam Survey (globular clusters excluded) plotted as S_{1400} versus distance d (points) out to $d \approx 20$ kpc. The line is a “blind” straight-line fit to $\log_{10}(S_{1400})$ versus $\log_{10}(d)$; its gradient is -0.30 . (b) Cumulative population distribution in S_{1400} for 11 distance bins. The mean distance of each bin is given in the inset key. (c) Example fits (red) of the skewed Fermi-Dirac function (Eq. 23) to two of the cumulative population distributions taken from (b).

significant change in S_{1400} may be occurring as a function of distance \S , precluding very wide distance ranges for the bins. Fig. 53(b) plots the resulting cumulative distributions for 11 distance bins, with mean distance spanning the range 0.6 – 12 kpc.

The first noticeable aspect of Fig. 53(b) is that all of the cumulative distribution functions tend to zero at roughly the same value of S_{1400} . This is, of course, a manifestation of the lower limit of sensitivity of the Parkes instrument; the distribution functions bottom out close to the notional minimum $S_{1400} \approx 0.06$ mJy already alluded to in Section 4.3.2.

By contrast, we would expect the high- S_{1400} parts of the distribution functions (*i.e.* where they tend towards 1) to be much less affected by the loss of low-intensity pulsars. Taking,

\S For example, one might expect $S_{1400} \propto d^{-2}$ if pulsars are “conventional” sources.

for example, the 90% points of the distribution functions, one is immediately struck by the small spread of S_{1400} values: for distances ≥ 1 kpc, the 90% points cover roughly a factor five in S_{1400} , even though the mean distance varies by a factor around 7.5. This is already an indication that the S_{1400} values are varying more slowly with apparent distance than one might expect for the inverse square law.

With the exception of the data for 0.60 kpc (which probably represent too wide a spread of distances and too small a sample for useful analysis), the cumulative distribution functions in Fig. 53(b) are fitted very well by the skewed Fermi-Dirac function

$$N_{\text{cum}} = \frac{1}{1 + \exp(\alpha S^\eta - \beta)}, \quad (23)$$

where S_{1400} has been written S for brevity and α , η and β are constants. Typical fits are shown in Fig. 53(c). Note that we do not believe that there is any physical significance in these good fits; Eq. 23 is merely of the correct form to give a smoothly-varying representation of the data.

The fitted curves for each distance bin can be differentiated to yield an apparent luminosity function $dN_{\text{cum}}/d\log_{10}S_{1400}$; typical examples are shown in Fig. 54(a). As the distance increases, the high-flux part of each curve moves to lower S_{1400} , as expected. However, the low-flux side of each curve is effectively fixed, showing that this part of the apparent luminosity is in fact an artifact of the drastic fall-off of the instrumental response at small fluxes.

This point is further emphasized by looking at the second derivative of the fitted skewed Fermi-Dirac functions for each distance (Fig. 54(b)). The peaks at low flux, representing the maximum gradients of the apparent luminosity functions (Fig 54(a)) remain essentially immobile as the distance is varied, suggesting that the number of pulsars seen is effectively determined just by instrumental response. On the other hand, the minima at high flux move to lower S_{1400} values as the distance increases, indicating that this part of the apparent luminosity is representative of the true luminosity function. The positions of these minima (Fig 54(c)) strongly suggests that $S_{1400} \propto 1/d$.

All of the analysis thus far points to the inadequacy and incompleteness of the Parkes Multibeam Survey; according to the various curves in Fig. 54(a) and (b), the chance that a pulsar is detected falls very dramatically for $S_{1400} \leq 0.4$ mJy. As we shall see below, this means that the vast majority of pulsars in our Galaxy have yet to be detected.

Fortunately, a method of analysis due to George Efstathiou [49] has been previously applied to an analogous problem, the red-shifts of very distant objects. Efstathiou also had to deal with missing data due to instrumental limitations, and in the next section we use an adaptation of his method to deal with the Parkes database.

4.3.4. Maximum likelihood evaluation of pulsar luminosity function. We analyze the data from the Parkes survey to construct a luminosity function for the pulsars. Our goal is to investigate whether such an analysis can help us ascertain the nature of decay of power with distance. We employ a maximum likelihood method [49] for determining the luminosity function, $\phi(L)$, based on the observed data. The probability that a pulsar at distance d and

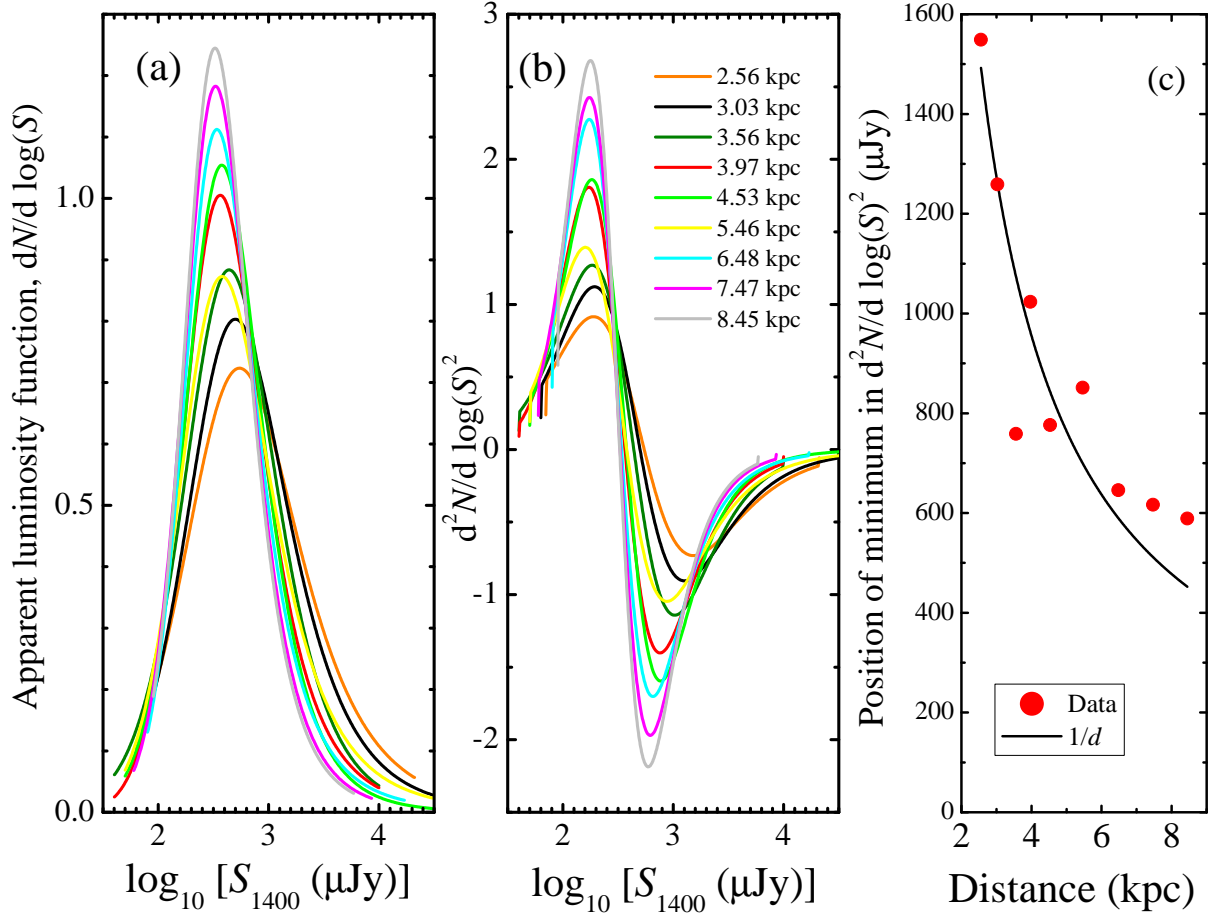


Figure 54. (a) The apparent luminosity functions for various distance bins obtained by differentiating the fits of Eq. 23 to the observed cumulative distribution functions (*e.g.* Fig. 53(c)). Note that the low-flux side of each curve is very similar, showing that this part of the observation primarily reflects the instrumental response, and not a true luminosity function. The high-flux side, however, moves to lower S_{1400} values as the distance increases. (b) Differentiation of the functions plotted in (a), showing that the low-flux side of each apparent luminosity function (the maximum) is essentially distance-independent, *i.e.* determined by the instrument, and not an intrinsic feature of the true distribution. On the other hand, the high-flux side of the function (minimum) moves to lower S_{1400} with increasing distance; this suggests that it is an intrinsic part of the luminosity function, and not an instrumental artifact. (c) Minima positions from (b) plotted as a function of distance d , showing that the characteristic high-flux part of the luminosity function corresponds to $S_{1400} \propto 1/d$.

luminosity L_i is observed is given by

$$p_i \propto \phi(L_i) \int_{L_{\min}(z_i)}^{\infty} \phi(L) dL. \quad (24)$$

We can define a likelihood function

$$\mathcal{L} = \prod_i p_i$$

We utilize a technique that does not assume a simple functional for $\phi(L)$. Instead we parameterize the luminosity function as N_b steps.

$$\phi(L) = \phi_k, \quad L_k - \frac{\Delta L}{2} < L < L_k + \frac{\Delta L}{2}, \quad k = 1, \dots, N_b \quad (25)$$

The maximum likelihood function assumes the form

$$\ln \mathcal{L} = \sum_{i=1}^{N_p} W(L_i - L_k) \ln \phi_k - \sum_{i=1}^{N_p} \ln \left(\sum_{j=1}^{N_b} \phi_j \Delta L H[L_j - L_{\min}(z_i)] \right) + \text{const.} \quad (26)$$

where N_p is the total number of pulsars in the Parkes survey.

$$H(x) = \begin{cases} 0, & -\Delta L/2 \leq x \leq \Delta L/2 \\ 1, & \text{otherwise} \end{cases}$$

and

$$W(x) = \begin{cases} 0, & x \leq -\Delta L/2 \\ (x/\Delta L + 1/2), & -\Delta L/2 \leq x \leq \Delta L/2 \\ 1, & x \geq \Delta L/2 \end{cases}$$

The parameters ϕ_k determining the luminosity function are given by the self-consistent set of equations

$$\phi_k \Delta L = \frac{\sum_i W(L_i - L_k)}{\sum_i \left(H[L_k - L_{\min}(z_i)] / \sum_{j=1}^{N_b} \phi_j \Delta L H[L_j - L_{\min}(z_i)] \right)}, \quad k = 1, \dots, N_b \quad (27)$$

The above equations are solved iteratively to obtain the luminosity function.

The Parkes survey lists the measured fluxes S and the distances d . To carry out the computation, we assume that the intrinsic luminosity is related to the fluxes by

$$L = S * d^n. \quad (28)$$

We used the above technique of determining the luminosity function by trying both $n = 1$ and $n = 2$. The success of the Maximum Likelihood method is determined by evaluating an error measure (Fig. 55). For $n = 1$, the error measure was found to be 3×10^{-6} using the entire Parkes dataset. For $n = 2$, the dataset had to be restricted for convergence to occur (*i.e.* 12 “troublesome” pulsars were excluded), and the error measure was 0.14. The error is roughly 5×10^4 times worse for $n = 2$ than for $n = 1$.

In summary, we find that the Maximum Likelihood Method works particularly well when we assume a $1/d$ fall off of the flux with distance. This is consistent with the hypothesis of a component of non-spherically decaying radiation from pulsars and in strong support of the superluminal model.

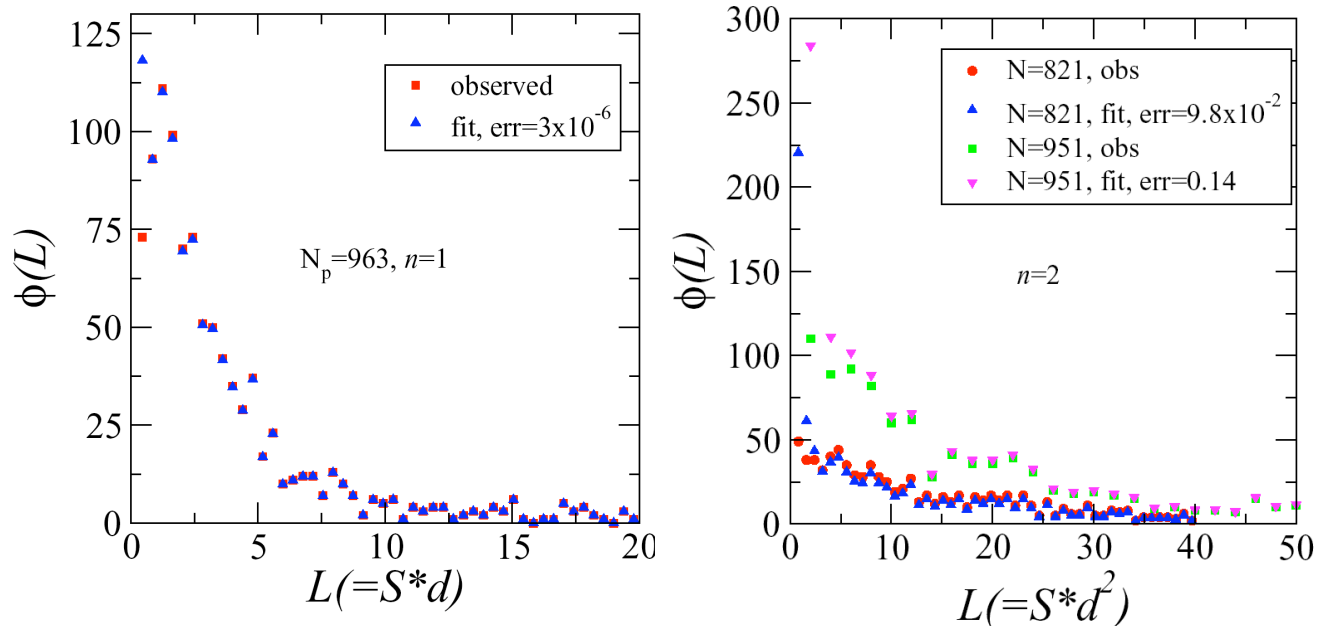


Figure 55. Maximum likelihood fits for $n = 1$ (left) and $n = 2$ (right).

4.3.5. Bayesian statistical analysis. In order to further study the Parkes Multibeam Survey, a Bayesian statistical analysis is underway [50]. Some preliminary results (Fig. 56) illustrate the likely (enormous) populations of undetected pulsars in our Galaxy.

4.3.6. Future work. We intend to publish the frequency and distance survey work [38, 39] in the near future, followed by the Bayesian analysis [50]. Subsequently, our attention will refocus on data mining gamma-ray-burst observations in a search for phenomena attributable to superluminal emission.

4.4. The Lick Observatory Gamma-Ray-Burst Afterglow Experiment

4.4.1. Introduction. One prediction of the Superluminal Polarization Current theory of pulsar emission, where the pulsed emission arises from polarization currents induced beyond the light cylinder by the rotating pulsar magnetic field [14], is that one component of the pulsed radiation diminishes as $1/d$ (where d is distance), rather than $1/d^2$. This model also predicts that pulsed emission in circumstances where there is plasma at several (n) light-cylinder|| radii is directed at an angle of $\arcsin(1/n)$ from the rotation axis. Observations of the afterglows from gamma-ray bursts, the optical to infrared radiation which decays by orders of magnitude within a day, indicate that these also diminish less rapidly than $1/d^2$, indicating that this emission may be pulsed as well, and indeed may provide the mechanism which drives the gamma-ray burst itself. Accordingly, we have mounted an experiment on the Crossley 36-inch reflecting telescope at Lick Observatory, which had been unused for

|| The light cylinder is the cylinder of radius r at which $\omega r = c$.

Model results

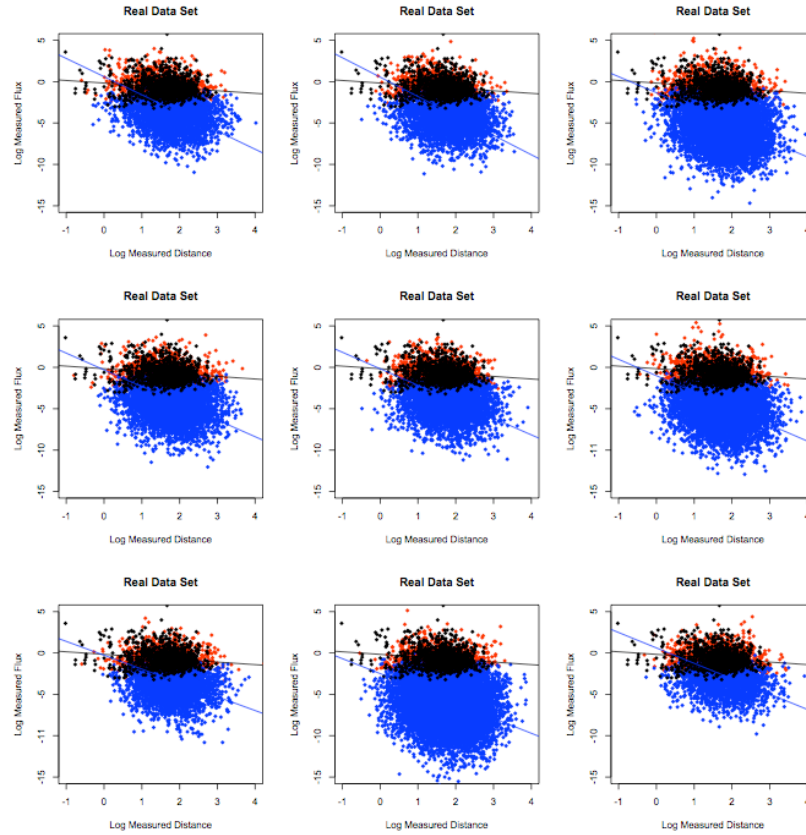


Figure 56. Some results of Bayesian analysis of the Parkes Multibeam Survey. The Black dots are real observations; red dots represent members of synthetic populations that would be detected by Parkes, and the blue dots represent likely populations of undetected pulsars.

several years, using a photoelectric detector and a fast recording system capable of data rates of 500,000 samples per second.

4.4.2. The initial setup made in late July of 2008. The capability to record time series data at a high rate has been virtually wiped out by the rush, over the past dozen years or so, to commission high quantum efficiency, integrating, solid state detectors, and the appearance that observing supernovae with these could yield reliable cosmological parameters. Without a working photometer, with apertures, filters, dark slide, offset guiding mechanism, and so on, the only other way to go would be to commission both a time- and imaging detector, which would still need an iris for protection, and other items for cooling, mounting and auxiliary support: an expensive proposition and one for which there were insufficient resources from LDRD DR20080085 as of the summer of 2008, as well as currently.

Among the casualties were the phototubes and photoimeters at the Kitt Peak and Cerro Tololo Inter-American Observatories, the very fine photometer designed by William Kunkel, former director of the Las Campanas Observatory, and the very convenient offset photometer at the former 24-inch telescope at Lick Observatory, which was replaced by the 0.75-m Katzman Automated Imaging Telescope (KAIT – the 24-inch scope went to Kitt Peak, and the photometer is boxed up in the tunnel beneath the Shane 3-meter). However, one photometer which had not been replaced as of the summer of 2008 was that on the neglected Crossley 36-inch reflector. Also available were the cold boxes which interface with the Crossley photometer, and contained old photoelectric tubes, which we replaced with a more red-sensitive tube, a \$950 Hamamatsu R7400U-20. Lick Observatory is well located for observing in the late Spring, Summer, and early Autumn, when the weather is very dependable, and when it is not as dependable at Fenton Hill.

Ancillary electronics and a laptop were gathered from Lick and LBL. The laptop was used with a unit purchased from Keithley Industries, (formerly ‘Metabyte’ Division), the KUSB-3116, which is programmable using a screw terminal accessory and strip cable(s) from this accessory to the 3116 unit. Software to control the 3116 with the laptop was compiled by LANL retiree, Brook Sandford. A Rubidium frequency standard was borrowed from Larry Earley’s Lab. at TA-53, and an OEM GPS unit was supplied by Kostas Chloros at Lick Observatory to complete the experimental capability to record data at a reliable rate and with reference to an absolute time.

4.4.3. Observations. We have manned the Crossley during 7 trips for a total of 32 nights between late July, 2008, and late March, 2009, a duty cycle of about a sixth. One Swift Observatory trigger, with an afterglow of $m_V < 17.8$, occurs per month, and the Crossley setup can easily work down to a V magnitude of 19, given a time series lasting more than a few minutes. A K2 star with $m_V = 8.92$ produces about 2,000,000 counts per second (a quite surprising number which is about 5 times higher than expected, but rates from other sources appear to be consistent with this value and their statistics have been checked by Fourier transforms), which means $m_V = 17.8$ produces about 561 counts per second. The background rate in a 0.26 mm aperture (10 arc s in diameter: the smallest) is about 1000 counts per second at lowest. In the best circumstances, a pulsar with $m_V = 22.7$, or 6 counts per second, could be detected in 4,000 seconds. Acquisition has to be by blind offset for sufficiently faint targets. Thus a V magnitude of 22 seems to be accessible to this experiment (there will be a considerable frequency derivative for such pulsars, but we can compensate for this, and we have ignored gains in sensitivity due to low pulsar duty cycle). During a five night run, there is usually an accessible afterglow brighter than $m_V = 22$.

4.4.4. Where we are now and where we might go. Since late July, 2008, when the experiment began, there have been two observations of GRB afterglows with KAIT, which is a lower limit for the number of, in principal, afterglows accessible to our experiment on the Crossley. Both have occurred in bright moon, with the brightest one, near magnitude 16, on 2009, March 13, about 22 degrees away, and increasing with time, from a moon only two days past full. Since

the rainbow angle, in moonlight scattered by cirrus clouds, is 23 degrees, KAIT was only able to get a glimpse of the afterglow, and could not follow up.

Other afterglows, with an R magnitude >19 , were close calls, but ultimately out of reach of the current setup and telescope and possibly weather, without a time series lasting several hours. We hope to improve our ability to do this with minor improvements to the offset guide configuration on the Crossley photometer.

Currently, in the high power eyepiece, the focus of the star field is about 1/8 inch closer to the observer than that of the reticle (which is split into the field by a prism with a 45 degree surface). This can be improved by replacing two flathead screws with 1/4 inch heads, with screws that have heads with smaller diameters, and moving the splitting prism closer to the observer by the difference in radius. Inverting the aperture disks would also buy another 32nd of an inch or so.

4.4.5. The 30-inch Hands-on-Universe Telescope. This telescope was rat-infested while still packaged at Fenton Hill Observatory. Lacking the \$100K requested from the UC-LANL collaboration fund to automate this telescope, staff at Argonne National Laboratory are available to commission this telescope locally. When this telescope becomes automated, we will suggest that it be relocated to Fenton Hill, where observing conditions are superior, and frequently complimentary, to those at Lick Observatory. We can clone the data-taking electronics we have at Lick for about \$10K.

Attempts to record time-series data of afterglows will continue.

5. Outreach to sponsors

5.1. Introduction

From the onset, this project has recognized the need to include an aggressive technology transfer and program development efforts to leverage the advancements of the superluminal technology. Several efforts have been initiated in the past year and a half of the period of performance. While we have explored a number of promising directions, further action is contingent on the project reaching the technology demonstrator milestones.

The concepts and technology developed under this LDRD-DR can be exploited in three principal ways:

- outright commercialization,
- military and related applications, and
- astronomy and astrophysics applications

We recognize that the first two are not independent and that there exists some tension between the two areas. We will lump these two together since military (and related) applications will be mostly niche markets of more generally applicable uses, such as radar.

5.2. Oxbridge Pulsar Sources Ltd.

Prior to the availability of funding and because of the speculative nature of the superluminal concept, LANL Technology Transfer (Susan Sprake and others) advised the current PI to set up a holding company with the other two coinventors (H. and A. Ardavan) to serve as a vehicle for commercialization and intellectual property protection. The company is known as Oxbridge Pulsar Sources Ltd. (registered in Cambridge, UK) but at the present is a mere skeleton.

We have conducted a series of discussions with Christopher van Essen, Chair of the Board of Oxbridge Pulsar Sources (OPS) Ltd., and formerly of Boeing, to explore co-operative development and licensing of the superluminal technology. These discussions have involved the staff at the Technology Transfer Office, principally Kathleen McDonald and Belinda Padilla. OPS now wishes to develop the technology for radar applications.

The PI, John Singleton, is a shareholder in OPS, and now that LANL funding has been forthcoming, this poses an obvious conflict of interest. The most straightforward solution here will be for the PI to renounce his shareholding in OPS. *The timing of this event will be coordinated with the acceptance of any CRADA by both parties (LANL, OPS).*

LANL formal procedures require us first to establish a non-disclosure agreement (NDA) with OPS. With this in place, the negotiations as to the terms of the Cooperative Research and Development Agreement (CRADA) can begin.

The PI is refreshing his Form 701 paperwork (“Outside Activity Permission Request”) prior to the CRADA/share discard referred to above.

5.3. Commercialization

In determining commercial potential, we must first assess whether the maturity of our technology is sufficient to attract a commercial partnership. While our early field demonstrations have verified the underlying principles, the new demonstration machines will provide a more convincing case for technology partnerships.

Within the life of the current project, the original inventors have defended superluminal intellectual property through a patent filed via LANL Tech Transfer [8]. With progress in the current project, we anticipate that our IP can be expanded into a multiproduct cluster of applications *e.g.* efficient communications, radar applications, secure communications, directed energy applications, medical). Of course, there are competing technologies for these markets and we have yet to analyze our position relative to those of our competitors.

5.4. Other issues

As part of the path towards commercialization and to comply with LANL’s management of intellectual property, two members of the project team (Perez, Junor) have taken the Lab’s “Managing Intellectual Property” class developed and organized by the Technology Transfer Division and the Laboratory Counsel’s Intellectual Property Office.

Project team member Junor has reviewed possible issues with dual-use technology and export control with the staff at SAFE-1 (Sandy Bonchin, Larry Collins). In the context of agreements with the associated UK company (OPS), their guidance was

- to specify in sufficient detail the nature of the work and the mutual expectations, and the materials and the intellectual property which would be transferred, and
- to define the obligations for the UK company with respect to export control.

SAFE-1 will review any collaborative agreements for export control and ITAR issues.

5.5. DOE Intelligence

At the beginning of the LDRD period of performance (October 2007), DOE Intelligence approached the team in order to understand the scope of the work, with a view to using this technology for future applications of interest to this office. Several interactions were held with the DOE Program Manager regarding communications and encryption applications. Due to restrictions derived from security clearance issues, PI Singleton (currently a foreign national) could not participate in these exchanges; instead, Co-PI Fasel and other team members represented the interests of the project.

Our agreement with DOE Intelligence is that once TD1 (Technology Demonstrator 1) is field-tested and working routinely, negotiations will start to receive additional funding to explore certain applications of interest to the DOE intelligence community.

5.6. DARPA

We have initiated discussions with DARPA's Strategic Technology Office (STO) and Tactical Technology Office (TTO) to assess their interest in superluminal transmitters for power efficient communications and countermeasures resistant waveforms. These two features of our technology seem most appropriate to their needs but we will explore other possibilities.

The typical path forward here is to generate a White Paper (or Papers) to define possible scope of work under seedling funding (around \$300k or less) for a period of performance typically 1 year or less. Contingent on success, DARPA will then solicit formal proposals (usually in response to a BAA) for demonstration projects at the \$1–2 M level. This level of project requires well-defined advancement and exit criteria. In parallel with the technical component, we must also work to develop interest in the services to transition the technology to real-world applications, usually through industrial partnerships or with LANL in a consultancy role.

5.7. Raytheon and L-3

Members of the LDRD team met with Raytheon personnel at LANL interested on superluminal applications in telecommunications (John S, Joe and Larry were part of these exchanges). Exploratory conversations were held with L-3 personnel on the radar and encryption capabilities of the superluminal technology.

5.8. USAF radar solicitation

We investigated a BAA solicitation released by the Department of the Air Force/Air Force Materiel Command/AFRL for Innovative Radar Sensor Technology (BAA-09-02-RIKA) on January 22, 2009. The funding opportunity description reads:

AFRL Rome Research Site is soliciting white papers for innovative approaches in the area of advanced radar technology that will overcome deficiencies in existing and planned radar systems to detect, track, and identify aircraft, missiles, spacecraft, space debris, ground vehicles, and subsurface complexes in clutter and countermeasure environments. The survivability of new and existing systems must also be improved without the use of decoys. Upgrades to existing Intelligence, Surveillance and Reconnaissance (ISR) Platforms and demonstrations to support transition to the next level of technology development, and evolutions to new sensors and concepts (Unmanned Air Vehicles, Space Based Platforms, etc.) need to be addressed. Sensor concepts should include multiple configurations with characteristics supporting diverse multimission requirements including Airborne Moving Target Indicator (AMTI), Ground Moving Target Indicator (GMTI) and Synthetic Aperture Radar (SAR), Multiband SAR/Tomographic Imaging features, and Foliage Penetrating (FOPEN) Radar. These concepts include both Monostatic and Multistatic solutions. Lookdown Bistatic concepts should include bistatic receivers using radiators of opportunity (TV, FM etc.) with large wideband receive antennas. Areas of interest include new and innovative advances in system architectures, hardware, software and/or signal processing algorithm improvements, diverse transmit waveforms, survivability, positional estimation improvements, unique concepts in radar system design, Multi-Basing Look Down Surveillance (Air and Space), Augmentation of Reconnaissance Capabilities (development of new surveillance capabilities in Reconnaissance sensors), Ground Penetrating Radar, Bistatic/Multistatic Radar (Non-cooperative emitter stand alone sensors and Cooperative augmentation of existing ISR Platforms through UAVs), the architecture and signal processing for expendable UAV radar probes and theater missile defense. Additional technology areas include the measurement, test, analysis and modeling efforts that are required to support the development of advanced radar systems. The primary emphasis is to identify and demonstrate promising technologies for both monostatic and multistatic radar sensors in the areas of Space Time Adaptive Processing, both Adaptive and Knowledge Based (KB), Multi-Channel Signal Processing Techniques, Innovative and Wideband Processing Techniques, Multi-Dimensional Processing Techniques, Improved radar system performance developments in spread doppler clutter environment for a theater application and, in general, technologies that may significantly improve the performance of advanced radar systems. The successful application of these approaches will require a broad spectrum of expertise, covering hardware, software, and systems technology.

The scope of this call would seem to be broad enough to accommodate the use of superluminal transmitters.

The effective submission window for FY10 proposals closes on October 1, 2009. Projected funding for FY10 is \$8.3 M with contracts ranging between \$100 k to \$4.9 M per year.

As in many of these solicitations, funding has not been obligated up front and the LANL DoD proposal office sees these calls as “fishing expeditions”. Consequently, the project team has not decided whether to respond to this solicitation or not; our current sense is that there are better directions to explore for new funding and applications.

5.9. NASA

First, a member of our LDRD team (Mario Perez) during FY08 took an IPA position at NASA-HQ, Washington DC, as Program Scientist within the Astrophysics Division. This will help the LDRD team to better understand theory, data analysis, technology development, and flight opportunities in the near future within NASA. Although this is certainly a great advantage and gain for the team and LANL in the long term, this also impacted the manpower count of the current team.

Subsequently, last year we submitted a proposal to NASA’s solicitation for its Astrophysics Theory and Fundamental Physics (ATFP) program entitled “Radiation Theory of Astronomical Sources That Move Faster than Light: Applications to Pulsars”.

In our proposal, we sought to develop further the superluminal model of pulsar radiation to account quantitatively for the dynamic intensity, spectrum, and polarization of observed pulses. This work would facilitate the interpretation of data from space astrophysics missions and allow predictions to be made that would be tested by space astrophysics observations. The proposed work would support NASA strategic subgoal 3D and specifically would apply to category 2 (Post-Main-Sequence Stars and Collapsed Objects) of the ATFP program. Our model would also find application to related phenomena, such as gamma-ray bursts (category 3) and quasars (category 8).

Our proposal was unsuccessful for several reasons. The first was obvious: our institutional cost model makes LANL proposals rather uncompetitive compared to those from academic and quasi-academic institutions (*e.g.* SWRI). The apparent priciness of our proposal (\$815 k over 3 years) when coupled with our existing LDRD-DR support (total budget of \$4.145 M over 3 years) put us at a distinct disadvantage.

The second reason for our proposal’s failure is that we did not communicate effectively the underlying science and to connect this strongly to NASA’s mission objectives. We accept that, since our project team is relatively inexperienced in the ways of NASA, our first NASA proposal may be a “dues paying”, learning experience. However, we do understand that there is a steep learning curve for any reviewer of such a proposal from us since our foundational documents are heavily mathematical [3, 27, 26].

Finally, the novelty of our model, which challenges conventional models of pulsar emission energetics [14, 28], may be difficult to accept for volunteer reviewers, many of whom

are not specialists in these particular fields, and who may have a large number of proposals to consider.

Nevertheless, we feel that the astrophysical applications of the superluminal model is so profound that we will make another proposal to NASA this year.

NASA has released its annual Research Opportunities in Space and Earth Sciences (ROSES) omnibus call for proposals (Solicitation NNH09ZDA001N). Our work under the LDRD-DR is most germane to NASA's Astrophysics Research Program (described in Appendix D of the solicitation). Three broad areas are open to us potentially.

5.9.1. Astrophysics Data Analysis. The solicitation reads (in part):

The Astrophysics Data Analysis program (Appendix D.2) supports the broad range of data analysis efforts relating to past or current NASA astrophysics space missions regardless of the physical phenomena studied.

5.9.2. Astronomy and Physics Research and Analysis. Here the solicitation reads:

The Astronomy and Physics Research and Analysis program (Appendix D.3) supports investigations in the areas of suborbital flights, detector development, supporting technology development, laboratory astrophysics, and limited ground based observing. Basic research proposals are solicited for investigations that are relevant to NASA's programs in astronomy and astrophysics and include research over the entire range of photons, gravitational waves, and particles of astronomical origin.

5.9.3. Astrophysics Theory. This part of the Solicitation is probably our best opportunity. The guidance reads (in part):

The Astrophysics Theory program (Appendix D.4) supports theoretical investigations or modeling of the astrophysical phenomena targeted by past, current, or future NASA astrophysics space missions.

We note that this part of the solicitation no longer supports laboratory work related to NASA's strategic goals in gravitation and fundamental physics. Such efforts are now supported in the Astronomy and Physics Research and Analysis program. (Section 5.9.2).

5.10. NASA Deep Space Network

We have had some very preliminary discussions with Jet Propulsion Laboratory about the use of superluminal transmitters and their very desirable $1/R$ law for Deep Space Network communications.

5.11. CIA and others

A fellow from ISR-2 that participated in joint discussions of communication protocols volunteered to present the superluminal technology to John Phillips (CIA Chief Scientist) and others in order to probe their interest. However, any attempt to move forward in that direction would only take place after the TD1 was field-tested and operationally working, which is still a milestone in the near future.

5.12. Other outreach

5.12.1. Conference summaries

- (i) “The Kinematics of the SN 1987A Beam/Jet(s)”, 2008, John Middleditch, M.R. Perez, Bulletin of the American Astronomical Society (BAAS), Vol. 40, No. 2, 206, St. Louis, MO Meeting, June 1-5, 2008.
- (ii) “The SN 1987A Beam/Jet and Its Associated Mystery Spot”, 2008, John Middleditch, M.R. Perez, Bulletin of the American Astronomical Society (BAAS), Vol. 39, No. 4, 742, Austin, Texas Meeting, January 7-11, 2008.
- (iii) “Superluminal Emission Processes as a Key to Understanding Pulsar Radiation”, 2008, Andrea Schmidt, H. Ardavan, J. Fasel III, M. Perez, J. Singleton, Bulletin of the American Astronomical Society (BAAS), Vol. 39, No. 4, 742, 917, Austin, Texas Meeting, January 7-11, 2008.
- (iv) “Polarization Currents that Travel Faster than the Speed of Light in Vacuo: Laboratory Demonstrations and a Model for Pulsar Observational Data”, 2008, John Singleton, A. Schmidt, J. Fasel, H. Ardavan, A. Ardavan, M. R. Perez, Bulletin of the American Astronomical Society (BASS), Vol. 39, No. 4, 742, 950, Austin, Texas Meeting, January 7-11 2008.

5.12.2. Talks, seminars and colloquia

- (i) “Polarization currents that travel faster than the speed of light in vacuo: laboratory demonstrations and a model for pulsar observational data”, J. Singleton, A. Schmidt, J. Fasel, H. Ardavan, A. Ardavan, M. Perez, Austin, 211th Meeting of the American Astronomical Society, January 2008
- (ii) “On the Superluminal Model of Pulsar Radiation”, A. Schmidt, J. Fasel, H. Ardavan, A. Ardavan, J. Singleton, Poster, Socorro, 23rd Annual New Mexico Symposium, October 2007
- (iii) “Lawbreakers? Superluminal sources in the laboratory and as a model for pulsars”, A. Schmidt and J. Singleton, Talk, Los Alamos, Los Alamos Astronomical Society, December 2007
- (iv) “Superluminal Emission Processes as a Key to Understanding Pulsar Radiation”, A. Schmidt, H. Ardavan, J. Fasel, M. Perez, J. Singleton, Austin, Poster, 211th Meeting of the American Astronomical Society, January 2008

- (v) “Superluminal Emission Processes as a Key to Understanding Unexplained Astrophysical Phenomena”, A. Schmidt, University of New Mexico, Albuquerque, LAAZ ASUNM Daze, February 2008
- (vi) “Radiation Theory of Astronomical Sources that Move Faster than Light: Application to Pulsars”, A. Schmidt, Los Alamos, 2008 Student Symposium, Los Alamos, August 2008
- (vii) “The SN 1987A Mystery Spot, GRBs, other SNe, and Ia Cosmology”, John Middleditch, at the 23rd annual NM Symposium at Socorro, October 19th, 2007.
- (viii) “The SN 1987A beam/jet and Mystery Spot: the Rosetta Stone for 99 percent of GRBs”, John Middleditch, Poster at the 2007 Gamma-ray Burst Conference in Santa Fe, Nov 5-8, 2007.
- (ix) “The SN 1987A Beam/Jet and Its Associated Mystery Spot”, John Middleditch and Mario R. Perez, Poster at the 211th Meeting of the American Astronomical Society in Austin, Jan 7-11, 2008.
- (x) “The Kinematics of the SN 1987A Beam/Jet(s)”, John Middleditch and Mario R. Perez, Poster at the 212th Meeting of the American Astronomical Society in St. Louis, June 1-5, 2008.
- (xi) “Pulsars, Cosmology, and Science with Giant Telescopes”, John Middleditch, Talk at the Science with Giant Telescopes Meeting in Chicago, June 15-18, 2008.
- (xii) “Faster-Than-Light Electromagnetic Sources”, David Bizzozero, 2008 Student Symposium, held August 5-6, 2008 at the University of New-Mexico-Los Alamos.
- (xiii) “Radiation Theory of Astronomical Sources that Move Faster than Light”, David Bizzozero and Andrea Schmidt, AET Division talk, July 29, 2008.
- (xiv) “Terrestrial and Astronomical Radiation Sources that Move Faster than Light”, David Bizzozero and Andrea Schmidt, Colloquium at the University of New Mexico (Albuquerque), September 17 2008
- (xv) “Development of Signal Modulation Methods and Control Systems for a Ground-based Pulsar: the Superluminal RF Source”, Ian Higginson, poster, Science and Energy Research Challenge (SEARCh), Oak Ridge, 9-10 November 2008.

6. References and publications

Articles with **bold** titles have been prepared as part of the work of the current program.

- [1] J. Singleton, A. Ardavan, H. Ardavan, J. Fopma, D. Halliday, and W. Hayes, *Experimental demonstration of emission from a superluminal polarization current - a new class of solid-state source for MHz-THz and beyond*, Conference Digest of the 2004 Joint 29th International Conference on Infrared and Millimeter Waves and 12th International Conference on Terahertz Electronics (IEEE Cat. No.04EX857) (2004) p.591-2
- [2] A. Ardavan, W. Hayes, J. Singleton, H. Ardavan, J. Fopma, and D. Halliday, *Experimental observation of nonspherically-decaying radiation from a rotating superluminal source*, Journal of Applied Physics **96**, 7760-77 (2004)

- [3] A. Schmidt, H. Ardavan, J. Fasel, J. Singleton, and A. Ardavan, *Occurrence of concurrent 'orthogonal' polarization modes in the Lienard-Wiechert field of a rotating superluminal source*, in W. Becker and H. H. Huang, editors, *Proceedings of the 363rd WE Heraeus Seminar on Neutron Stars and Pulsars*, pages 124-127 (2007) and at arXiv: 0701257 [astro-ph].
- [4] H. Ardavan, A. Ardavan, and J. Singleton, *Spectral and polarization characteristics of the nonspherically decaying radiation generated by polarization currents with superluminally rotating distribution patterns* *Journal of the Optical Society of America A (Optics, Image Science and Vision)* **21**, 858-72 (2004)
- [5] H. Ardavan, A. Ardavan, and J. Singleton, *Spectral and polarization characteristics of the nonspherically decaying radiation generated by polarization currents with superluminally rotating distribution patterns: reply to comment*, *Journal of the Optical Society of America A (Optics, Image Science and Vision)* **23**, 1535-9 (2006)
- [6] B. M. Bolotovskii and V. L. Ginzburg, *The Vavilov-Čerenkov effect and the Doppler effect in the motion of sources with superluminal velocity in vacuum*, *Sov. Phys. Usp.* **15**, 184-192 (1972).
- [7] V.L. Ginzburg, *Vavilov-Čerenkov effect and anomalous Doppler effect in a medium in which wave phase velocity exceeds velocity of light in vacuum*, *Sov. Phys. JETP.* **35**, 92-93 (1972).
- [8] US patent **Apparatus and method for phase fronts based on superluminal polarization current**, J. Singleton, H. Ardavan and A. Ardavan, filed as 12/191,148.
- [9] A. V. Bessarab, A. A. Gorbunov, S. P. Martynenko and N. A. Prudkoy, *Faster-than-light EMP source initiated by short X-ray pulse of laser plasma*, *IEEE Trans. Plasma. Sci.* **32**, 1400-1403 (2004).
- [10] A.V. Bessarab, S.P. Martynenko, N.A. Prudkoi, A.V. Soldatov and V.A. Terekhin, *Experimental study of electromagnetic radiation from a faster-than-light vacuum macroscopic source*, *Radiation Physics and Chemistry* **75**, 825-831 (2006).
- [11] B. M. Bolotovskii and A. V. Serov, *Radiation of superluminal sources in empty space*, *Phys. Usp.* **48**, 903-915 (2005).
- [12] H. Ardavan, A. Ardavan and J. Singleton, *Frequency spectrum of focused broadband pulses of electromagnetic radiation generated by polarization currents with superluminally rotating distribution patterns*, *Journal of the Optical Society of America A (Optics, Image Science and Vision)* **20**, 2137-2155 (2003).
- [13] H. Ardavan, *Generation of focused, nonspherically decaying pulses of electromagnetic radiation*, *Phys. Rev. E*, **58** 6659-84 (1998).
- [14] H. Ardavan, A. Ardavan, J. Singleton and M.R. Perez, **Mechanism of generation of the emission bands in the dynamic spectrum of the Crab pulsar**, *Mon. Not. R. Astron. Soc.* **388**, 873-883 (2008).
- [15] J.D. Jackson, *Classical Electrodynamics*, (Wiley, 2nd Edition, 1975)
- [16] JP Accelerator Works, <http://www.jpaw.com>
- [17] Computer Simulation Technology, <http://www.cst.com>
- [18] Thomas Keating Ltd., Billingshurst, UK, <http://www.terahertz.co.uk>
- [19] K. Gentile, *Digital Quadrature Modulator Gain*, Analog Devices Application Note, AN-924.
- [20] Advanced Circuits, <http://www.4pcb.com>
- [21] Emerson and Cuming Microwave Products, <http://www.eccosorb.com/america/english/page/92/geometric-absorbers>.
- [22] G.M. Lilley, R. Westley, A.H. Yates and Y.R. Busing, *Some aspects of noise from supersonic aircraft*, *J. Royal Aeronautical Soc.* **57**, 396-414 (1953).
- [23] G.M. Lilley, R. Westley, A.H. Yates and Y.R. Busing, *The supersonic bang*, *Nature* **171**, 994-996 (1953).
- [24] T. Gold, *The double bang of supersonic aircraft*, *Nature* **170**, 808 (1952).
- [25] P. Volegov, H. Ardavan, J. Middleditch and A. Ardavan, **Draft discussion document on superluminal models for gamma-ray bursts.**
- [26] H. Ardavan, A. Ardavan, J. Singleton, J. Fasel, A. Schmidt, **Fundamental role of the retarded potential in the electrodynamics of superluminal sources**, *Journal of the Optical Society of America A (Optics, Image Science and Vision)* **25**, 543-57 (2008).
- [27] H. Ardavan, A. Ardavan, J. Singleton, J. Fasel and A. Schmidt, **Morphology of the nonspherically decaying radiation beam generated by a rotating superluminal source**, *Journal of the Optical Society*

- of America A (Optics, Image Science and Vision) **24**, 2443-56 (2008).
- [28] H. Ardavan, A. Ardavan, J. Fasel, J. Middleditch, M. Perez, A. Schmidt, J. Singleton, **A new mechanism for generating broadband pulsar-like polarization**, in *Proc. Int. Conf. Polarimetry 2008, Rome*, in press, and at arXiv:0903.0399.
 - [29] H. Ardavan, A. Ardavan, J. Singleton, J.H. Fasel, A. Schmidt **Morphology of the nonspherically decaying radiation generated by a rotating superluminal source: reply to comment** Journal of the Optical Society of America A (Optics, Image Science and Vision) **25**, 2167-169 (2008).
 - [30] H. Ardavan, A. Ardavan, J. Singleton, J.H. Fasel, A. Schmidt, **Method of handling the divergences in the radiation theory of sources that move faster than their own waves** J. Math. Phys., in press (2009)
 - [31] T. Gold, *Rotating neutron stars as the origin of the pulsating radio sources*, Nature **218** 731-2 (1968).
 - [32] H. Ardavan, A. Ardavan, J. Singleton, J. Fasel, A. Schmidt, **Spectral properties of the nonspherically decaying radiation generated by a rotating superluminal source**, Journal of the Optical Society of America A (Optics, Image Science and Vision) **25**, 780-4 (2008).
 - [33] P. Colwell. *Solving Kepler's equation over three centuries* (Willman-Bell, Richmond, VA, 1993).
 - [34] S. Sallmen, D. C. Backer, T. H. Hankins, D. Moffett, and S. Lundgren. *Simultaneous dual-frequency observations of giant pulses from the Crab pulsar*, Astrophys. J. **517**, 460-471, (1999).
 - [35] M. V. Popov, V. A. Soglasnov, V. I. Kondrat'ev, S. V. Kostyuk, and Yu. P. Ilyasov. *Giant pulses-the main component of the radio emission of the Crab pulsar*, Astron. Rep. **50**, 55-61 (2006).
 - [36] A. V. Popov, A. D. Kuz'min, O. M. Ul'yanov, A. A. Deshpande, A. A. Ershov, V. V. Zakharenko, V. I. Kondrat'ev, S. V. Kostyuk, B. Ya. Losovskii, and V. A. Soglasnov. *Instantaneous radio spectra of giant pulses from the Crab pulsar from decimeter to decameter wavelengths*, Astron. Rep., **50**, 562-568, (2006).
 - [37] A. Iserles, *On quadrature methods for highly oscillatory integrals and their implementation*, BIT, **44**(4), 755-772 (2004).
 - [38] H. Ardavan, A. Ardavan, J. Fasel, J. Middleditch, M. Perez, A. Schmidt, J. Singleton, **Universal behavior of pulsar frequency spectra**, in preparation for submission to Mon. Not. Roy. Ast. Soc. (2009).
 - [39] J. Singleton, P. Sengupta, J. Middleditch, M.R. Perez, H. Ardavan, A. Ardavan, **Unusual flux-distance relationship for pulsars suggested by analysis of the Australia National Telescope Facility Pulsar Catalogue**, preprint to be submitted to Nature (2009).
 - [40] T.H. Hankins and J.A. Eilek, *Radio emission signatures in the Crab pulsar*, Astrophysical Journal **670**, 693-701 (2007).
 - [41] A.G. Lyne and F. Graham-Smith, *Pulsar Astronomy*, Cambridge University Press, Cambridge, UK (2006).
 - [42] R.N. Manchester, G.B. Hobbs, A. Teoh and M. Hobbs, *The Australia Telescope National Facility Pulsar Catalogue*, Astrophysical Journal **129**, 1993-2006 (2005).
 - [43] J.A. Zensus and T.J. Pearson, *Superluminal Radio Sources*, Cambridge University Press, Cambridge, UK (1987).
 - [44] D.R. Lorimer, A.J. Faulkner, A.G. Lyne, R.N. Manchester, M. Kramer, M.A. McLaughlin, G. Hobbs, A. Possenti, I.H. Stairs, F. Camilo, M. Burgay, N. D'Amico, A. Corongiu and F. Crawford, *The Parkes Multibeam Pulsar Survey - VI. Discovery and timing of 142 pulsars and a Galactic population analysis*, Mon. Not. Roy. Astron. Soc. **372**, 777 (2006).
 - [45] J.H. Taylor and J.M. Cordes, *Pulsar distances and the galactic distribution of free electrons*, Astrophysical Journal, **411**, 674-684 (1993).
 - [46] J.M. Cordes and T.J.W. Lazio, *A new model for the galactic distribution of free electrons and its fluctuations* arXiv : astro - ph/0207156v3(2003).
 - [47] J.M. Cordes and T.J.W. Lazio, *Using radio propagation data to construct a model for the galactic distribution of free electrons* arXiv : astro - ph/0301598v1(2003).
 - [48] J.V. Wall and C.R. Jenkins, *Practical Statistics for Astronomers*, Cambridge University Press, Cambridge, UK (2003).
 - [49] G. Efstathiou, R.S. Ellis, B.A. Peterson, *Analysis of a complete galaxy redshift survey- II the field-galaxy luminosity function*, Mpn. Not. R. Astr. Soc. **232**, 431-461 (1988).
 - [50] T. Graves, W. Junor and J. Singleton, **Bayesian Analysis of the Parkes Multibeam Survey**, internal report,

in preparation for publication (2009).

- [51] M.R. Perez, B. McCollum, M.E. van den Ancker, M.D. Joner, **The enigmatic young object: Walker 90/V590 Monocerotis**, Perez, MR ; McCollum, B ; van den Ancker, ME ; Joner, MD *Astronomy and Astrophysics* **486**, 533-544 (2008).